MULTI-PHASE FAULT TOLERANT PMSM DRIVE SYSTEM

A Dissertation

by

JAEBUM PARK

Submitted to the Office of Graduate and Professional Studies of
Texas A&M University
in partial fulfillment of the requirements for the degree of

DOCTOR OF PHILOSOPHY

Chair of Committee,	Hamid A. Toliyat
Committee Members,	Won-Jong Kim
	Prasad Enjeti
	Shankar P. Bhattacharyya
Head of Department,	Chanan Singh

May 2015

Major Subject: Electrical Engineering

ABSTRACT

The drive to develop electric machines with a wide constant power-speed range (CPSR), high torque capabilities, excellent efficiency, superior reliability, and a reduced environmental footprint for EV traction and ship propulsion systems has led to research interest in various Permanent Magnet Synchronous Motors (PMSM). One particular area of interest is multi-phase fault tolerant PMSM drive systems, which are integral to the development of electric traction systems with all-inclusive motors that include sensors, inverter modules, and a cooling system, much like an automobile engine. Furthermore, these designs simplify fault condition maintenance because their independent single-phase structure allows them to be used with replaceable modular inverter units which have one H-bridge for each phase. In order to provide high reliability for the PMSM drive systems, even in a fault condition, simple but effective current control methods are necessary.

An interior PMSM configuration with 5 independent phases is presented for electric vehicle (EV) traction and ship propulsion applications along with the proposed design procedure as well as an associated inverter design and current control methods. The proposed design process is verified using finite element analysis (FEA). An existing 5-phase 15-slot 4-pole Interior PMSM was modified to remove the neutral point, thus allowing for independent control of the 5 phases with 5 H-bridge inverters through a fabricated custom-made control board. Bipolar and unipolar switching methods were evaluated and an effective switching method was proposed to drive the motor. Closed

loop speed control was implemented using Step VSI control, SPWM control, and hysteresis control methods. Finally, the 5-phase 10-lead PMSM systems were evaluated under the various control methods using simulated and experimental data after fabricating a new inverter interface board with TI floating point DSP, Delfino (F28335). The results suggest that multi-phase fault tolerant PMSM drive systems could play a key role in the future of EV traction and ship propulsion systems.

DEDICATION

To my parents: Jong-Hwan Park and Gong-Rye Hwang

To my wife, Mi-Young Choi

To my parents in law: Gi-Whoo Choi and Myoung-Ja Kim

To my son: In-Chan Park

To my daughter: Hea-Na Park

To my brothers: Chae-Su Park and Sung-Min Park

To my brother in law: Hyun-Jin Choi

ACKNOWLEDGEMENTS

I love to acknowledge and deeply thank those who have helped me in accomplishing this dissertation. First and foremost, I would like to express my sincere appreciation to my supervisor, Hamid A. Toliyat, for his support and insightful guidance. His continuing devotion and innovative ideas in his research have truly inspired me.

I am very thankful for Dr. Prasad Enjeti, Dr. Shankar P. Bhattacharyya and Dr. Won-Jong Kim, who generously advised me to carry out this dissertation as well as the wonderful courses I took from them. I have benefited from their knowledge, help, and guidance throughout the course of my studies.

I would like to send my great appreciation to Prof. Ju Lee who always guided me from South Korea.

I also wish to thank the Electrical and Computer Engineering Department at Texas A&M University for providing me with a great educational environment and to acknowledge all current and past students in the research group and in Texas A&M power electronics division, without whom my work would have been very hard. I thank (in no particular order) all others in the EPPE research division for making learning and life enjoyable.

Last but not least, I thank my parents, my wife Mi-Young Choi, my son In-Chan Park, my daughter Hea-Na Park, my brothers, relatives and friends for their patience, endless love, and support during all these years that I have just neglected them.

TABLE OF CONTENTS

Page

LIST OF FIGURES

Page

LIST OF TABLES

Page

1. INTRODUCTION

1.1. Technical roadmap of electric machines

Recently, various electric traction applications have led to increased motor reliability demands, and developments in power electronics have made the use of multi-phase motors a feasible solution to this problem. Multi-phase motors offer additional degrees of freedom in comparison to single-phase motors as well as many other qualities which compare favorably to those of the conventional three-phase motors, such as high torque capability, reduced torque pulsation, improved reliability, increased torque per ampere performance for a given machine size, diminished stator copper losses, and reduced rotor harmonic currents [1]-[4].

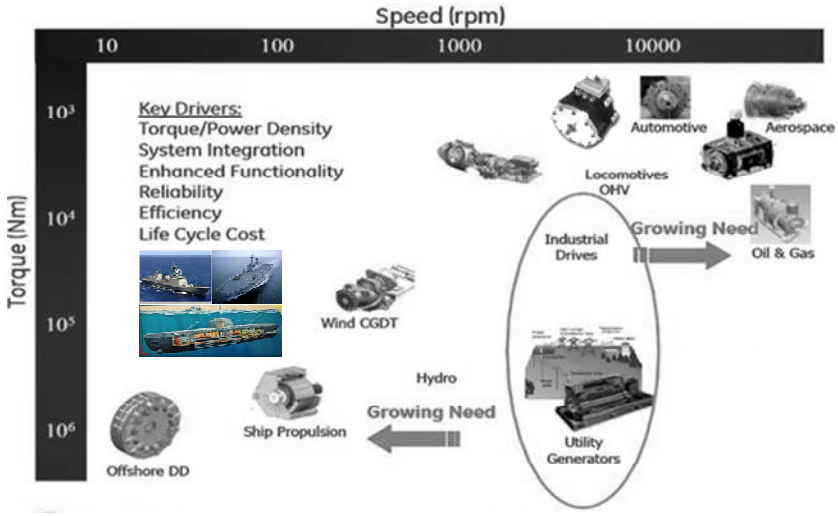

Fig. 1. Technical roadmap of electrical machines

Multi-phase motors are primarily used in a few specific applications such as hybrid and electrical vehicles, marine vessels, and electric locomotives. Fig. 1 shows the technical roadmap of electric machines in terms of speed and torque. The demand for electric machines is growing rapidly in both the electric vehicle and ship propulsion industries.

1.2. Electric vehicle and electric ship propulsion markets

Fig. 2 shows the conservative estimate of the worldwide automobile market. Full, mild and plug-in hybrid demand to reach 7.5 million units in 2019 and the EV market has been increasing every year and the electric vehicle portion of this market is getting larger. Global EV demand is 1.5 million units in 2019 [5]-[9].

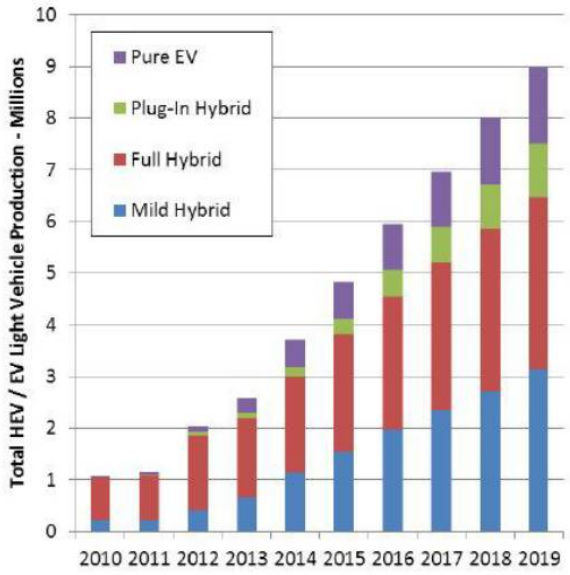

Fig. 2. Worldwide automobile market (Copyright 2012 by STRATEGY ANALYTICS SAE-ATA)

Fig. 3 shows the ship propulsion industry market which was over 1 billion US dollars in 2010 and is growing at a rate of over 10% per year. This demand has led to the increased research interest in multi-phase fault tolerant PMSM drive systems for ship propulsion and EV traction applications [10]-[12].

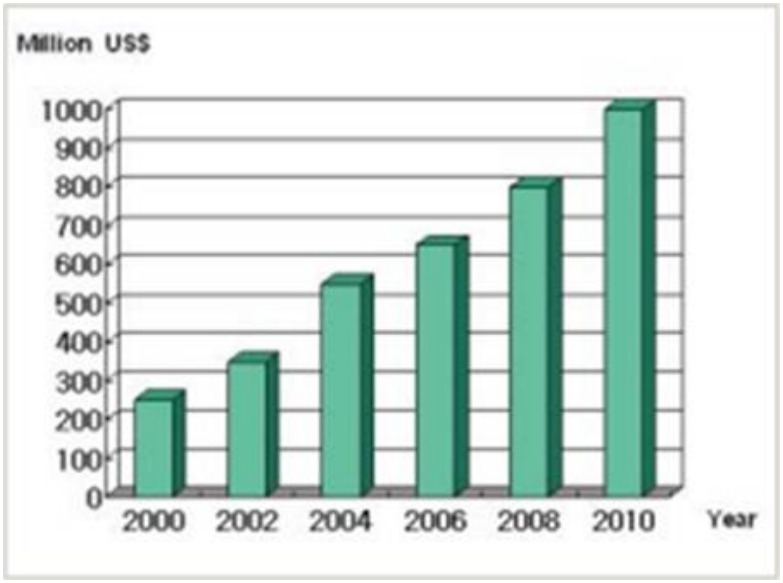

Fig. 3. Electric Propulsion System Market (Copyright 2009 by ABB)

1.2.1. Proposed solution: 5-phase 10-lead interior PMSM drive systems

Instead of using the conventional 3-phase, 5-phase, or 6-phase systems, this dissertation proposes the 5-phase interior PMSM with a unique structure which does not have neutral point inside of the motor. The main idea is to use the 5-phase motor just like 5 independent single-phase motors. The motor which has 10 leads or terminals can be easily maintained even if it loses some phases under a fault condition with modular replaceable inverter units because each phase can be operated independently without

neutral point. Various control methods will be applied to confirm the mechanical structure and proposed inverter systems.

1.3. Motivation

The motivation to pursue this research is the all-inclusive motors which have sensors, inverter modules, and cooling system will be used in the future, just like an automobile engine. Fault condition maintenance will be easier because modular replaceable inverter units which have one H-bridge for each phase with the independent single-phase structure motor will be used. In order to provide high reliability, simple but effective current control methods are necessary, even in a fault condition.

1.4. Outline of the dissertation

This dissertation is organized into six sections. Each section includes and explains the following contents and ranges below.

Section 1 introduces the technical trend of electric machines and the market estimate of the EV traction and ship propulsion systems. A proposed solution for both traction and propulsion systems is elucidated, and the section concludes by explaining the research objective and the dissertation outline. Each major section has literature review at the beginning.

Section 2 explains mathematical modeling of interior PMSM for conventional 3-phase and proposed 5-phase 10-lead interior PMSM. Reference transformation for 5-

phase machine is also explained in detail and the extra x-y set of components is introduced in this section.

Section 3 proposes a design procedure with six sigma tools. The proposed topology is confirmed and validated though FEM. In basic design, the stator slot and rotor pole combination with winding method was chosen after air-gap force distribution analysis. This section also discusses design results of each part.

Section 4 proposes an inverter design for 5-phase 10-lead interior PMSM. 20 IGBTs power the motor and are controlled by TI's DSP, F28335. The interface board includes seven parts: DSP board connector, current sensing circuit, QEP circuit, hardware protection circuit, PWM signal circuit, inverter gate signal connector, and power supply circuit parts.

Section 5 discusses the fabrication of a reconfigurable control set-up, and the results of the experiments performed on the set-up. An effective switching method was proposed and confirmed through various control methods: 10-step VSI control, SPWM control, and hysteresis control. Closed speed loops for each control method are implemented and shown in this section.

Section 6 provides a summary of the research work and concludes the dissertation by suggesting recommendations for future research in this area.

2. MATHEMATICAL MODELING OF INTERIOR PMSM*

2.1. Introduction

Permanent Magnet Synchronous Motors (PMSM) are generally classified as either Surface Permanent Magnet Synchronous Motor (SPMSM) or Interior Permanent Magnet Synchronous Motors (IPMSM) depending on how the magnets are attached to the rotor. Fig. 4 shows the classifications of brushless synchronous motors which have different magnet positions or no magnets on the rotors [13]-[15].

PMSM can be divided into two sub-categories based on Back-EMF waveform shapes and the applied current. The first sub-category is the brushless ac PM synchronous motor, SPMSM, which has a sinusoidal Back-EMF waveform and uses a sinusoidal current control method. The next sub-category is the brushless dc PM motor which has a trapezoidal Back-EMF waveform and uses a square wave current control method [16]. The BLDC PM motor has similar structure to the DC motor, but the brush and commentator are replaced with an inverter, so the control method is the same as that of a DC motor. This makes the system easy to control and inexpensive, but The BLDC

---

*Part of this section is reprinted with permission from:
"Integrated Torque Ripple Analysis Method for Multi-Phase Motors" by Jae-Bum Park, M. Johnson, and H.A. Toliyat, *Proc. 2013 IEEE International Electric Machines and Drives Conf., pp*. 294-299. Copyright 2013 by IEEE and
"A Novel Switching Hysteresis Current Control Method for Torque Ripple Minimization in Multi-Phase Motors" by Jae-Bum Park, M. Johnson, and H.A. Toliyat, in *Proc. 2014 IEEE Energy Convers. Congr. Expo. (ECCE), pp*. 3251-3258. Copyright 2014 by IEEE.

PM motor has a very high torque ripple during changes in the current direction, and it is not good for precise control and traction applications.

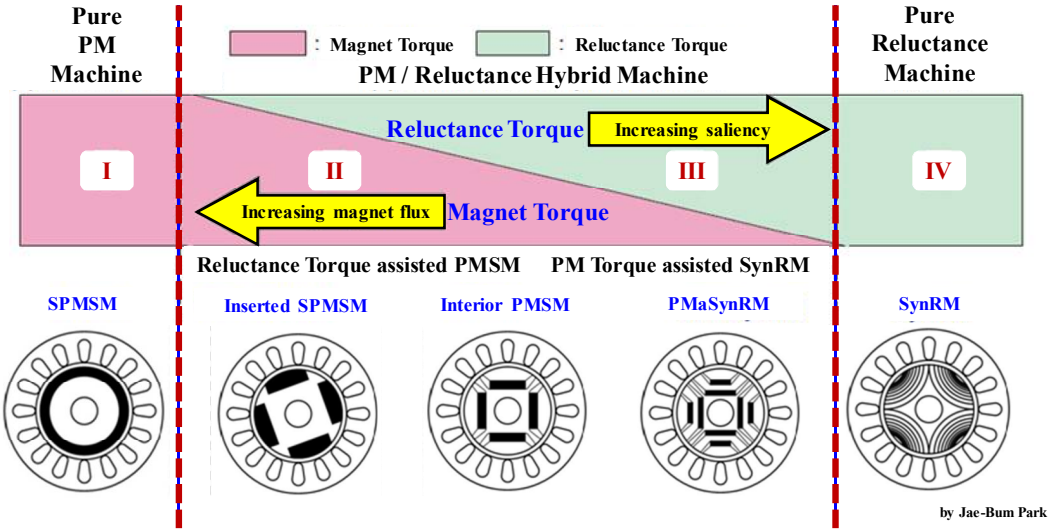

Fig. 4. Brushless synchronous motor classification

The BLAC PMSM, SPMSM, has an advantage in that it can generate very low torque ripple because the motor has sinusoidal Back-EMF, and a vector controller can smoothly operate the motor with sinusoidal currents. Both of them need to have a nonmagnetic protector which fixes the magnets on the rotors at high speeds. This protector makes the motor air-gap bigger which results in a lower power density. Moreover, the flux associated with the stator winding currents affects the magnet surfaces and can demagnetize the magnets.

In an interior PMSM, the magnets are inserted into the rotor barriers, which minimize the effective air-gap length and maximize the motor output power.

Furthermore, its magnet and reluctance torque generation capabilities provide a means of maximizing power density through the design of the rotor core's saliency. This saliency property allows an IPMSM to generate both reluctance torque and magnet torque, a combination which offers the potential for high-power and high-speed performance when operated with field weakening control algorithms.

There are three primary types of rotor shapes for an IPMSM: single layer rotors, V-shaped rotors, and double layer rotors. The first configuration is easy to manufacture but generates low reluctance torque because of its small saliency ratio. This design is good for low speed, high torque applications, but its characteristically large excitation currents prevent it from simultaneously offering high torque, speed, and efficiency in the field weakening region. The second type of rotor offers more reluctance torque than the single layer rotor, but less magnet torque and ultimately, less overall torque because of its larger saturation areas. The third topology, the double layer rotor, is the most efficient since the flux per phase is controllable based on the flux path design for saliency and saturation in the rotor core [17]-[22]. As a result of its enhanced characteristics the double layer rotor IPMSM has drawn significant worldwide research interest [23].

2.2. Conventional 3-phase interior PMSM model

Fig. 5 shows the analytical model of the IPMSM which defines the relationship between the a-b-c reference frame and the d-q reference frame in Fig. 6. The flux path of the permanent magnets is aligned with the d-axis and the q-axis leads this path by 90 electrical degrees.

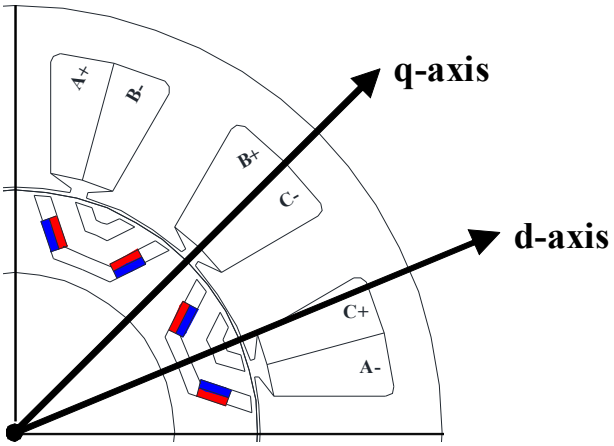

Fig. 5. d-q axis definition

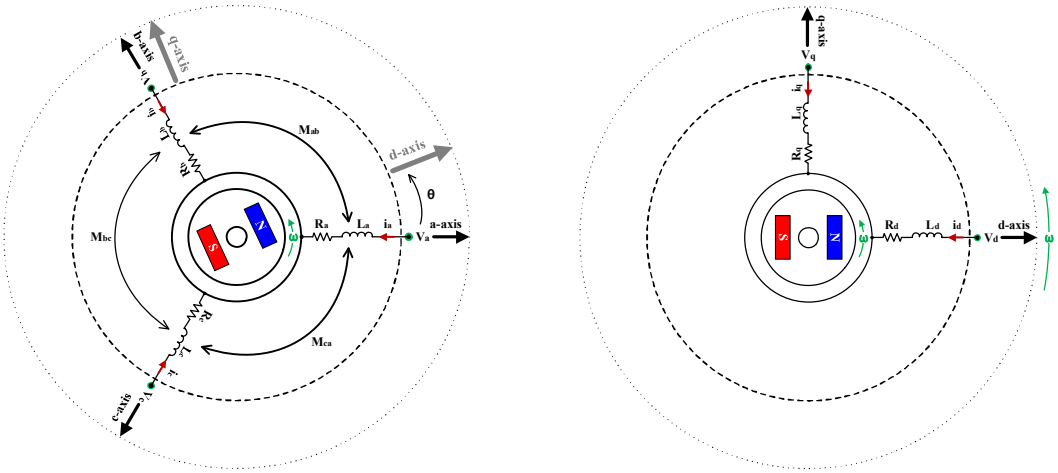

(a) **(b)**

Fig. 6. Analytical model of 3-phase PMSM. (a) a-b-c reference frame. (b) d-q reference frame.

Defining θ as the angle between the a-axis and the d-axis, allows the stator self-inductances, mutual inductances, and the permanent magnet flux linkages to be expressed as:

$$\begin{pmatrix} L_a = L_l + L_m = L_l + L_{avg} - L_{pp}\cos 2\theta \\ L_b = L_l + L_m = L_l + L_{avg} - L_{pp}\cos\left(2\theta + \frac{2}{3}\pi\right) \\ L_c = L_l + L_m = L_l + L_{avg} - L_{pp}\cos\left(2\theta - \frac{2}{3}\pi\right) \end{pmatrix} \quad (1)$$

$$\begin{pmatrix} M_{ab} = -\frac{1}{2}L_{avg} - L_{pp}\cos\left(2\theta - \frac{2}{3}\pi\right) \\ M_{bc} = -\frac{1}{2}L_{avg} - L_{pp}\cos 2\theta \\ M_{ca} = -\frac{1}{2}L_{avg} - L_{pp}\cos\left(2\theta + \frac{2}{3}\pi\right) \end{pmatrix} \quad (2)$$

$$\begin{pmatrix} \Psi_{fa} = \Psi_f \cos 2\theta \\ \Psi_{fb} = \Psi_f \cos\left(2\theta - \frac{2}{3}\pi\right) \\ \Psi_{fc} = \Psi_f \cos\left(2\theta + \frac{2}{3}\pi\right) \end{pmatrix} \quad (3)$$

$$\begin{pmatrix} M_{ab} = -\frac{1}{2}L_{avg} - L_{pp}\cos\left(2\theta - \frac{2}{3}\pi\right) \\ M_{bc} = -\frac{1}{2}L_{avg} - L_{pp}\cos 2\theta \\ M_{ca} = -\frac{1}{2}L_{avg} - L_{pp}\cos\left(2\theta + \frac{2}{3}\pi\right) \end{pmatrix} \quad (4)$$

$$\begin{pmatrix} M_{ab} = -\frac{1}{2}L_{avg} - L_{pp}\cos\left(2\theta - \frac{2}{3}\pi\right) \\ M_{bc} = -\frac{1}{2}L_{avg} - L_{pp}\cos 2\theta \\ M_{ca} = -\frac{1}{2}L_{avg} - L_{pp}\cos\left(2\theta + \frac{2}{3}\pi\right) \end{pmatrix} \quad (5)$$

$$\begin{pmatrix} M_{ab} = -\frac{1}{2}L_{avg} - L_{pp}\cos\left(2\theta - \frac{2}{3}\pi\right) \\ M_{bc} = -\frac{1}{2}L_{avg} - L_{pp}\cos 2\theta \\ M_{ca} = -\frac{1}{2}L_{avg} - L_{pp}\cos\left(2\theta + \frac{2}{3}\pi\right) \end{pmatrix} \quad (6)$$

where

L_a, L_b, L_c: stator self-inductances

L_l: leakage inductance per a phase

L_m: magnetizing inductance per a phase

L_{avg}: average magnetizing inductance per a phase

L_{pp}: peak to peak magnetizing inductance per a phase

M_{ab}, M_{bc}, M_{ca}: stator mutual inductances

Ψ_f : maximum flux linkage by PM per a phase

Ψ_{fa}, Ψ_{fb}, Ψ_{fc} : phase flux linkages

$\theta = \omega t$: angle between the a-axis and d-axis

ω: electrical angular speed

From (1), (2), and (3), the IPMSM stator voltage equation in the a-b-c reference frame is given by:

$$\begin{bmatrix} V_a \\ V_b \\ V_c \end{bmatrix} = \begin{bmatrix} R_a + \frac{d}{dt}L_a & \frac{d}{dt}M_{ab} & \frac{d}{dt}M_{ca} \\ \frac{d}{dt}M_{ab} & R_b + \frac{d}{dt}L_b & \frac{d}{dt}M_{bc} \\ \frac{d}{dt}M_{ca} & \frac{d}{dt}M_{bc} & R_c + \frac{d}{dt}L_c \end{bmatrix} \begin{bmatrix} i_a \\ i_b \\ i_c \end{bmatrix} - \begin{bmatrix} \omega\Psi_f \sin\theta \\ \omega\Psi_f \sin\left(\theta - \frac{3}{2}\pi\right) \\ \omega\Psi_f \sin\left(\theta + \frac{3}{2}\pi\right) \end{bmatrix} \quad (7)$$

where

V_a, V_b, V_c: phase voltages

i_a, i_b, i_c: phase currents

R_a, R_b, R_c: phase resistances

Fig. 7 shows the d-q equivalent circuit of the IPMSM which is transformed from the a-b-c reference frame to the d-q reference frame.

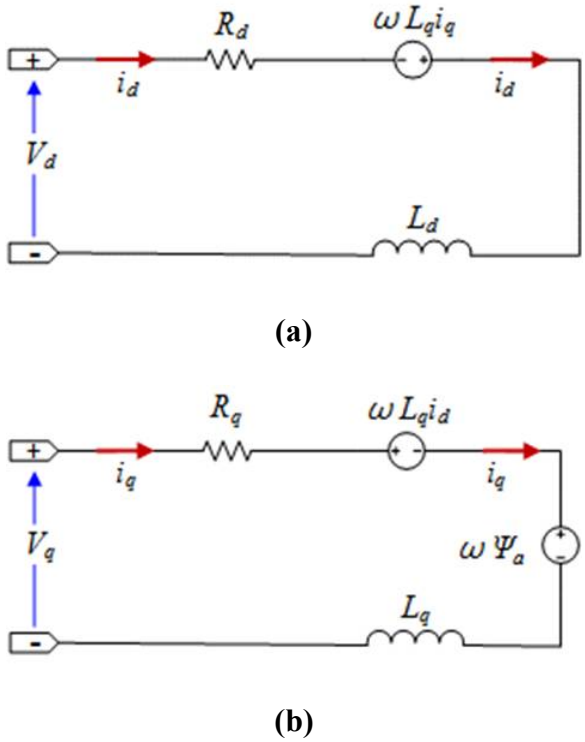

Fig. 7. d-q axis equivalent circuit considering core loss. (a) d-axis equivalent circuit. (b) q-axis equivalent circuit.

Analytical modeling of the voltage equation is very complicated in the a-b-c reference frame, because the angle ($\theta = \omega t$) varies with time (t). The transformation

matrix from the a-b-c reference frame to the d-q reference frame is shown in (8). Based on this transformation, the stator voltage equation rotates with the angular speed (ω) in the d-q reference frame and can be reformulated as (9).

$$T(\theta)=\sqrt{\frac{2}{3}}\begin{bmatrix} \cos\theta & \cos\left(\theta-\frac{2}{3}\pi\right) & \cos\left(\theta+\frac{2}{3}\pi\right) \\ -\sin\theta & -\sin\left(\theta-\frac{2}{3}\pi\right) & -\sin\left(\theta+\frac{2}{3}\pi\right) \end{bmatrix} \tag{8}$$

$$\begin{bmatrix} V_d \\ V_q \end{bmatrix} = T(\theta)\begin{bmatrix} V_a \\ V_b \\ V_c \end{bmatrix} = \begin{bmatrix} R_d+\frac{d}{dt}L_d & -\omega L_q \\ \omega L_d & R_q+\frac{d}{dt}L_q \end{bmatrix}\begin{bmatrix} i_d \\ i_q \end{bmatrix} + \begin{bmatrix} 0 \\ \omega\Psi_a \end{bmatrix} \tag{9}$$

where

V_d, V_q: d- and q-axis stator voltage components

i_d, i_q: d- and q-axis stator current components

$R_a = R_b = R_c = R_d = R_q$: phase resistances

$L_d = L_l + \frac{3}{2}(L_{avg} - L_{pp})$: d-axis inductance

$L_q = L_l + \frac{3}{2}(L_{avg} + L_{pp})$: q-axis inductance

$\Psi_a = \sqrt{\frac{3}{2}}\Psi_f = \sqrt{3}\Psi_{rms}$: PM flux linkage

$\Psi_{rms} = \frac{\Psi_f}{\sqrt{2}}$: rms value of the phase flux linkage

In the d-q reference frame, the d-axis and q-axis currents can be represented by the phase current and the phase angle of the current (β). The flux linkages and electromagnetic torque are given as:

$$\begin{aligned} i_d &= -I_a \sin\beta \\ i_q &= I_a \cos\beta \end{aligned} \tag{10}$$

$$\begin{aligned} \lambda_d &= L_d i_d + \Psi_a \\ \lambda_q &= L_q i_q \end{aligned} \tag{11}$$

$$\begin{aligned} T &= \frac{P_n}{2}\left(\lambda_d i_q - \lambda_q i_d\right) = \frac{P_n}{2}\left(\Psi_a i_q + \left\{L_d - L_q\right\} i_d i_q\right) \\ &= \frac{P_n}{2}\left(\Psi_a I_a \cos\beta + \frac{1}{2}\left\{L_q - L_d\right\} {I_a}^2 \sin 2\beta\right) \end{aligned} \tag{12}$$

where

L_d, L_q: d-axis and q-axis inductances

λ_d, λ_q: d-axis and q-axis flux linkages

P_n: number of the rotor poles

In an IPMSM, L_q is typically larger than L_d and the currents, i_d and i_q, must have opposite polarities in order to contribute a positive torque in (12). This negative d-axis current may cause demagnetization of the permanent magnets. The first term in (12) is the magnetic torque which is independent of i_d but proportional to the stator current (i_q). The second term is the reluctance torque which is proportional to the product of the current component ($i_d \times i_q$) and to the difference between the two inductance components

($L_d - L_q$). Therefore, IPMSMs have a hybrid nature, and as illustrated in Fig. 8, their torque is not linearly proportional to the stator current amplitudes because of the magnetic circuit saliency and PM demagnetization.

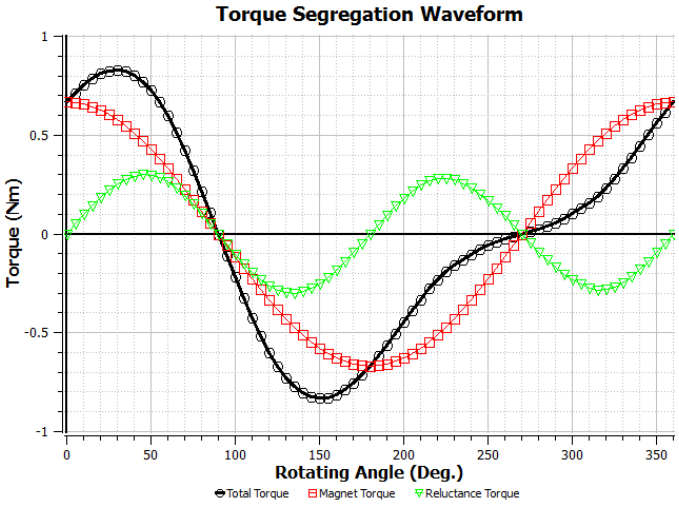

Fig. 8. Torque component waveforms

The IPMSM equivalent circuit is depicted in Fig. 9 with the equivalent core loss resistor, R_c, and the induced voltages (V_{od} and V_{oq}). The stator voltage equation can be expressed in terms of the induced currents (i_{od} and i_{oq}) as in (13).

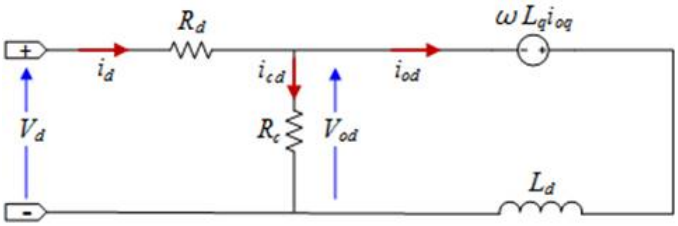

(a)

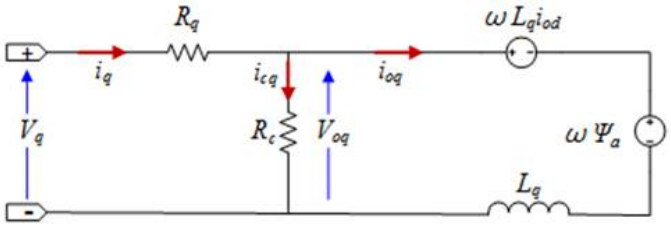

(b)

Fig. 9. d-q axis equivalent circuit considering core loss. (a) d-axis equivalent circuit. (b) q-axis equivalent circuit.

$$\begin{bmatrix} V_d \\ V_q \end{bmatrix} = R_a \begin{bmatrix} i_{od} \\ i_{oq} \end{bmatrix} + (1 + \frac{R_a}{R_c}) \begin{bmatrix} V_{od} \\ V_{oq} \end{bmatrix} + p \begin{bmatrix} L_d & 0 \\ 0 & L_q \end{bmatrix} \begin{bmatrix} i_{od} \\ i_{oq} \end{bmatrix} \tag{13}$$

where

$$\begin{bmatrix} V_{od} \\ V_{oq} \end{bmatrix} = \begin{bmatrix} 0 & -\omega L_q \\ \omega L_d & 0 \end{bmatrix} \begin{bmatrix} i_{od} \\ i_{oq} \end{bmatrix} + \begin{bmatrix} o \\ \omega \Psi_a \end{bmatrix} : \text{induced voltages}$$

$i_{od} = i_d - i_{cd}$: d-axis induced current

$i_{oq} = i_q - i_{cq}$: q-axis induced current

$i_{cd} = -\dfrac{\omega L_q i_{oq}}{R_c}$: d-axis core loss current

$i_{cq} = \dfrac{\omega(\Psi_a + L_d i_{od})}{R_c}$: q-axis core loss current

The equivalent circuit yields the following expressions for the electromagnetic torque, copper loss, core loss, total loss, and efficiency:

$$T = \frac{P_n}{2}\left(\Psi_a i_{oq} + \left\{L_d - L_q\right\} i_{od} i_{oq}\right) \tag{14}$$

$$W_{Cu} = R_a I_a{}^2 = R_a \left(i_d{}^2 + i_q{}^2\right) \tag{15}$$

$$W_c = \frac{V_o{}^2}{R_c} = \frac{V_{od}{}^2 + V_{oq}{}^2}{R_c} = \frac{\omega^2 \left\{(L_d i_{od} + \Psi_a)^2 + (L_q i_{oq})^2\right\}}{R_c} \tag{16}$$

$$W_{loss} = W_{Cu} + W_c \tag{17}$$

$$\eta = \frac{P_{out}}{P_{in}} \times 100 = \frac{P_{out}}{P_{out} + W_{loss}} \times 100 \tag{18}$$

Based on the stator voltage equation, (13), the vector diagram for an underexcited motor with a lagging power factor (δ>0 and ϕ<0) is illustrated in Fig. 10. The torque angle or load angle, δ, is defined as the angle between the V_a vector and the q-axis. The power factor angle, ϕ, is defined as the angle between the I_a and V_a vectors [24]-[27]. The current angle, β, is given by:

$$\beta = \tan^{-1}\left(\frac{i_d}{i_q}\right) \tag{19}$$

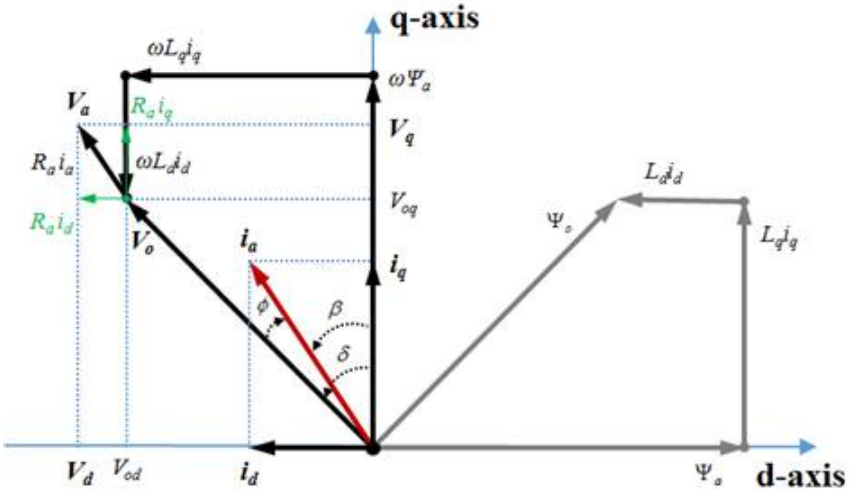

Fig. 10. Vector diagram for interior PMSM using d-q parameters

2.3. 5-phase 10-lead interior PMSM model

Fig. 11 Shows the symbolic structure of an independent 5-phase interior PMSM which consists of phase resistances, self-inductances, mutual inductances, and back-EMFs. Each phase in the motor is offset by a 72 degree electrical angle.

The stator voltage equation of the interior PMSM in this system is given as:

$$V_{abcde} = R_s + \frac{d\lambda_{abcde(s)}}{dt} + e_{abcde} = R_s i_{abcde} + L_s \frac{di_{abcde}}{dt} + e_{abcde} \tag{20}$$

where R_s is the stator resistance, and e_{abcde} is the back-EMF, which is a function of the field flux ($\lambda_{abcde(f)}$).

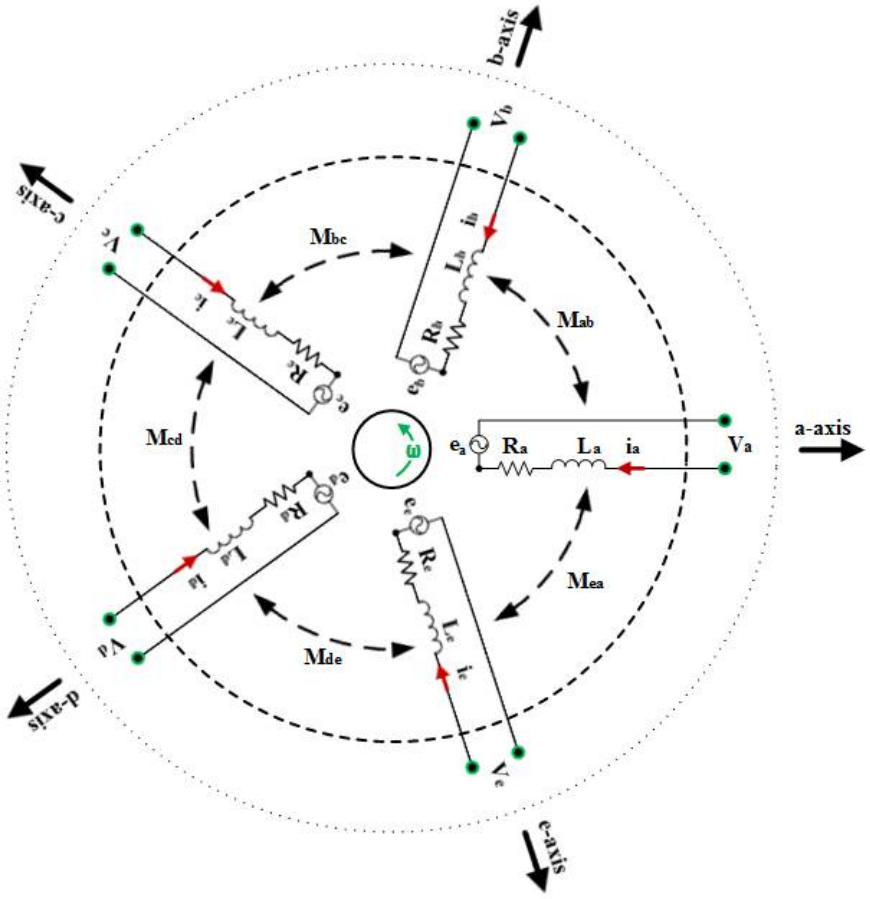

Fig. 11. Symbolic structure of 5-phase 10-lead interior PMSM

Therefore, the final form of the 5-phase 10-lead interior PMSM voltage equation can be rewritten as:

$$\begin{bmatrix} V_a \\ V_b \\ \vdots \\ V_k \\ V_l \end{bmatrix} = \begin{bmatrix} R_s & 0 & 0 & \cdots & 0 \\ 0 & R_s & 0 & \cdots & 0 \\ \vdots & \vdots & \ddots & \vdots & \vdots \\ 0 & 0 & \cdots & R_s & 0 \\ 0 & 0 & \cdots & 0 & R_s \end{bmatrix} \begin{bmatrix} i_a \\ i_b \\ \vdots \\ i_k \\ i_l \end{bmatrix} + \begin{bmatrix} L_{aa} & M_{ab} & M_{ac} & M_{ad} & M_{ae} \\ M_{ba} & L_{bb} & M_{bc} & M_{bd} & M_{be} \\ M_{ca} & M_{cb} & L_{cc} & M_{cd} & M_{ce} \\ M_{da} & M_{db} & M_{dc} & L_{dd} & M_{de} \\ M_{ea} & M_{eb} & M_{ec} & M_{ed} & L_{ee} \end{bmatrix} \left(\frac{d}{dt}\right) \begin{bmatrix} i_a \\ i_b \\ i_c \\ i_d \\ i_e \end{bmatrix} + \begin{bmatrix} e_a \\ e_b \\ e_c \\ e_d \\ e_e \end{bmatrix} \tag{21}$$

From inductance voltage equation, the differential form of the multi-phase inductor voltage equation is:

$$[V_L] = [L_s] \times (\frac{d}{dt}) \times [i_s] \tag{22}$$

The voltage, current, and inductance matrices are the given by:

$$[V_L] = \begin{bmatrix} V_{L_a} & V_{L_b} & V_{L_c} & V_{L_d} & V_{L_e} \end{bmatrix} \tag{23}$$

$$[i_s] = \begin{bmatrix} i_a & i_b & i_c & i_d & i_e \end{bmatrix} \tag{24}$$

$$[L_s] = \begin{bmatrix} L_{aa} & M_{ab} & M_{ac} & M_{ad} & M_{ae} \\ M_{ba} & L_{bb} & M_{bc} & M_{bd} & M_{be} \\ M_{ca} & M_{cb} & L_{cc} & M_{cd} & M_{ce} \\ M_{da} & M_{db} & M_{dc} & L_{dd} & M_{de} \\ M_{ea} & M_{eb} & M_{ec} & M_{ed} & L_{ee} \end{bmatrix} \tag{25}$$

After further manipulation, (23) can be written as:

$$\Delta[i_s] = \begin{bmatrix} i_{s,n} \end{bmatrix} - \begin{bmatrix} i_{s,n-1} \end{bmatrix} = [L_s]^{-1} \times [V_L] \times \Delta T \tag{26}$$

$$\begin{bmatrix} i_{s,n} \end{bmatrix} = \begin{bmatrix} i_{s,n-1} \end{bmatrix} + \left([L_s]^{-1} \times [V_L] \times \Delta T \right) \tag{27}$$

$$\begin{bmatrix} i_{a,n} \\ i_{b,n} \\ i_{c,n} \\ i_{d,n} \\ i_{e,n} \end{bmatrix} = \begin{bmatrix} i_{a,n-1} \\ i_{b,n-1} \\ i_{c,n-1} \\ i_{d,n-1} \\ i_{e,n-1} \end{bmatrix} + \left(\begin{bmatrix} L_{aa} & M_{ab} & M_{ac} & M_{ad} & M_{ae} \\ M_{ba} & L_{bb} & M_{bc} & M_{bd} & M_{be} \\ M_{ca} & M_{cb} & L_{cc} & M_{cd} & M_{ce} \\ M_{da} & M_{db} & M_{dc} & L_{dd} & M_{de} \\ M_{ea} & M_{eb} & M_{ec} & M_{ed} & L_{ee} \end{bmatrix}^{-1} \times \begin{bmatrix} V_{L_a} \\ V_{L_b} \\ V_{L_c} \\ V_{L_d} \\ V_{L_e} \end{bmatrix} \times \Delta T \right) \tag{28}$$

Based on (29), the simulated inductor, which has self-inductance (L_{ii}) and mutual-inductance components (M_{ij}), can be modeled as the load of the inverter using a controlled current source.

2.4. Reference frame transformation for 5-phase PMSM

Fig. 12 shows the conceptual diagram of the reference frame transformation for the 5-phase Interior PMSM. The AC currents can be transferred into DC currents by using the Clarke transformation and Park transformation. The DC currents are easily controlled by PI controllers. The windings are phase-shifted by 72˚, and the saturation of the iron will be neglected.

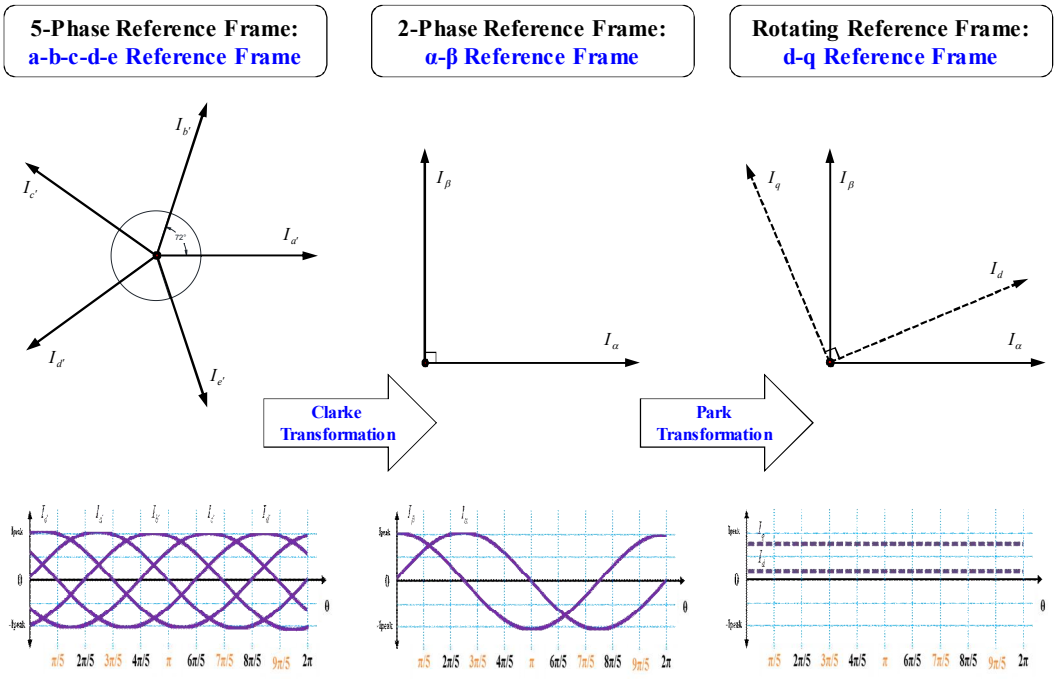

Fig. 12. Conceptual diagram of the reference frame transformation

In general, the voltage equation which describes the electrical behavior of the machine is:

$$V_s = R_s I_s + \frac{d\lambda_s}{dt} \tag{29}$$

where $\lambda_s = L_s I_s$.

Since the inductance matrix varies with the rotor position, the second term of the voltage equation can be written as:

$$\frac{d\lambda_s}{dt} = L_s \frac{dI_s}{dt} + \frac{dL_s}{dt} I_s \tag{30}$$

The second term in the above equation can be written using the chain rule as:

$$\frac{dL_s}{dt} I_s = \frac{dL_s}{d\theta_{rm}} \times \frac{d\theta_{rm}}{dt} \times I_s \tag{31}$$

After defining the rotor mechanical speed as:

$$\omega_{rm} = \frac{d\theta_{rm}}{dt} \tag{32}$$

The term can be rewritten as:

$$\frac{dL_s}{dt} I_s = \omega_{rm} \times \frac{dL_s}{d\theta_{rm}} \times I_s \tag{33}$$

Therefore, the second term can be written in the form as:

$$\frac{d\lambda_s}{dt} = L_s \frac{dI_s}{dt} + \omega_{rm} \times \frac{dL_s}{d\theta_{rm}} \times I_s \tag{34}$$

Substituting the equation 35 in 30 yields the voltage equation in the a-b-c-d-e reference frame system.

$$V_s = R_s I_s + \frac{d\lambda_s}{dt} = R_s I_s + L_s \frac{dI_s}{dt} + \omega_{rm} \times \frac{dL_s}{d\theta_{rm}} \times I_s \tag{35}$$

The voltage equations describe both the transient and steady state behavior of a 5-phase machine. These equations are complex due to the degree of coupling between stator windings since the mutual inductances are a function of the rotor position.

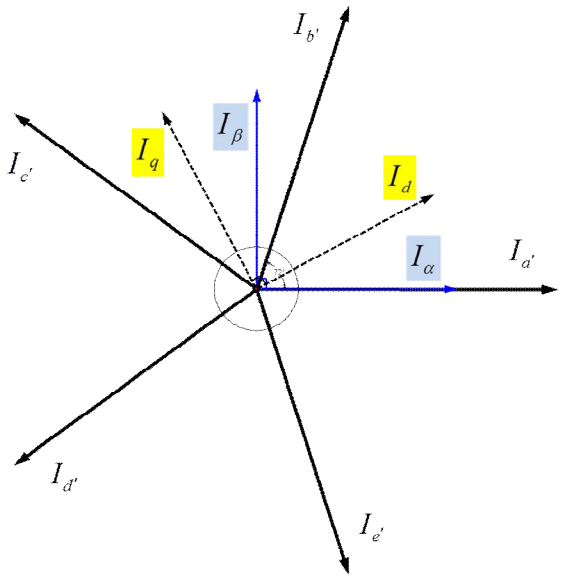

Fig. 13. Relations between each reference frame

From the a-b-c-d-e reference frame, the I_α and I_β components in Fig. 13 can be defined as:

$$I_\alpha = I_{a'} + I_{b'}\cos(\frac{2\pi}{5}) - I_{c'}\cos(\frac{\pi}{5}) - I_{d'}\cos(\frac{\pi}{5}) + I_{e'}\cos(\frac{2\pi}{5}) \tag{36}$$

$$I_{\beta} = I_{a'} sin(0) + I_{b'} \sin(\frac{2\pi}{5}) + I_{c'} \sin(\frac{\pi}{5}) - I_{d'} \sin(\frac{\pi}{5}) - I_{e'} \sin(\frac{2\pi}{5}) \tag{37}$$

This transformation needs $\sqrt{\frac{2}{5}}$ constant between the a-b-c-d-e reference frame and the α-β reference frame because I_{α} equals to $\sqrt{\frac{2}{5}}$ times I_{Ph} when $|I_{a'}| = |I_{b'}| = |I_{c'}| = |I_{d'}| = |I_{e'}| = I_{Ph}$. Therefore, the transformation to simplify the system could be as follows.

$$T(\theta) = \sqrt{\frac{2}{5}} \times \begin{matrix} \alpha \\ \beta \\ x \\ y \\ 0 \end{matrix} \begin{bmatrix} \cos\theta & \cos(\theta - \frac{2\pi}{5}) & \cos(\theta - \frac{4\pi}{5}) & \cos(\theta + \frac{4\pi}{5}) & \cos(\theta + \frac{2\pi}{5}) \\ \sin\theta & \sin(\theta - \frac{2\pi}{5}) & \sin(\theta - \frac{4\pi}{5}) & \sin(\theta + \frac{4\pi}{5}) & \sin(\theta + \frac{2\pi}{5}) \\ \cos\theta & \cos(\theta - \frac{2\pi}{5}) & \cos(\theta - \frac{4\pi}{5}) & \cos(\theta + \frac{4\pi}{5}) & \cos(\theta + \frac{2\pi}{5}) \\ \sin\theta & \sin(\theta - \frac{2\pi}{5}) & \sin(\theta - \frac{4\pi}{5}) & \sin(\theta + \frac{4\pi}{5}) & \sin(\theta + \frac{2\pi}{5}) \\ 1/\sqrt{2} & 1/\sqrt{2} & 1/\sqrt{2} & 1/\sqrt{2} & 1/\sqrt{2} \end{bmatrix} \tag{38}$$

An extra x-y set of components appear, and there is no coupling of x-y set with d-q component and the rotor circuit.

In order to transform the voltage equations into the stationary α-β reference frame, the stator voltage equation is multiplied by the transformation function.

$$T(\theta)V_s = T(\theta)R_s I_s + T(\theta)\frac{d\lambda_s}{dt} \tag{39}$$

The second term in the above equation can be written using the chain rule again as:

$$T(\theta)V_s = T(\theta)R_sI_s + T(\theta)\frac{d\lambda_s}{dt} = T(\theta)R_sI_s + \frac{dT(\theta)}{dt}T(\theta)^{-1}T(\theta)\lambda_s \tag{40}$$

Multiplying the stator flux linkage by the transformation function yields the stator flux linkages in the d-q reference frame, given by:

$$T(\theta)\lambda_s = T(\theta)L_sT(\theta)^{-1}T(\theta)I_s = L_{dqs}(\theta)I_{dqs} = \lambda_{dqs} \tag{41}$$

$$\begin{aligned} V_{dqs} &= T(\theta)V_s \\ I_{dqs} &= T(\theta)I_s \\ \lambda_{dqs} &= T(\theta)\lambda_s \end{aligned} \tag{42}$$

The machine's voltage equations in the common reference frame can be written as:

$$\begin{aligned} V_{ds} &= R_sI_{ds} - \omega_{rm}\lambda_{qs} + \frac{d}{dt}\lambda_{ds} + \omega_{rm}\lambda_{Mag.} \\ V_{qs} &= R_sI_{qs} + \omega_{rm}\lambda_{ds} + \frac{d}{dt}\lambda_{qs} \\ V_{xs} &= R_sI_{xs} + \frac{d}{dt}\lambda_{xs} \\ V_{ys} &= R_sI_{ys} + \frac{d}{dt}\lambda_{ys} \\ V_{0s} &= R_sI_{0s} + \frac{d}{dt}\lambda_{0s} \end{aligned} \tag{43}$$

The transformation of flux linkage equation results in:

$$\begin{aligned} \lambda_{ds} &= (L_{ls} + L_m)I_{ds} + \lambda_{Mag.} \\ \lambda_{qs} &= (L_{ls} + L_m)I_{qs} \\ \lambda_{xs} &= L_{ls}I_{xs} \\ \lambda_{ys} &= L_{ls}I_{ys} \\ \lambda_{0s} &= L_{ls}I_{0s} \end{aligned} \tag{44}$$

Finally, transformation of the original torque equation yields:

$$T_e = \frac{5}{2} \times \frac{P}{2} \times (L_{ds} - L_{qs}) I_{ds} I_{qs} + \frac{5}{2} \times \frac{P}{2} \times \lambda_{Mag.} I_{qs} \quad (45)$$

The difference between a 3-phase machine and a 5-phase machine model is the extra x-y set of components that exist only in a 5-phase machine. However this extra set are non-flux and non-torque producing components and simply add to the extra losses in the machine. The d-q components produce torque and the remaining component simply causes losses in the machine. In a general property of multi-phase system, d-q components produce the fundamental, 9th, 11th…, x-y components produce 3rd, 7th, 13th…, and a multiple of the 5th harmonic is produced due to zero-sequence components [28]-[32].

2.5. Summary

This chapter presented the mathematical modeling of interior PMSM after Permanent Magnet Synchronous Motors are classified. It was shown that there are mainly two types: Surface-mounted Permanent Magnet Synchronous Motor (SPMSM) or Interior Permanent Magnet Synchronous Motor (IPMSM) depending on how the magnets are attached to the rotor.

It was shown how to derive the output torque equation for conventional 3-phase interior PMSM with and without core loss from the analytical model in a-b-c reference frame and d-q reference frame. 5-phase 10-lead interior PMSM is modeled as the load of the inverter using a controlled current source using self-inductance and mutual-inductance components.

In addition, reference frame transformation for 5-phase machine was introduced using conceptual diagram and relations of each reference frame. The original torque equation is derived through the transformation and the difference between a 3-phase machine and a 5-phase machine model is compared. The extra x-y set of components that exist only in a 5-phase machine is explained in detail.

3. 5-PHASE 10-LEAD INTERIOR PMSM DESIGN*

3.1. Introduction

This chapter is devoted to design the 5-phase interior PMSM with the proposed design procedure. The design flow will be explained with the basic, screening, and optimal design steps. Finally, the design results will be simulated and confirmed with FEA.

Table 1 shows the design specifications. The rated torque is 7.96Nm at 3kW with a speed of 3600rpm. The DC link voltage is 150V, and the motor will be air-cooled with an air-gap, 0.7mm. The existing motor provides the mechanical design constraints: the size and the amount of copper and magnet used.

When designing an Interior PMSM, two operating regions should be considered. The continuous rating region is the range where the motor will be operated all the time, and the intermittent rating region is the range when motor needs to generate the maximum torque or speed. These two conditions should be considered as shown in Fig. 14.

---

* Part of this section is reprinted with permission from:
"Integrated Torque Ripple Analysis Method for Multi-Phase Motors" by Jae-Bum Park, M. Johnson, and H.A. Toliyat, *Proc. 2013 IEEE International Electric Machines and Drives Conf., pp*. 294-299. Copyright 2013 by IEEE and
"Magnet Shape Optimization for Double Layer Rotor Interior PMSM using RSM" by Jae-Bum Park, M. Johnson, and H.A. Toliyat, in *Proc. 2014 IEEE Industrial Electronics, Control, and Instrumentation Conf. (IECON), pp*. 695-701. Copyright 2014 by IEEE.

Table 1. 3kW 5-phase 10-lead interior PMSM design specifications

Item		Specification	Unit
Given Design Conditions	Rated Torque (Power)	7.96 (3.0)	Nm (kW)
	Max. Torque (Power)	9.23 (3.5)	Nm (kW)
	Rated Speed	3600	Rpm
	DC Link Voltage (Vdc)	150	V
	Current Density	2 ~5	A/mm^2
	Air-Gap	0.7	mm
Design Constraints	Stator Outer Diameter	190	mm
	Axial Length	65	mm
	Efficiency	Over 90	%
	Slot Fill Factor	Less than 50	%
	Copper	60	Turns/Phase
	Magnet	32448	mm^2

To generate 3kW output power, the inverter capacity needs to be calculated, an appropriate power supply is necessary.

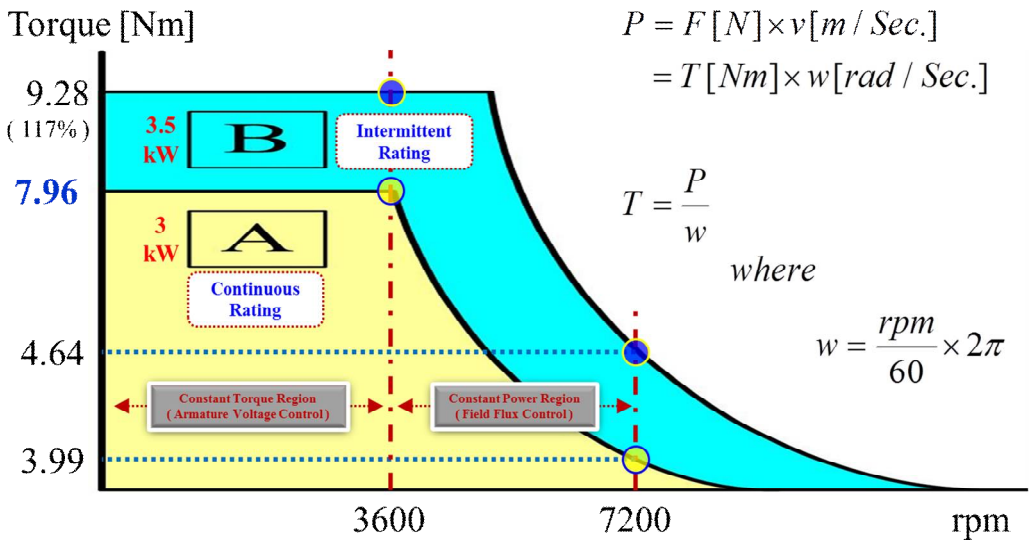

Fig. 14. 5-phase 10-lead interior PMSM design points

3.2. Proposed design procedure

3.2.1. Design flow chart

As indicated in the flowchart in Fig. 15, the proposed design procedure will use the basic arrangement to obtain the stator core and winding designs with a conventional design method based on the calculated air-gap flux per phase. The rotor design is more complicated and important, so a fractional design method is used as a screening process to find the main design parameters, and then the main parameters will be optimized using the response surface method and the Finite Element Method.

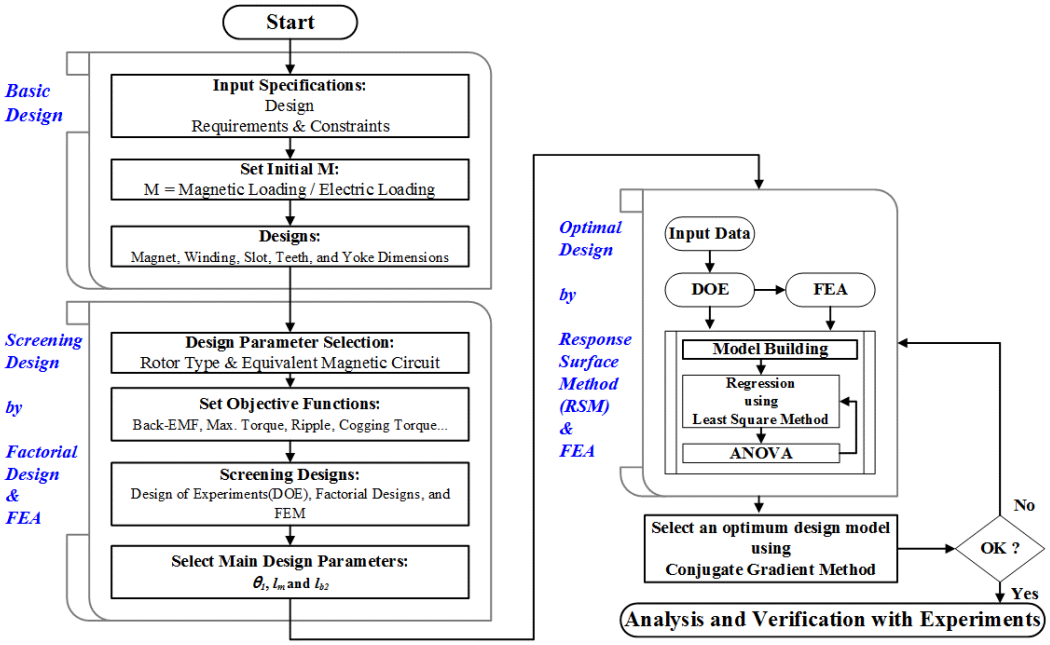

Fig. 15. Flow chart of the proposed design procedure

3.2.2. Factorial design method

Factorial designs are extensively used in manufacturing industry studies and experiments because they typically involve systems with numerous factors. This approach examines a system's input-output relationship to achieve one of several goals: identify important design variables, optimize a product or process design, and achieve robust performance in a system. The joint effects based on a response variable reveal the main effects of each factor as well as their interactions with other factors. Therefore, important design variables can be identified with this statistical methodology [33]-[36].

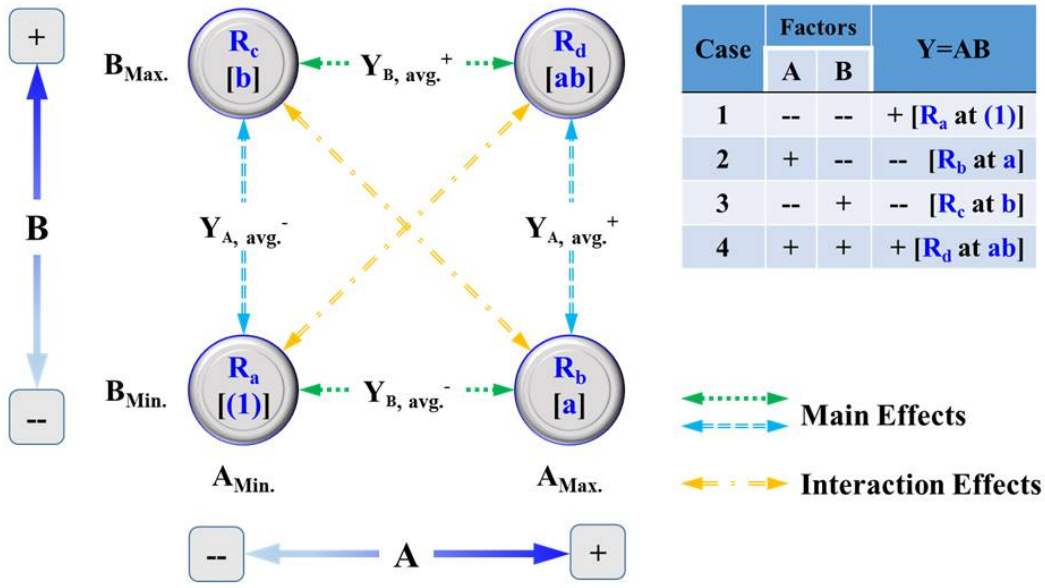

Case	Factors		Y=AB
	A	B	
1	--	--	+ [R_a at (1)]
2	+	--	-- [R_b at a]
3	--	+	-- [R_c at b]
4	+	+	+ [R_d at ab]

Fig. 16. Two-level factorial design diagram

The number of data points varies the number of levels. For a 2-level design, the minimum and maximum points are generally used. The simplest factorial design is one with two factors which is also called a two-level factorial design, or a 2^2 factorial design. Sometimes, the levels of the factors may be referred to as "low" and "high" or "min." and "max." as shown in Fig. 16. In Fig 16, the symbols (R_a, R_b, R_c, and R_d) represent response variables taken at the design points ((1), a, b, and ab).

The main effect of factor "A" (E_A) is the difference in the average response of the two points ("a" and "ab") on the right-hand side and the two points ("(1)" and "b") on the left-hand side of the square diagram in Fig. 16. $Y_{A, avg.}^{-}$ indicates the average response at the points where "A" is at the low level, and $Y_{A, avg.}^{+}$ denotes the average response at the points where "A" is at the high level. Similarly, the main effect of factor "B" (E_B) is found as the difference between the average value of the two points ("(1)" and "a") on the

bottom of the square ($Y_{B,\,avg.}^{-}$) and the average value of the two points ("b" and "ab") on the top of the square ($Y_{B,\ avg.}^{+}$). The interaction effect (E_{AB}) is the average of the responses on the right-to-left diagonal points ("ab" and "(1)") minus the average of the responses on the left-to-right diagonal points ("b" and "a") in the square. The formulas for these effects are derived in (47), (48), and (49) [37].

$$\begin{aligned} E_A &= Y_{A,avg.}^{+} - Y_{A,avg.}^{-} \\ &= \frac{R_d + R_b}{2} - \frac{R_c + R_a}{2} = \frac{1}{2}\left(R_d + R_b - R_c - R_a\right) \end{aligned} \tag{46}$$

$$\begin{aligned} E_B &= Y_{B,avg.}^{+} - Y_{B,avg.}^{-} \\ &= \frac{R_d + R_c}{2} - \frac{R_b + R_a}{2} = \frac{1}{2}\left(R_d + R_c - R_b - R_a\right) \end{aligned} \tag{47}$$

$$E_{AB} = \frac{R_d + R_a}{2} - \frac{R_b + R_c}{2} = \frac{1}{2}\left(R_d + R_a - R_b - R_c\right) \tag{48}$$

In order to obtain experimental verification, the number of samples used is equal to the number of prototypes which must be built. Therefore, cost implications must be considered when deciding the number of samples used, in a study. For most engineering problems, it is sufficient to only consider information related to the main effects and lower-order interactions, such as second-order interactions realistically as shown in Fig. 17. This pragmatism is why fractional factorial designs are among the most widely used design methods in industry. This approach can identify the factors which have the largest impacts across numerous variables in screening experiments or designs.

No. of Factors	Main Effects	Order of Interactions									No. of Combinations
		2nd	3rd	4th	5th	6th	7th	8th	9th	10th	
2	2	1									4
3	3	3	1								8
4	4	6	4	1							16
5	5	10	10	5	1						32
6	6	15	20	15	6	1					64
7	7	21	35	35	21	7	1				128
8	8	28	56	70	56	28	8	1			256
9	9	36	84	126	126	84	36	9	1		512
10	10	45	120	210	252	210	120	45	10	1	1024

Fig. 17. Two-level full factorial

The three key assumptions inherent in fractional factorial designs are listed as follows:

1) The sparsity of effects principle: There may be lots of factors, but few are important and the system is dominated by the main effects and low-order interactions.

2) The projection property: Every fractional factorial contains full factorials in fewer factors.

3) Sequential experimentation: More runs can be added to a fractional factorial to resolve difficulties or ambiguities in interpretation.

Using these principles, a fractional design which estimates the main effects and provides some insight into the two-factor interactions can be a reasonable study approach [38]-[41]. (50) provides the notation for a two-level fractional factorial design, and Fig. 18 illustrates the complete fractional factorial design which has 7 design parameters and 16 runs as an example.

$$2_R^{k-p} \tag{49}$$

where

2: no. of level for each factor

k: no. of factors included

p: the fraction to be run no. of extra factors that need to be placed into the basic design

R: the resolution of the design (III, IV, and V)

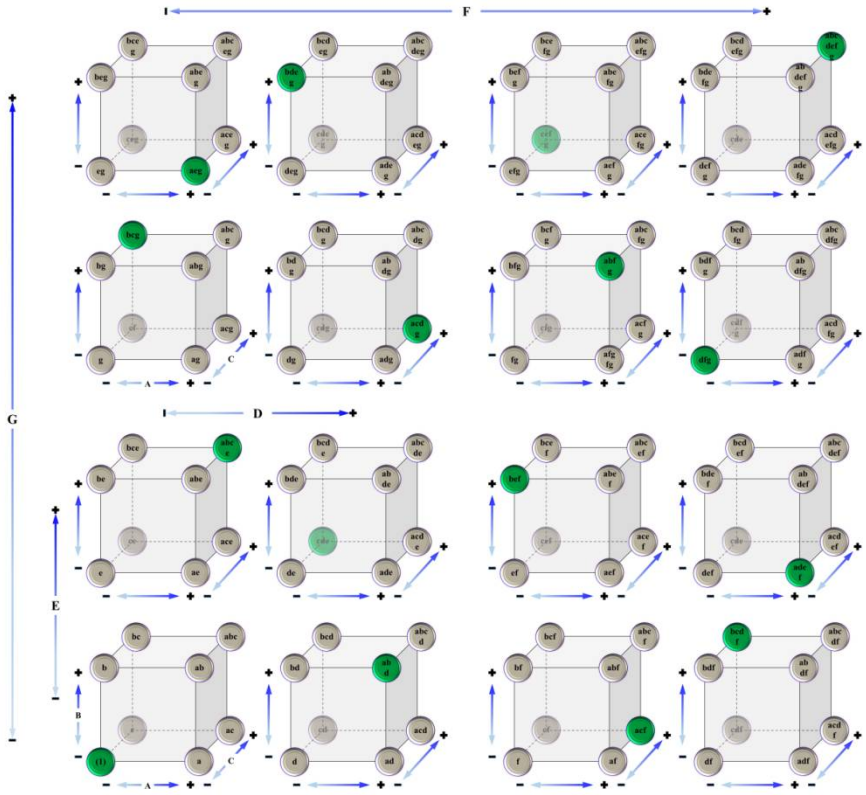

Fig. 18. Projection of the 2^{7-3} Design (16 out of 128).

Based on the treatment combination of the complete design, 16 cube plots of the projection are visualized, and the projection indicates a balanced design in which all

factors occur at low and high levels with the same frequency. That is, the design has good statistical properties despite using only 16 runs out of 128 possible experimental points. Main design variables can be chosen after analyzing the effects of the variables with the minimum experimental points.

3.2.3. Response surface methodology

RSM is a set of useful mathematical and statistical techniques, introduced by Box & Wilson in 1951, which is employed to develop and optimize design parameters. The DOE (Design of Experiments) that finds experiment points for design variables has been researched to create the response surface design [42].

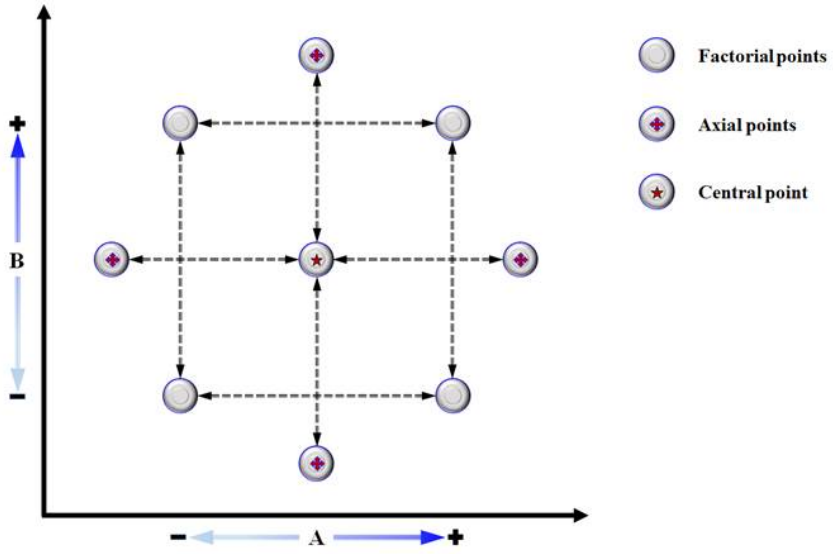

Fig. 19. CCD for 2-level 2 factors.

The least square method and variable selection method are used to make an approximate function for each objective function, and ANOVA (analysis of variance) is then used to evaluate the function. Among many DOEs, the Central Composite Design (CCD) that is generally used for polynomial models is chosen because maximum or minimum values can be obtained with the number of minimum experiment points for the system [43]-[47]. Fig. 19 and Fig. 20 show the experiment points for CCD when there are two factors and three factors for 2-Level respectively.

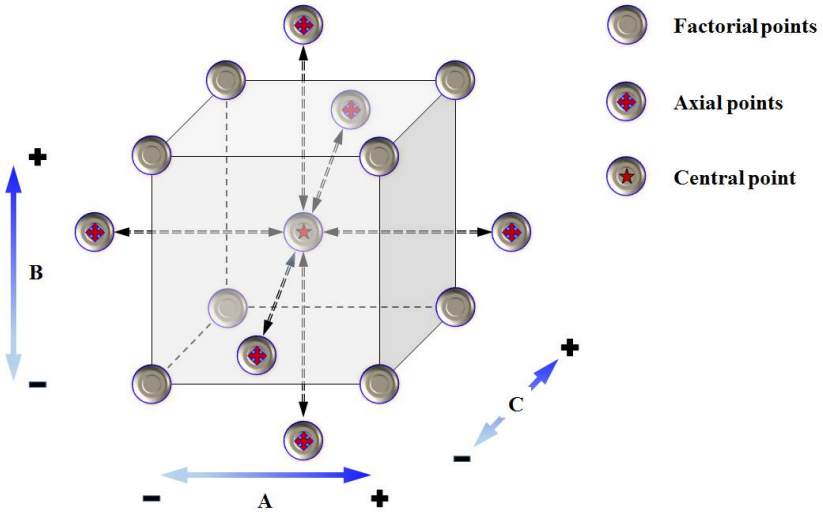

Fig. 20. CCD for 2-level 3 factors.

The number of the CCD experiment can be calculated as follows.

$$n = 2^k + 2k + n_c \tag{50}$$

where

2^k: The number of the 2-level factorial design

$2k$: The number of axial point

n_c: The number of replication for the center point

RSM statistically approximates the relationship between the response value, y, which is obtained from FEM analysis and the true value. The response value obtained from an experiment has an error, and the equation can be expressed in (52) [48].

$$y = f(x_1, x_2, \cdots, x_m) + \varepsilon \tag{51}$$

where

$u = f(x_1, x_2, \cdots, x_m)$: The true response function that has m design variables

ε : The random error component that includes measurement error on the response and is inherent in the process or system

For most of the response surfaces, the approximation functions are polynomials because of their simplicity, but the functions are not explicitly required to be polynomials. The second-order response surface model is described as follow from a Taylor series expansion of (53) [49]-[53].

$$y = \beta_0 + \sum_{j=1}^{m} \beta_j x_j + \sum_{j=1}^{m} \beta_{jj} x_j^{\,2} + \sum_{i=1}^{m-1} \sum_{j=i+1}^{m} \beta_{ij} x_i x_j + \varepsilon \tag{52}$$

where

β: regression coefficients

m: the number of variables.

Minitab, the leading statistical software, was used to plot the response surfaces with the CCD to analyze the results efficiently and conveniently. Response values of object functions are obtained from performing FEA studies of the experimental cases. To decide the optimal design model, the conjugate gradients method (CGM) was used with the regression coefficients for the response surfaces. The objective function equations can be derived from the response surface analysis.

3.3. Stator slot and rotor pole combination with winding method

3.3.1. Winding factor

Winding factor is an important consideration when choosing stator slot and rotor pole combination because the winding factor is directly proportional to MMF (Magneto motive force). High winding factor means the motor generate high magneto motive force. Winding factor equals to distribution factor.

The distribution factor is the ratio between the geometrical and the arithmetic sum of the phasors of the same phase. The computation can be repeated for each harmonic order, v, which corresponds to an angular displacement $2\pi v/Q$ between the phasors of two adjacent slots. It is worth noting that the distribution factor depends only on the number of spokes per phase q_{ph} of the star of slots, given by $q_{ph} = Q/(mt)$, while it is independent of the machine periodicity, t. Based on the selection of the phasors of each phase, the distribution factor for the main harmonic can be expressed as [54]-[55]:

$$If\ q_{ph}\ is\ odd,\ \ k_d = \frac{\sin(q_{ph} \times \frac{\alpha_{ph}}{4})}{q_{ph} \times \sin(\frac{\alpha_{ph}}{4})} \tag{53}$$

$$If\ q_{ph}\ is\ even,\ \ k_d = \frac{\sin(\frac{q_{ph}}{2} \times \frac{\alpha_{ph}}{2})}{\frac{q_{ph}}{2} \times \sin(\frac{\alpha_{ph}}{2})} \tag{54}$$

where $q_{ph} = Q/(mt)$, $\alpha_{ph} = 2\pi/(Q/t)$

q_{ph}: No. of spokes per phase

α_{ph}: Angle between two spokes

m: No. of phases

t: Machine periodicity

The pitch factor is independent of the star of slots and is computed from the coil throw. The slot pitch y_q, measured in number of slots, is approximated by y_q = round $\{Q/(2p)\}$ with the lowest value equal to unity. The pitch factor of the main harmonic is given by:

$$k_p = \sin\frac{\sigma_w \times v}{2} \tag{55}$$

where $\sigma_w = y_{q,\ Ang.} \times S$

σ_w: Coil span angle

$y_{q,\ Ang.}$: Slot pitch angle

S: No. of coil spans

v: Harmonic order

Fig. 21, 22, and 23 show the winding factor calculations at various combinations of the slots and poles with the difference number of coils spans. The highlighted ones are the best candidates with the mechanical constraints.

Winding Factor ($k_w = k_d * k_p$)								
Poles ($2p$)	2	4	6	8	12	14	16	18
Slots (Q)								
5	0.588	0.951	0.951	0.588	-0.588	-0.951	-0.951	-0.588
10	0.305	0.588	0.799	0.951	0.951	0.799	0.588	0.305
15	0.205	0.401	0.588	0.732	0.951	0.980	0.980	0.951
20	0.155	0.305	0.448	0.588	0.809	0.880	0.951	0.976

Fig. 21. Winding factor when *S*=1.

Winding Factor ($k_w = k_d * k_p$)								
Poles ($2p$)	2	4	6	8	12	14	16	18
Slots (Q)								
5	0.951	0.588	-0.588	-0.951	0.951	0.588	-0.588	-0.951
10	0.581	0.951	0.939	0.588	-0.588	-0.939	-0.951	-0.581
15	0.401	0.732	0.951	0.980	0.588	0.205	-0.205	-0.588
20	0.305	0.581	0.799	0.951	0.951	0.799	0.588	0.305

Fig. 22. Winding factor when *S*=2.

Winding Factor ($k_w = k_d * k_p$)								
Poles ($2p$)	2	4	6	8	12	14	16	18
Slots (Q)								
5	0.951	-0.588	-0.588	0.951	-0.951	0.588	0.588	-0.951
10	0.799	0.951	0.305	-0.588	-0.588	0.305	0.951	0.799
15	0.579	0.937	0.951	0.579	-0.588	-0.937	-0.937	-0.588
20	0.448	0.799	0.976	0.951	0.309	-0.155	-0.588	-0.880

Fig. 23. Winding factor when *S*=3.

There are few possible windings, so Fig. 24 recommends the number of coil spans. Based on the recommendation, 10 slots 4poles, 10 slots 8 poles, 15 slots 4 poles, and 15 slots 6 pole were chosen.

Coil Span (S* = max[int(Q/2p), 1]), Recommendation								
Poles ($2p$)	2	4	6	8	12	14	16	18
Slots (Q)								
5	2.0	1.0	1.0	1.0	1.0	1.0	1.0	1.0
10	5.0	2.0	1.0	1.0	1.0	1.0	1.0	1.0
15	7.0	3.0	2.0	1.0	1.0	1.0	1.0	1.0
20	10.0	5.0	3.0	2.0	1.0	1.0	1.0	1.0

Fig. 24. Recommended coil spans.

Winding Factor ($k_w = k_d * k_p$)								
Poles ($2p$)	2	4	6	8	12	14	16	18
Slots (Q)								
5	0.951	0.951	0.951	0.588	-0.588	-0.951	-0.951	-0.588
10	0.988	0.951	0.799	0.951	0.951	0.799	0.588	0.305
15	0.980	0.937	0.951	0.732	0.951	0.980	0.980	0.951
20	0.988	0.988	0.976	0.951	0.809	0.880	0.951	0.976

Fig. 25. Winding factor at each coil span.

The winding factors of the chosen combinations at each harmonic order are shown in Fig. 26, 27, 28, and 29.

Fig. 30 shows the concentrated winding configuration for 10 slots 8 poles, 10 slots 4 poles, and 15 slots 6 poles, and the 15 slots 4 poles has the distributed winding configuration in Fig. 31. With this information, it is not easy to decide the best condition, so each combination should be further evaluated with the radial force analysis.

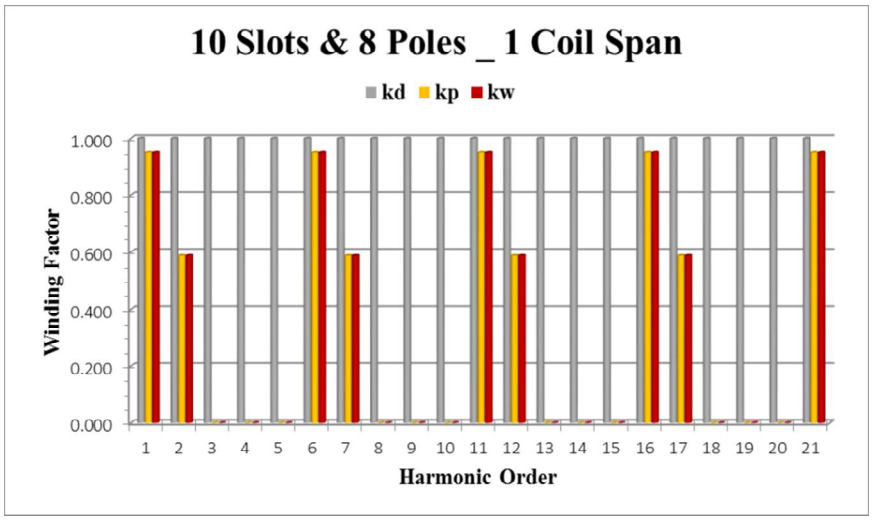

Fig. 26. 10 slots 8 poles winding factor at each harmonic order.

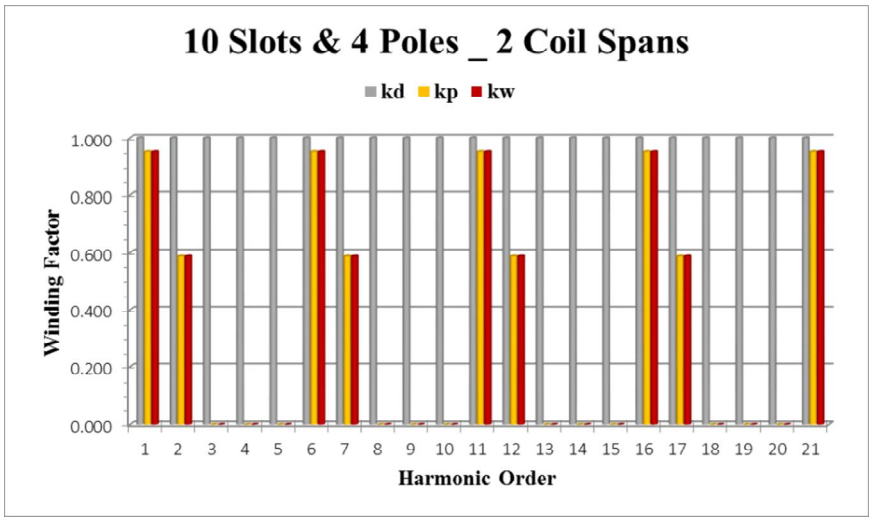

Fig. 27. 10 slots 4 poles winding factor at each harmonic order.

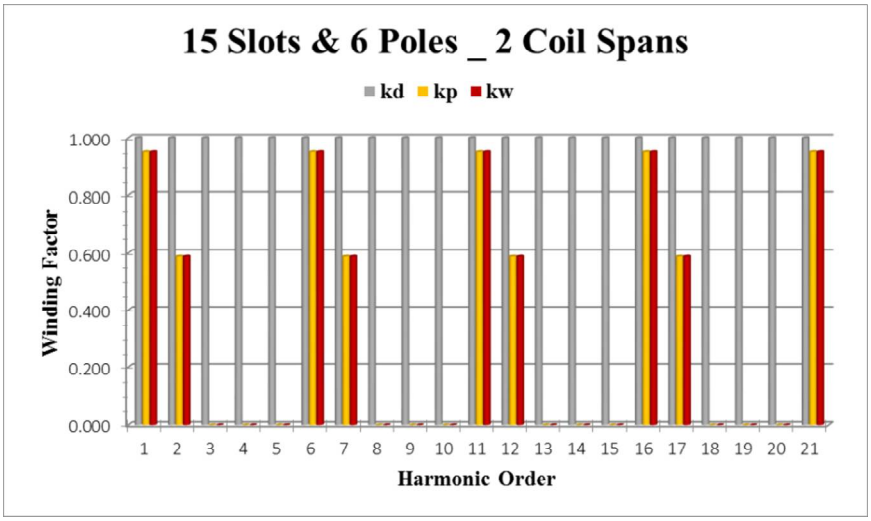

Fig. 28. 15 slots 6 poles winding factor at each harmonic order.

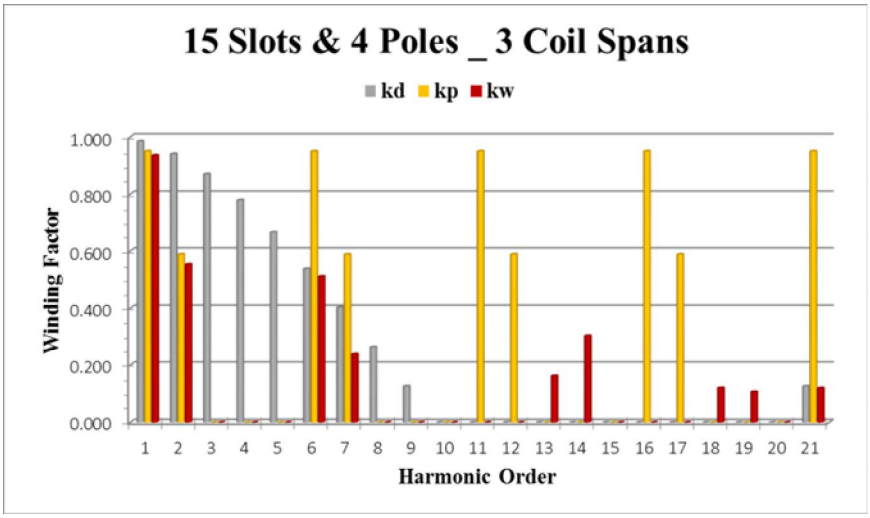

Fig. 29. 15 slots 4 poles winding factor at each harmonic order.

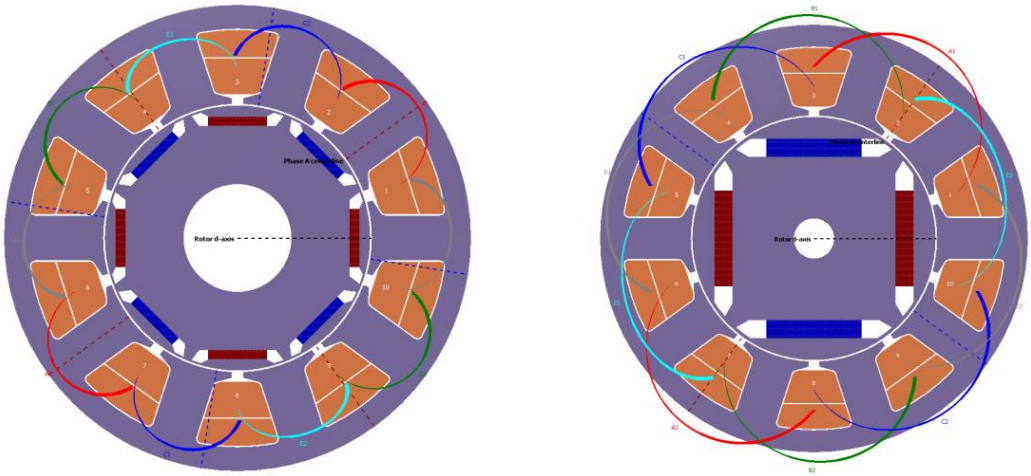

(a) **(b)**

Fig. 30. Winding configuration. (a) 10 slots 8 poles. (b) 10 slots 4 poles.

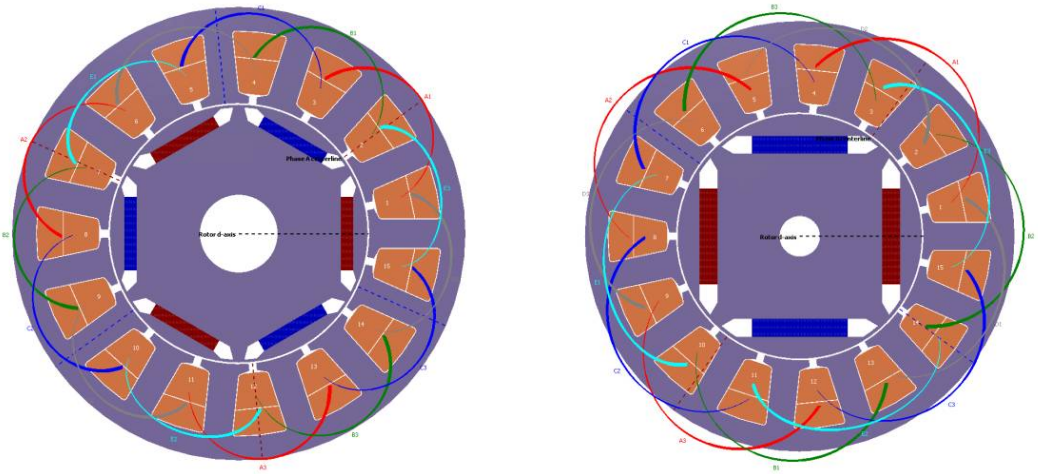

(a) **(b)**

Fig. 31. Winding configuration. (a) 15 slots 6 poles. (b) 15 slots 4 poles.

3.3.2. Air-gap force distribution analysis

There are two types of force when a motor rotates. One is the tangential force which generates torque, and the other is the radial force which is also called normal force. The radial force makes noise and vibration during motor operation. Technically, a radial force is any force that acts in a straight line and often used to describe the influence exerted perpendicular to the centerline or axis of an object traveling in an orbital path in physics. The aspect of the radial force changes depending on the combination of the stator slot and rotor pole and rotor shape too in electrical machines [56]-[59]. Fig. 32 shows the definition of the forces that derive the electromagnetic torque using an energy balance approach.

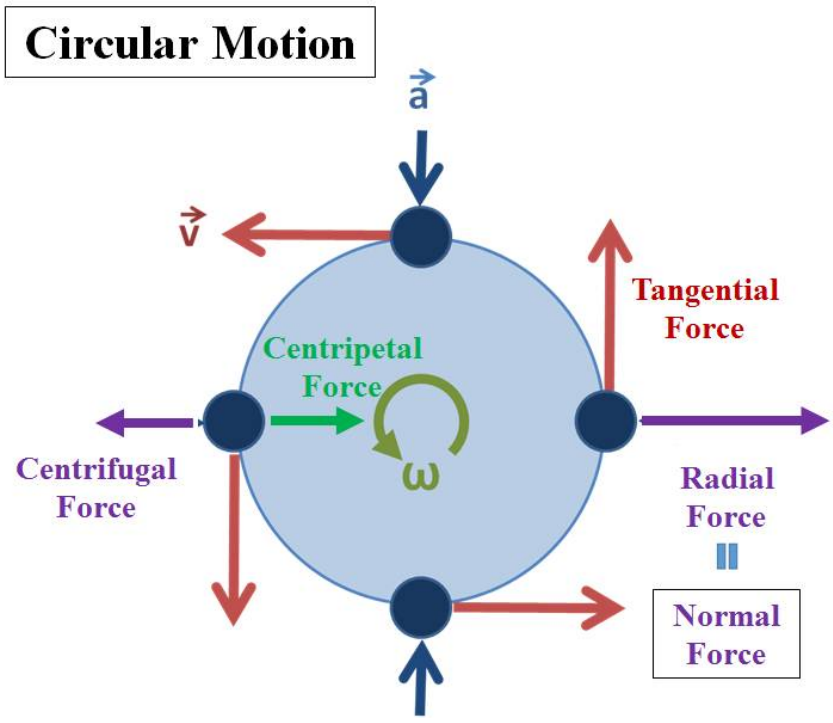

Fig. 32. Force definition.

When there is a circular motion, a radial force and a tangential force exist, and they can be calculated with the radial magnetic flux density and tangential magnetic flux density which can be simulated from FEA [60]-[62].

$$F_r = \frac{1}{2\mu_0}(B_r{}^2 - B_t{}^2) \ [\mathrm{N/m^2}]$$
$$F_t = \frac{1}{\mu_0} B_r B_t \ [\mathrm{N/m^2}] \tag{56}$$

where F_r is the radial component of force density (N/m^2), Ft is the tangential component of force density (N/m^2), B_r is the radial component of the magnetic flux density, B_t is the tangential component of magnetic flux density, and μ_0 is the permeability of free space.

Fig. 33 depicts the air-gap force distribution at 0° for the 10-slot 8-pole combination, and the radial and tangential forces were obtained every 45° electrical angle in Fig. 35, 37, and 39.

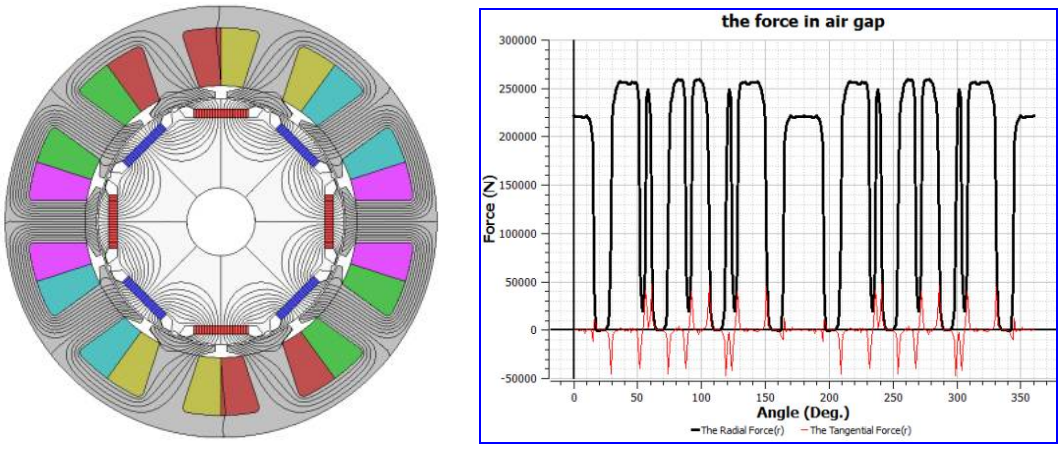

(a) **(b)**

Fig. 33. 10 slots 8 poles at 0°. (a) Flux line distribution. (b) Force distribution in air-gap.

To visualize the distribution more easily, both of them are plotted in the polar axis in Fig. 34, 36, 38, and 40.

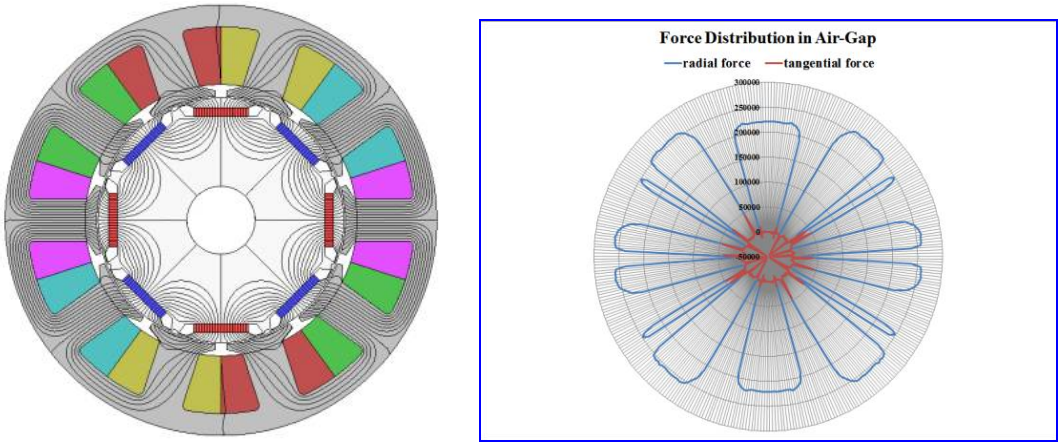

(a) **(b)**

Fig. 34. 10 slots 8 poles at 0˚. (a) Flux line distribution. (b) Air-gap force distribution in polar axis.

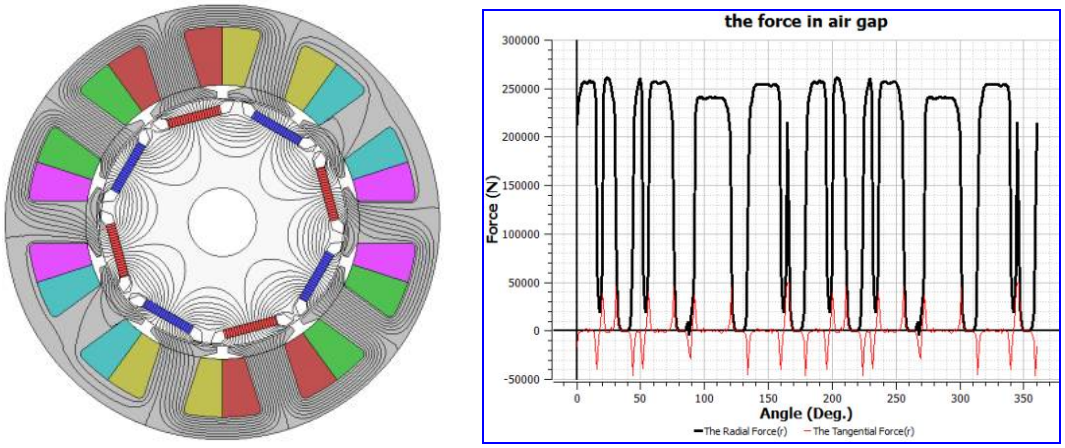

(a) **(b)**

Fig. 35. 10 slots 8 poles at 15˚. (a) Flux line distribution. (b) Force distribution in air-gap.

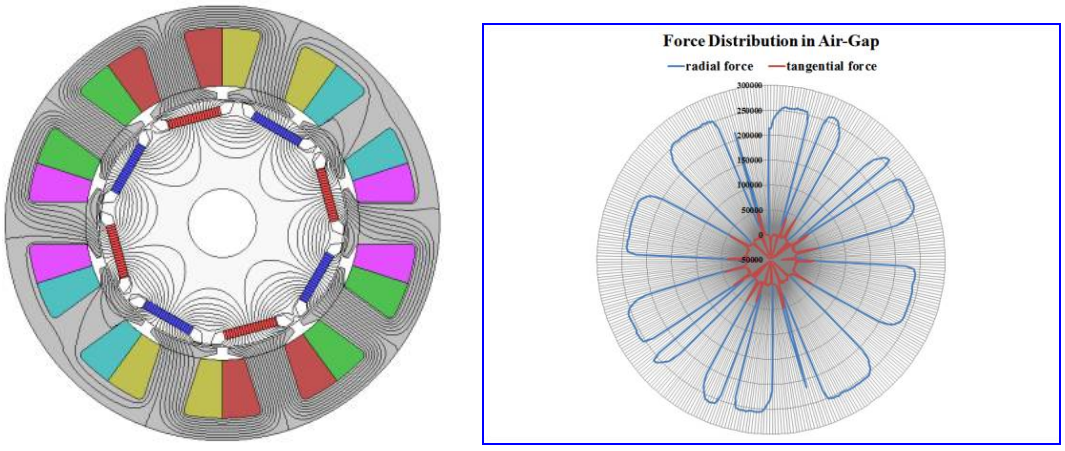

(a) **(b)**

Fig. 36. 10 slots 8 poles at 15˚. (a) Flux line distribution. (b) Air-gap force distribution in polar axis.

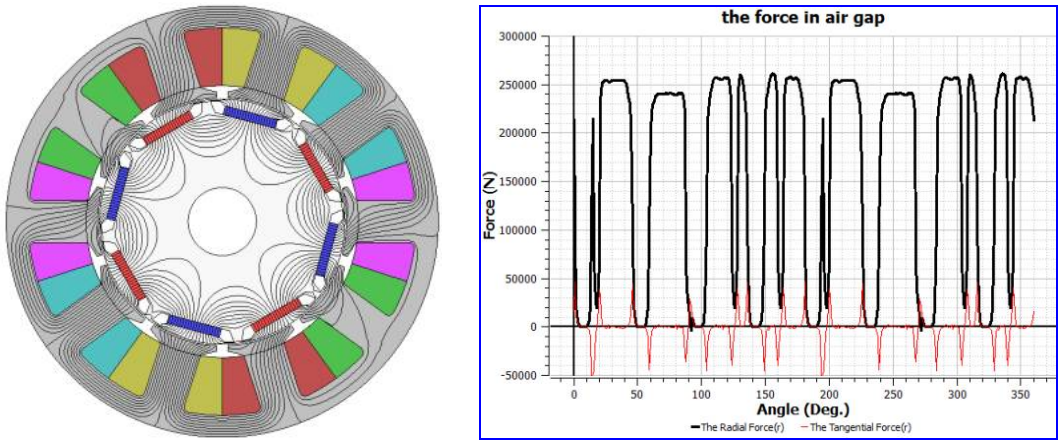

(a) **(b)**

Fig. 37. 10 slots 8 poles at 30˚. (a) Flux line distribution. (b) Force distribution in air-gap.

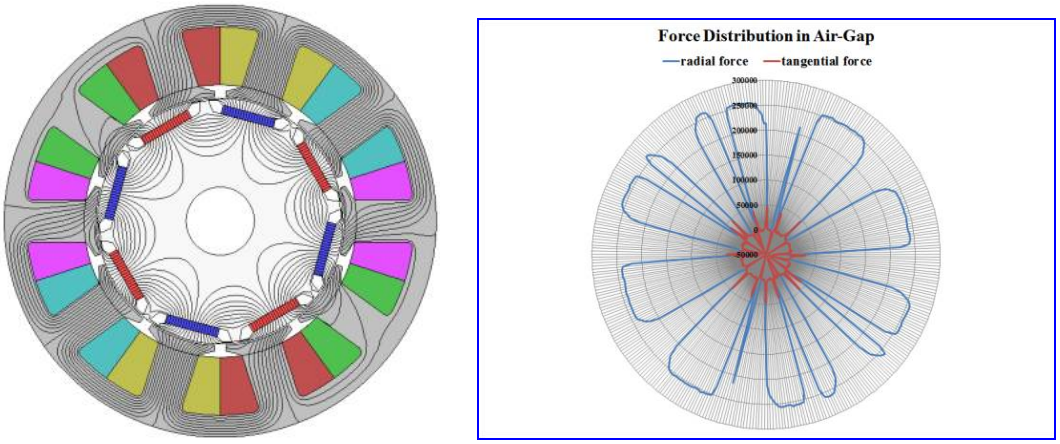

(a) **(b)**

Fig. 38. 10 slots 8 poles at 30˚. (a) Flux line distribution. (b) Air-gap force distribution in polar axis.

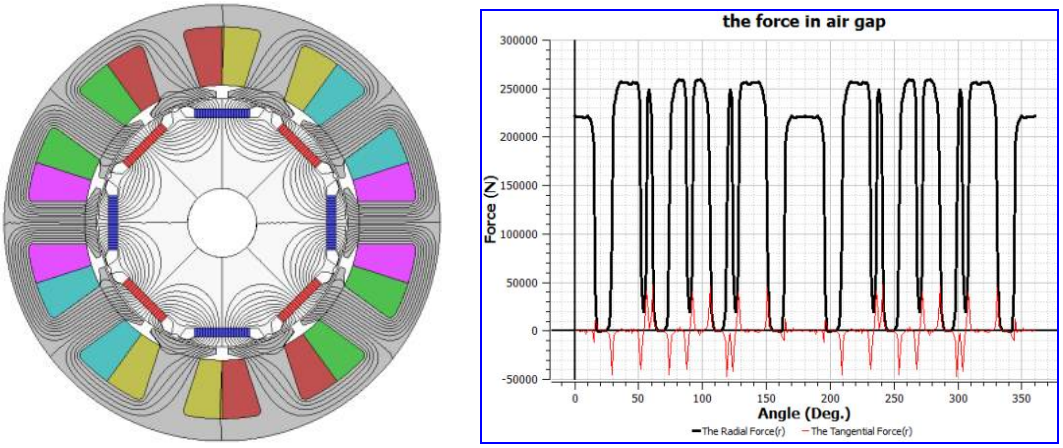

(a) **(b)**

Fig. 39. 10 slots 8 poles at 45˚. (a) Flux line distribution. (b) Force distribution in air-gap.

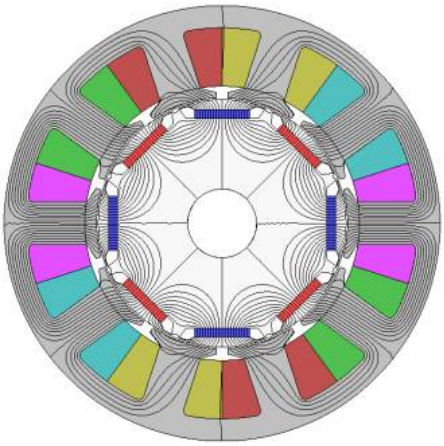

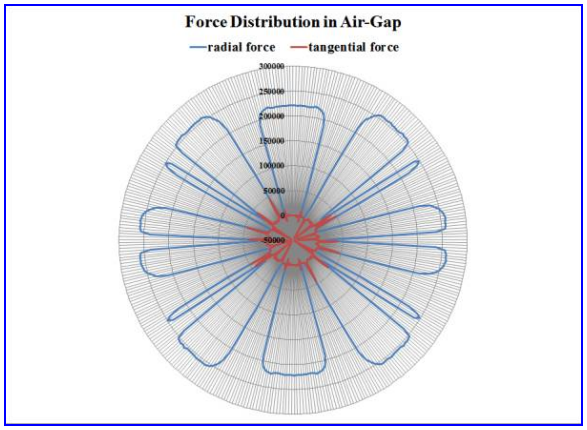

(a) **(b)**

Fig. 40. 10 slots 8 poles at 45°. (a) Flux line distribution. (b) Air-gap force distribution in polar axis.

From Fig. 41 to Fig. 44, four best candidates are compared, and the 10-slot 8-pole has the most evenly balanced radial force distribution as shown in Fig. 41.

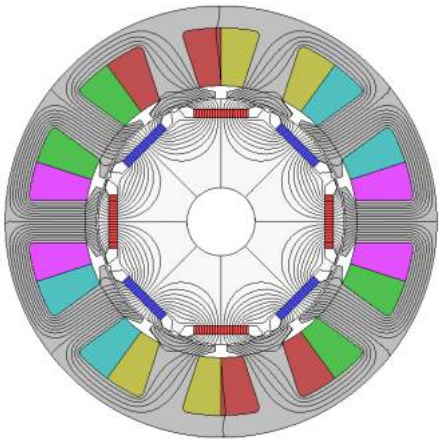

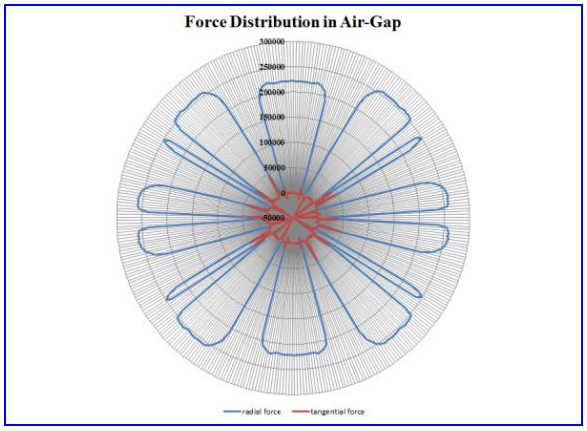

(a) **(b)**

Fig. 41. 10 slots 8 poles at 0°. (a) Flux line distribution. (b) Air-gap force distribution in polar axis.

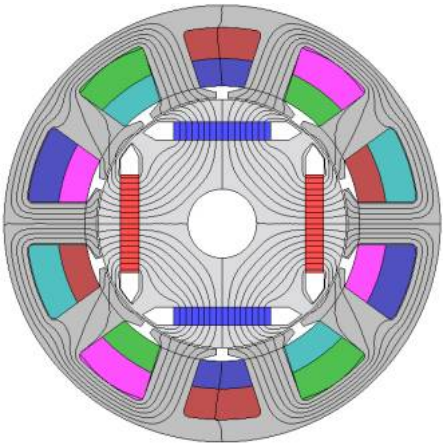

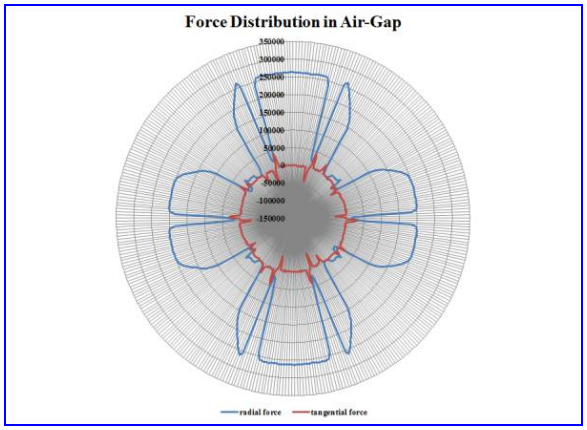

(a) **(b)**

Fig. 42. 10 slots 4 poles at 0˚. (a) Flux line distribution. (b) Air-gap force distribution in polar axis.

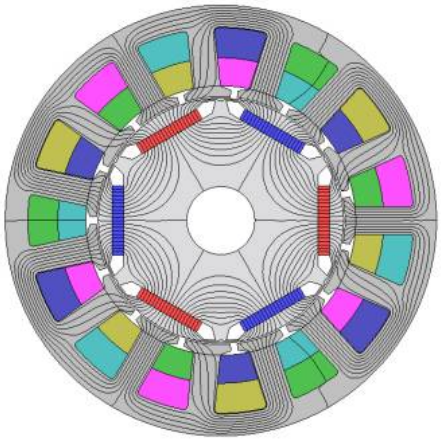

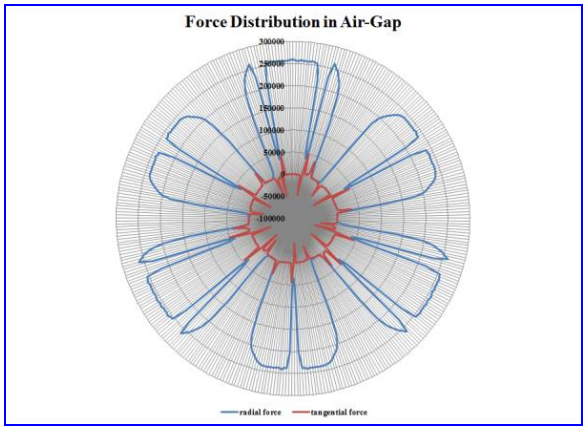

(a) **(b)**

Fig. 43. 15 slots 6 poles at 0˚. (a) Flux line distribution. (b) Air-gap force distribution in polar axis.

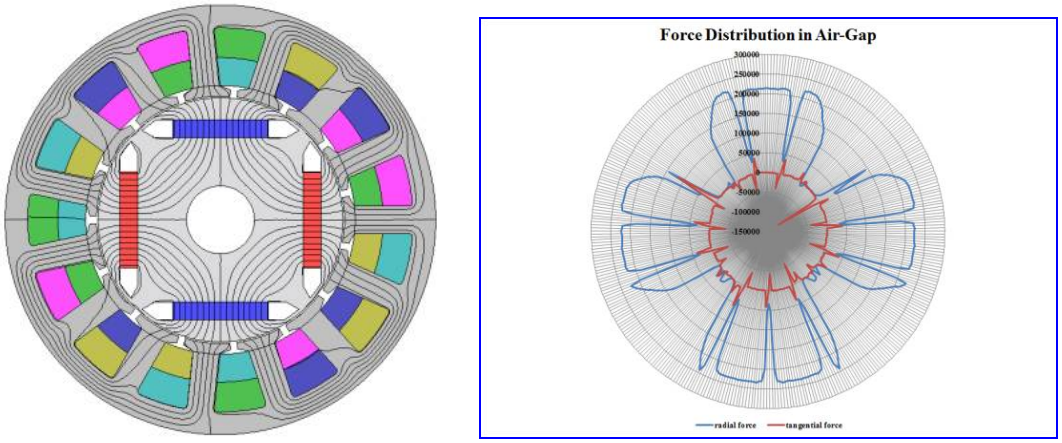

(a) **(b)**

Fig. 44. 15 slots 4 poles at 0°. (a) Flux line distribution. (b) Air-gap force distribution in polar axis.

Air-gap flux density changes depending on the rotor type and effects the air-gap force distribution too. There are mainly three types of rotors in interior PMSM design: single layer, V-shape, and double layer. Each has specific design parameters shown in Fig. 45, Fig. 46, and Fig. 47.

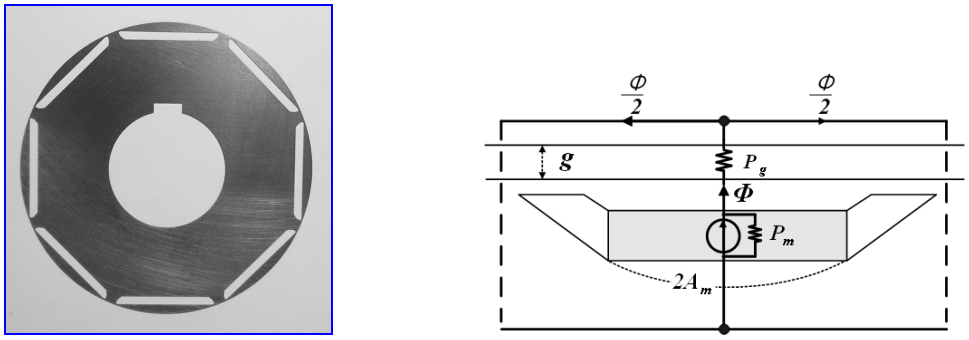

(a) **(b)**

Fig. 45. Single layer. (a) Rotor shape. (b) Design parameters.

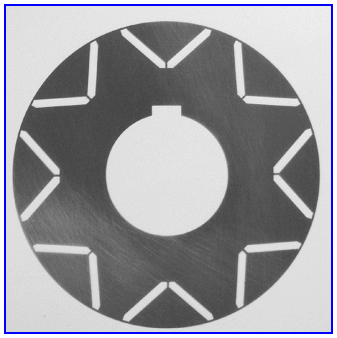

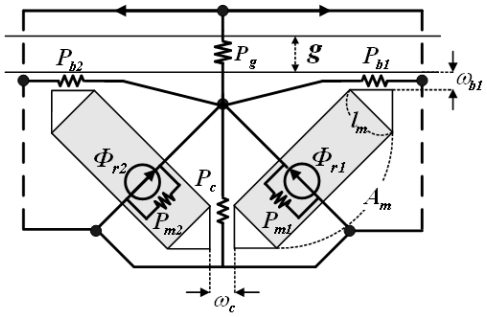

(a) **(b)**

Fig. 46. V-shape. (a) Rotor shape. (b) Design parameters.

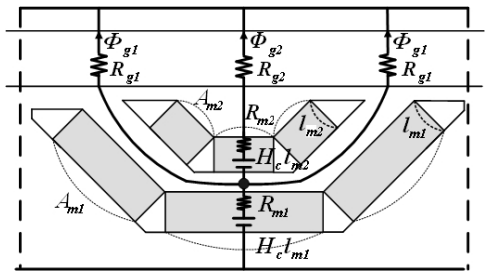

(a) **(b)**

Fig. 47. Double layer. (a) Rotor shape. (b) Design parameters.

The force distributions for the different rotor types are simulated and compared in the polar axis. They are all balanced and relatively distributed as illustrated in Fig. 48, 49, 50, and 51.

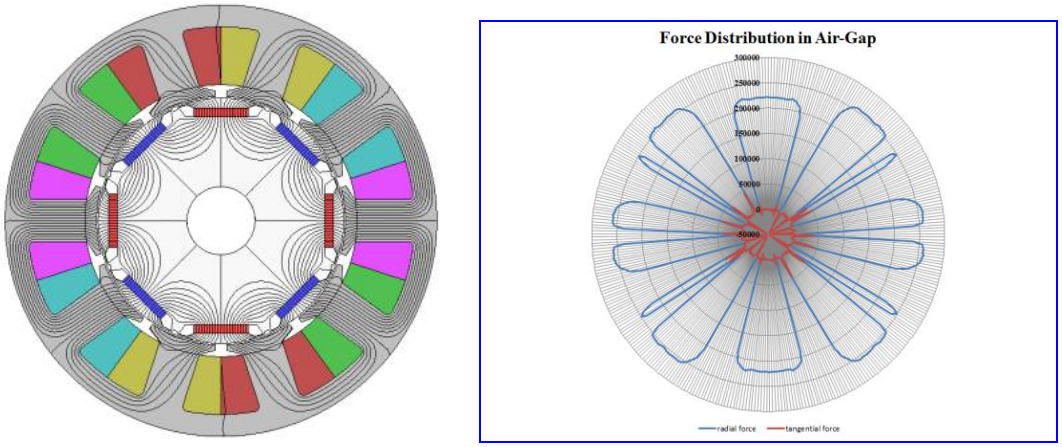

(a) **(b)**

Fig. 48. 10 slots 8 poles at 0˚. (a) Single layer. (b) Air-gap force distribution in polar axis.

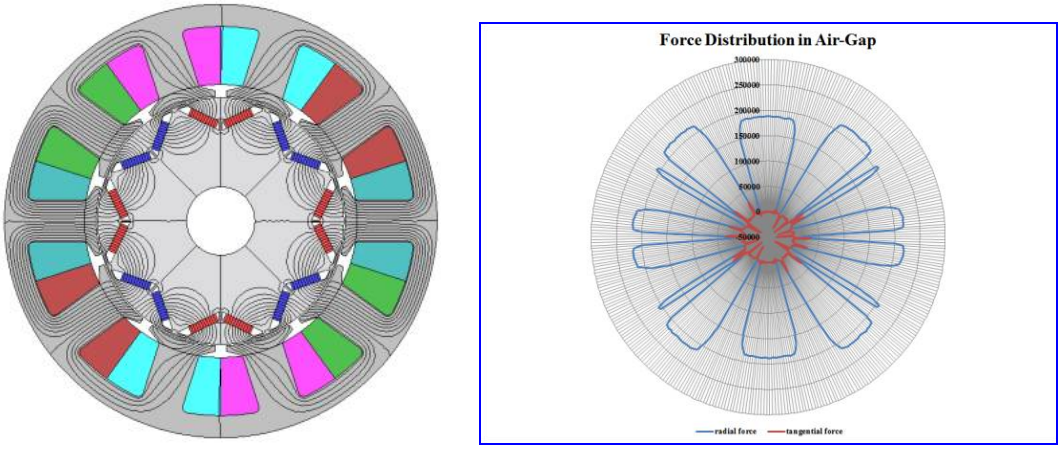

(a) **(b)**

Fig. 49. 10 slots 8 poles at 0˚. (a) V-shape. (b) Air-gap force distribution in polar axis.

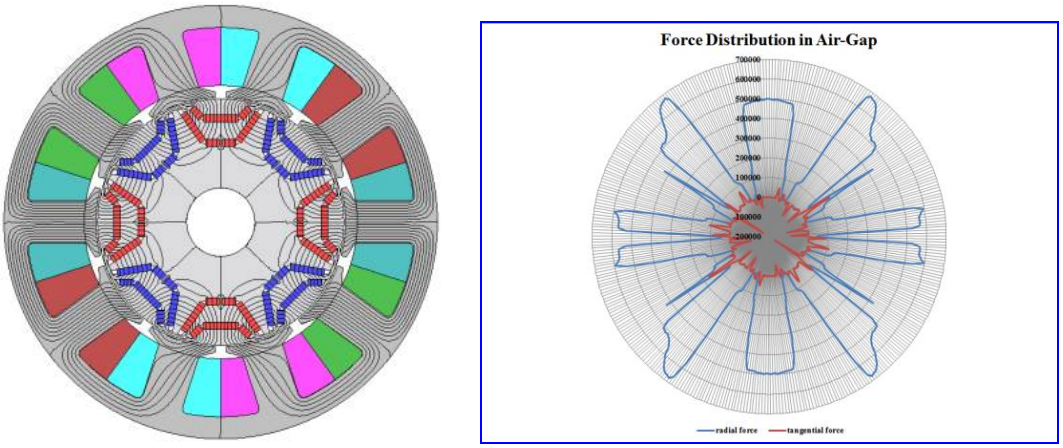

(a) **(b)**

Fig. 50. 10 slots 8 poles at 0°. (a) Double layer M1. (b) Air-gap force distribution in polar axis.

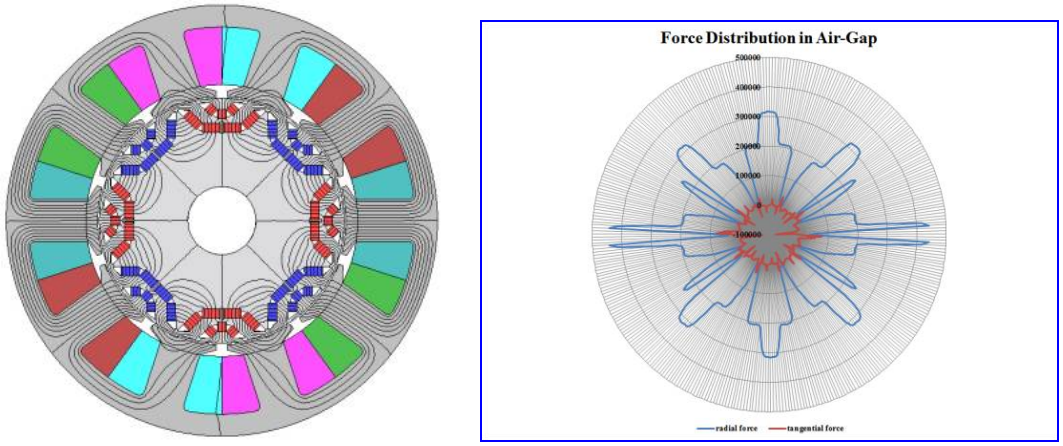

(a) **(b)**

Fig. 51. 10 slots 8 poles at 0°. (a) Double layer M2. (b) Air-gap force distribution in polar axis.

After FFT analysis of the back-EMF, the V-shape rotor type with the 10 slots 8 poles is chosen because the THD is low and the waveform is most closely sinusoidal as compared from Fig. 52 to Fig. 55.

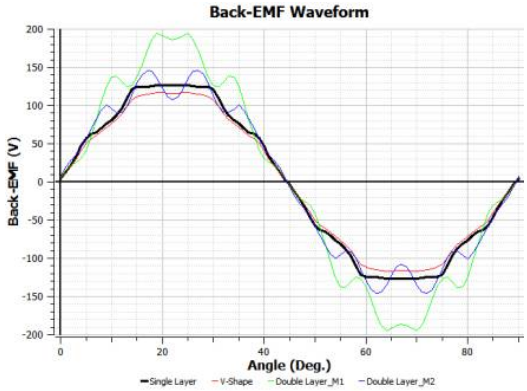

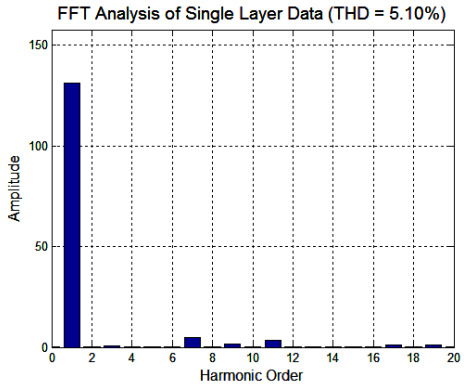

(a) **(b)**

Fig. 52. 10 slots 8 poles & single layer. (a) Back-EMF analysis. (b) FFT analysis.

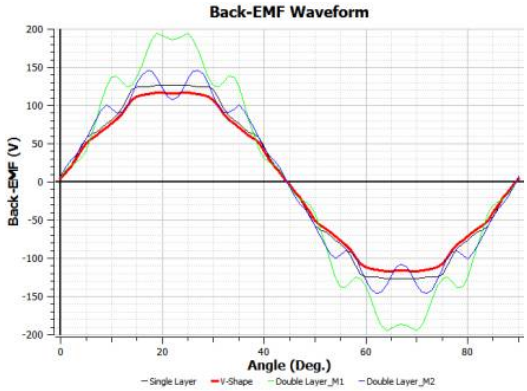

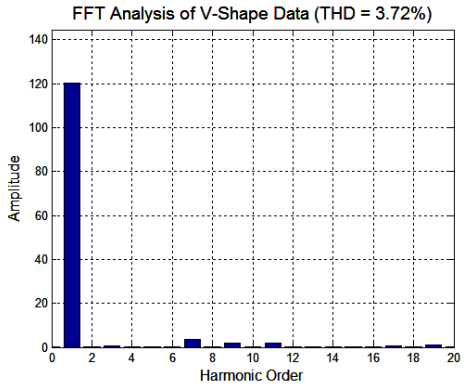

(a) **(b)**

Fig. 53. 10 slots 8 poles & V-shape. (a) Back-EMF analysis. (b) FFT analysis.

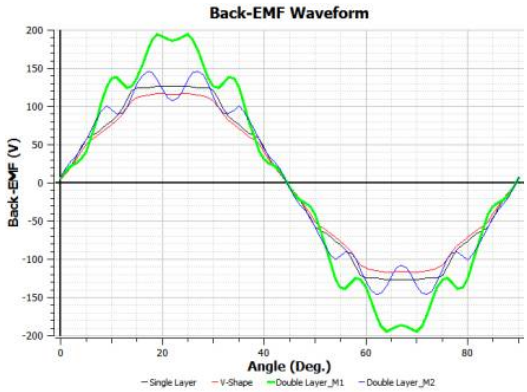

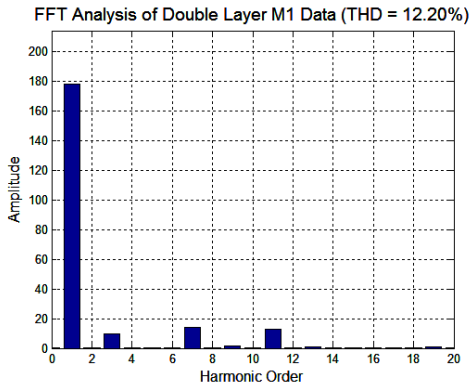

(a) **(b)**

Fig. 54. 10 slots 8 poles & double layer M1. (a) Back-EMF analysis. (b) FFT analysis.

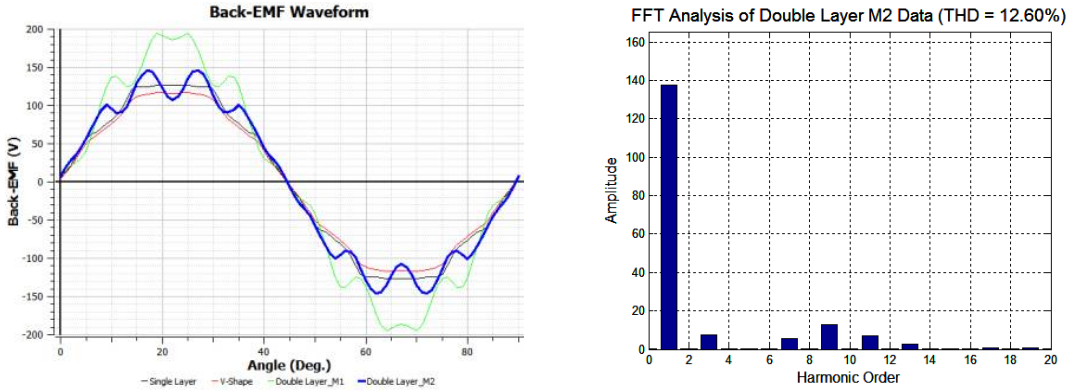

(a) **(b)**

Fig. 55. 10 slots 8 poles & double layer M2. (a) Back-EMF analysis. (b) FFT analysis.

3.4. Stator core design

There are mainly three design constraints when deciding the stator core dimensions. The first one is the stator outer diameter or inner diameter. The second one is the slot area, and the last one is the saturation flux density in a tooth. The outer or inner diameters can decide the slot tooth and slot area dimensions. The slot area is the thermal constraint which can find the current density and slot fill factor. The saturation flux density is the condition which can protect the magnetic flux path in the teeth. With the given design parameters, the stator core dimensions can be decided as shown in Fig. 56.

Stator slot area can be calculated with the number of the coil in the slot, the cross section area of the coil, and slot fill factor [63].

$$A_{slot} = \frac{Z_{slot} A_z}{K_{sf}} = \frac{2mN_{ph} I_a}{K_{sf} Q J_\sigma} \tag{57}$$

where

Z_{slot}: No. of coils in a slot
A_z: Cross section of coil
K_{sf}: Slot fill factor
m: No. of phase
N_{ph}: No. of series turn per phase
I_a: Phase current
Q: No. of slot
J_σ: Current density

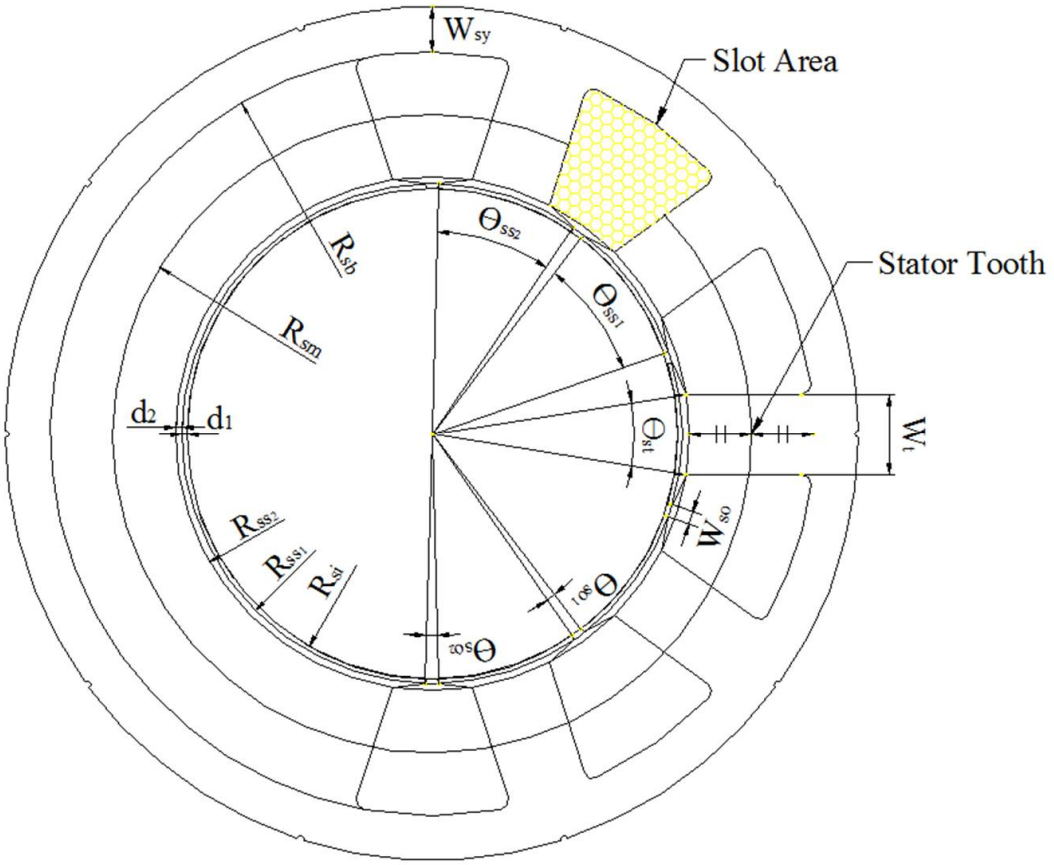

Fig. 56. Stator design parameters.

To calculate the stator slot dimensions, the tooth width needs to be decided. When assuming the saturation flux density in the tooth is B_{tm},

$$N_{sm} B_{tm} W_{tb} L_{stk} = \phi_g \tag{58}$$

where

N_{sm}: No. of slot per pole (=$Q/2p$)

$$W_{tb} = \frac{\phi_g}{N_{sm} B_{tm} L_{stk}} = \frac{2p\phi_g}{Q B_{tm} L_{stk}} \tag{59}$$

When assuming R_{sm} is the radius to the center of the tooth, slot area can be defined:

$$A_s = 2\alpha_{slot} R_{sm} \theta_s \left(R_{sm} - R_{ss2} \right) \tag{60}$$

where

R_{ss2}: Radius to the upper part of the shoe

θ_s: Slot pitch angle

α_{slot} is defined as:

$$\alpha_{slot} = \frac{R_{sm}\theta_s - W_t}{R_{sm}\theta_s} \tag{61}$$

α_{slot} is the main value which decides the tooth width. It is usually between 0.5 and 0.7. From the slot area equation, R_{sm} can be calculated as:

$$R_{sm} = \frac{2\alpha_{slot}\theta_s R_{ss2} + \sqrt{\left(2\alpha_{slot}\theta_s R_{ss2}\right)^2 + 8\alpha_{slot}\theta_s A_s}}{4\alpha_{slot}\theta_s} \tag{62}$$

All values can be found except R_{ss2}. R_{ss2} is equal to the rotor radius plus the shoes depth. The shoe depth is normally 10~20% compared to the tooth length. That is:

$$d_1 + d_2 = \alpha_{slot} W_{tb} \tag{63}$$

Therefore,

$$R_{ss2} = R_{ro} + d_1 + d_2 \tag{64}$$

From this, R_{sb} can be found as:

$$R_{sb} = R_{ss2} + 2\left(R_{sm} - R_{ss2}\right) = 2R_{sm} - R_{ss2} \tag{65}$$

The last step is the thickness of the stator back-york. The flux from the rotor flows the stator back-york though the teeth and makes a closed loop. Therefore, there should be no saturation in the back-york. The air-gap flux can be calculated as:

$$2B_{ym}W_{sy}L_{stk} = \phi_g \tag{66}$$

From the air-gap flux, the back-york thickness can be obtained.

$$W_{sy} = \frac{\phi_g}{2B_{ym}L_{stk}} \quad or \quad W_{sy} = \frac{W_t}{2}\frac{N_{slot}}{N_{pole}} \tag{67}$$

3.5. Rotor core design

V-shape rotor core is widely used and the design factors are well known. Fig. 57 shows the design parameters, θ_m and H_m. The ranges of the parameters are shown in Table 2 based on the mechanical constraints.

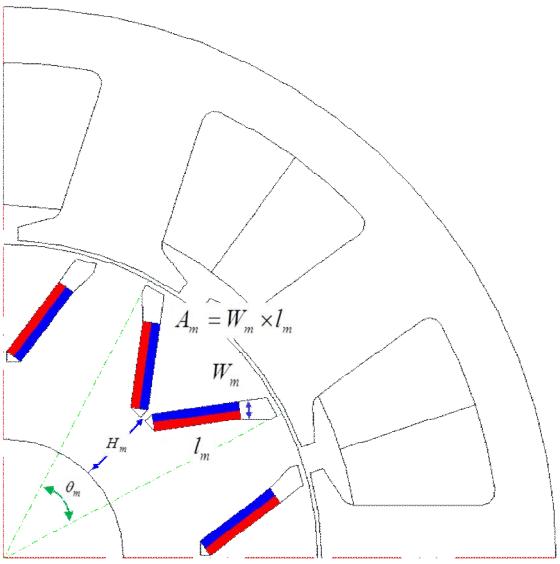

Fig. 57. Stator design parameters.

To optimize the design parameters, response surface methodology is used after the central composite design found the 9 different combinations of the design parameters listed in Fig. 58.

From Fig. 59 to Fig. 61, 9 cases were modeled and simulated to find the objective functions which were listed in Table 3.

Table 2. Design parameter and ranges

Item		Min.	Max.	Unit
1	θ_m	35	40	Deg.
2	H_m	8	12	mm
3	$A_m = 62.4\ [mm^2]$ / pole			

StdOrder	RunOrder	PtType	Blocks	Theta_m	Theta_m / 2	H_m	Case No.
8	1	-1	1	37.50	18.75	17.66	1
11	2	0	1	37.50	18.75	12.00	2
13	3	0	1	37.50	18.75	12.00	2
4	4	1	1	40.00	20.00	16.00	3
12	5	0	1	37.50	18.75	12.00	2
9	6	0	1	37.50	18.75	12.00	2
3	7	1	1	35.00	17.50	16.00	4
2	8	1	1	40.00	20.00	8.00	5
5	9	-1	1	33.96	16.98	12.00	6
1	10	1	1	35.00	17.50	8.00	7
6	11	-1	1	41.04	20.52	12.00	8
10	12	0	1	37.50	18.75	12.00	2
7	13	-1	1	37.50	18.75	6.34	9

Fig. 58. Experimental points from CCD (9 cases).

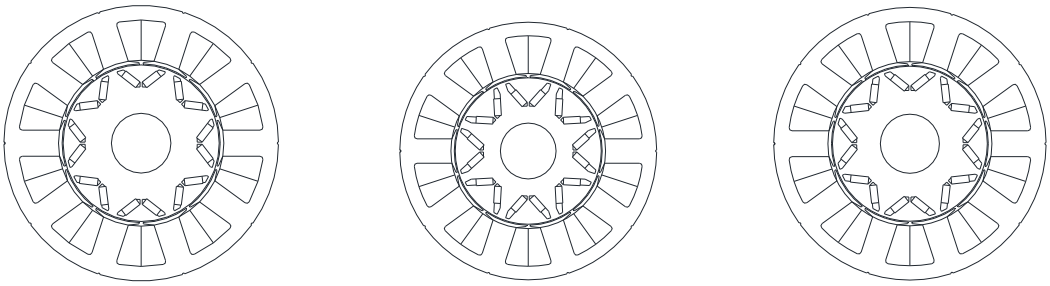

(a) **(b)** **(c)**

Fig. 59. Rotor design cases. (a) Case 1. (b) Case 2. (c) Case 3.

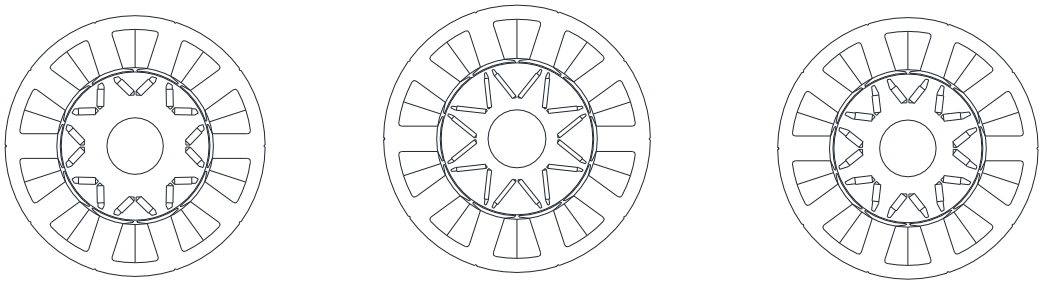

(a) **(b)** **(c)**

Fig. 60. Rotor design cases. (a) Case 4. (b) Case 5. (c) Case 6.

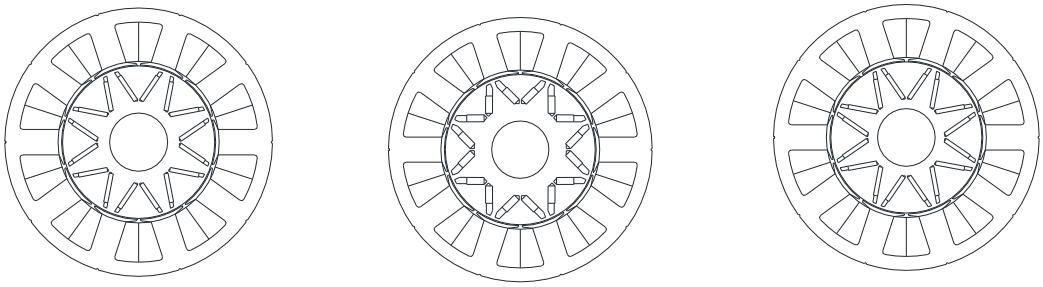

(a) **(b)** **(c)**

Fig. 61. Rotor design cases. (a) Case 7. (b) Case 8. (c) Case 9.

Table 3. Simulation results of each objective function

	Back-EMF THD [%]	Max. Cogging Torque [Nm]	Avg. Torque [Nm]	Efficiency [%]	Torque Ripple [%]
Case 1	43.27	0.076	7.90	92.99	8.68
Case 2	10.37	0.340	7.36	93.60	20.80
Case 3	8.94	0.389	7.76	93.71	18.87
Case 4	11.13	0.147	7.70	92.81	10.73
Case 5	7.06	0.577	10.96	92.98	17.28
Case 6	10.52	0.283	6.39	78.72	18.17
Case 7	7.06	0.577	10.96	92.98	17.28
Case 8	11.69	0.217	7.33	94.03	14.26
Case 9	7.41	0.514	10.80	93.84	9.19

The conjugate gradients method (CGM) was used with the regression coefficients for the response surfaces to decide the optimal design model. The formulation of the regression for each objective function is expressed as follows.

Subject to:

Maximize:

$$Efficiency = -561.838 + 34.221 \times \theta_m - 1.301 \times H_m - 0.441 \times {\theta_m}^2 + 0.048 \times {H_m}^2 + 0.003 \times \theta_m H_m$$

$$Avg.Torque = 34.260 - 0.589 \times \theta_m - 2.506 \times H_m + 0.008 \times {\theta_m}^2 + 0.081 \times {H_m}^2 + 0.007 \times \theta_m H_m$$

Minimize:

$$Back - EMF\ THD = -447.054 + 24.521 \times \theta_m - 2.305 \times H_m - 0.31 \times {\theta_m}^2 + 0.324 \times {H_m}^2 - 0.1 \times \theta_m H_m$$

$$Max.Cogging\ Tor. = 2.346 - 0.108 \times \theta_m - 0.021 \times H_m + 0.002 \times \theta_m{}^2 + 0.002 \times H_m{}^2 - 0.002 \times \theta_m H_m$$

$$Torque\ Ripple = -262.948 + 16.096 \times \theta_m - 2.834 \times H_m - 0.261 \times \theta_m{}^2 - 0.329 \times H_m{}^2 + 0.284 \times \theta_m H_m$$

Constraints:

Efficiency ≥ 90 [%]

Avg. Torque ≥ 7.96 [Nm]

Total A_m = 32448 [mm^3]

Copper = 60 turns / Phase

The objective function equations were derived from the response surface analysis in Minitab, and the constraint conditions of the rotor parameter are based on manufacturing capabilities. The torque was required to be greater than 7.9Nm because the output of the motor is 3kW at 3,600 rpm. Since the efficiency and output torque are the important objective function, these two have a heavier weighting and importance than the other functions. Fig. 62 shows the overlaid contour plots in which the white areas indicate the feasible design regions where all of the objective functions overlap at each factor setting. In the feasible design regions, there are many potential combinations of the design parameters. The solid lines are the minimum values of the objective functions. The response optimizer is a function that finds an optimal point after adjusting the weight and importance values as illustrated in Fig. 62. The optimizer indicates that the optimal point is located where θ_m and H_m are 39° and 8mm respectively based on the given multi-objective functions and constraint conditions. At the optimal setting, the

feasible design region is obtained and the optimum point is marked on Fig. 63. The average torque is approximately 10Nm, the corresponding efficiency is 95.3%, and the maximum cogging torque is 0.6Nm.

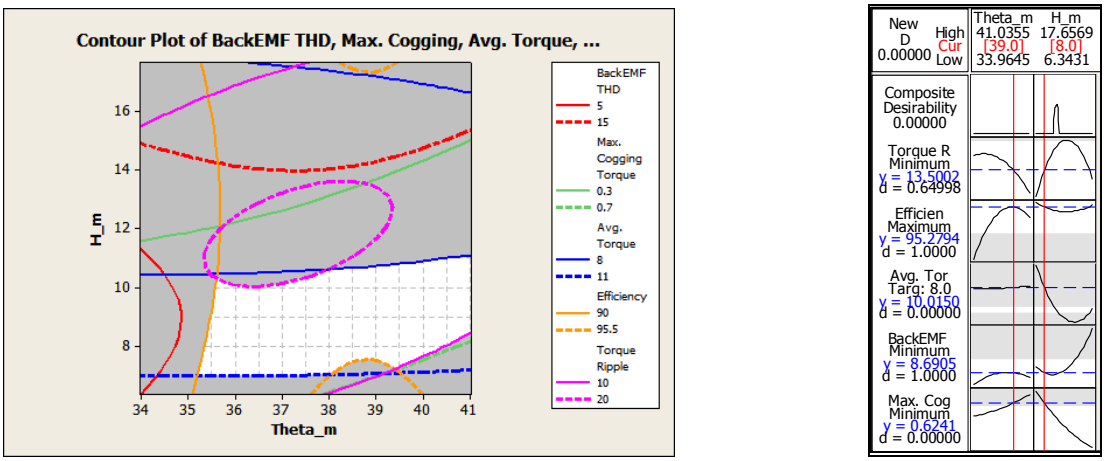

(a) **(b)**

Fig. 62. Optimization plots. (a) Feasible design region plot. (b) Response optimizer plot.

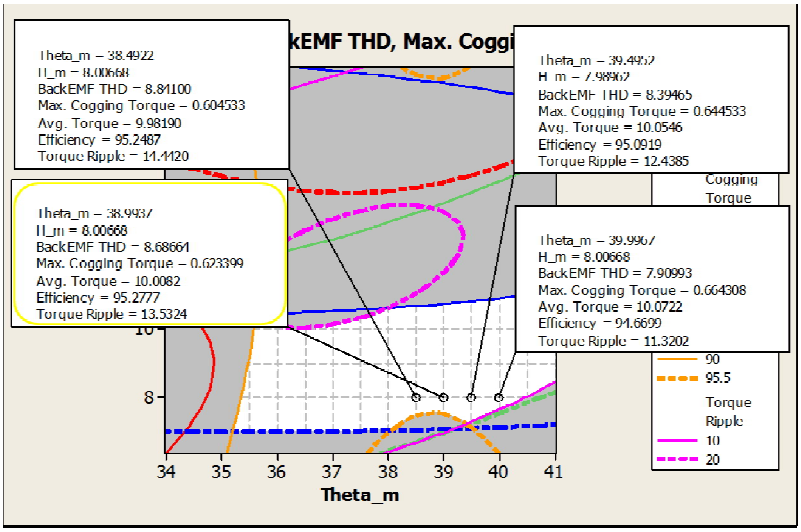

Fig. 63. Optimal point in the feasible design region

Fig. 64 shows the 2D FEA simulation with the optimized design values. Maximum flux density is 2.3T, back-EMF has 10.56% THD in Fig. 65, and the average torque is 8.22Nm with 93.8% efficiency which are exceptional in Fig. 66.

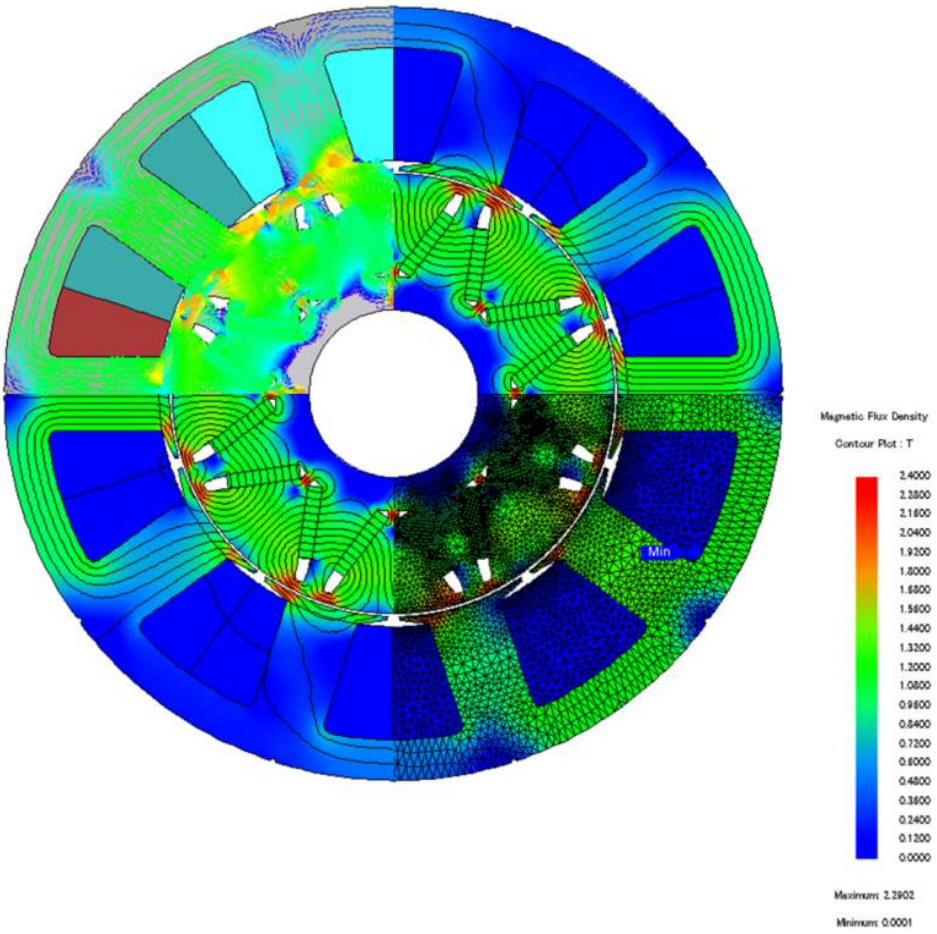

Fig. 64. Optimal point in the feasible design region

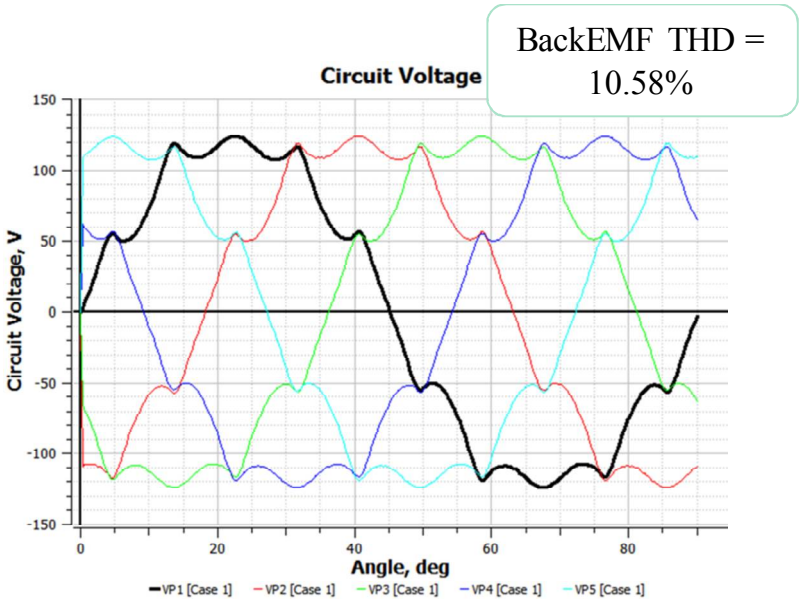

Fig. 65. Optimal point in the feasible design region

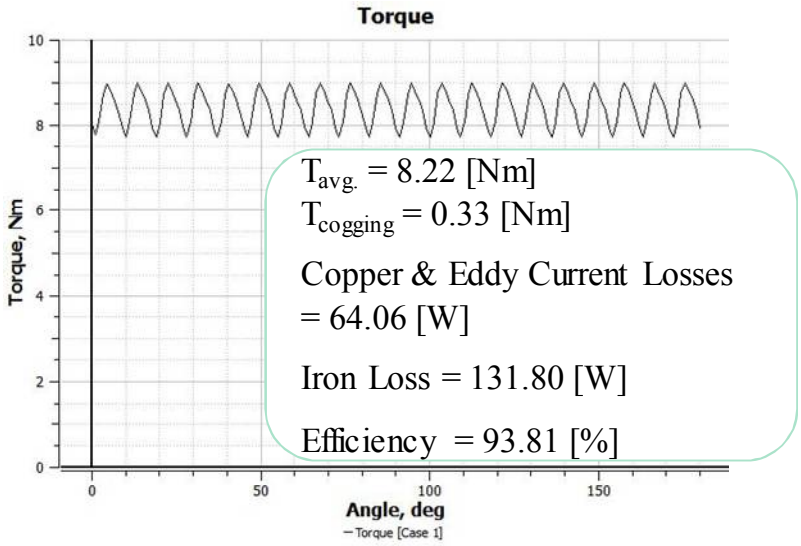

Fig. 66. Optimal point in the feasible design region

3.6. Design results

This section shows the design drawings for 5-phase 10-lead Interior PMSM.

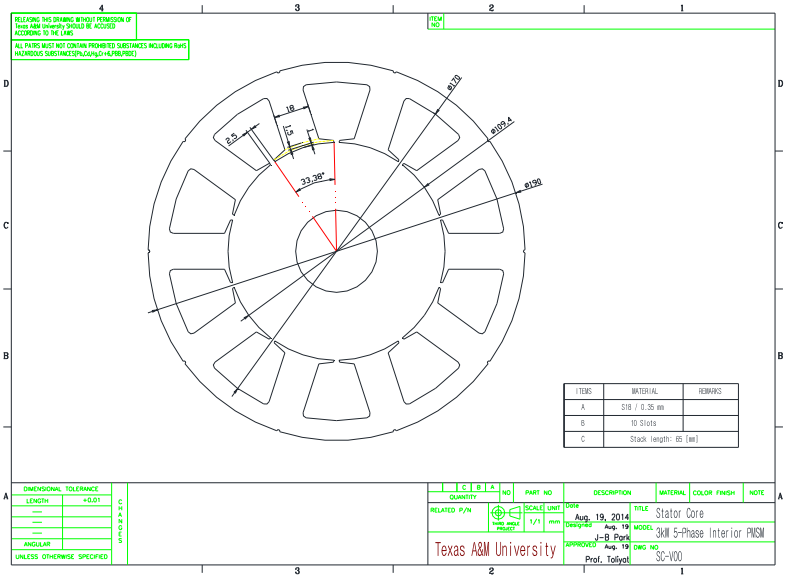

Fig. 67. Stator core design drawing

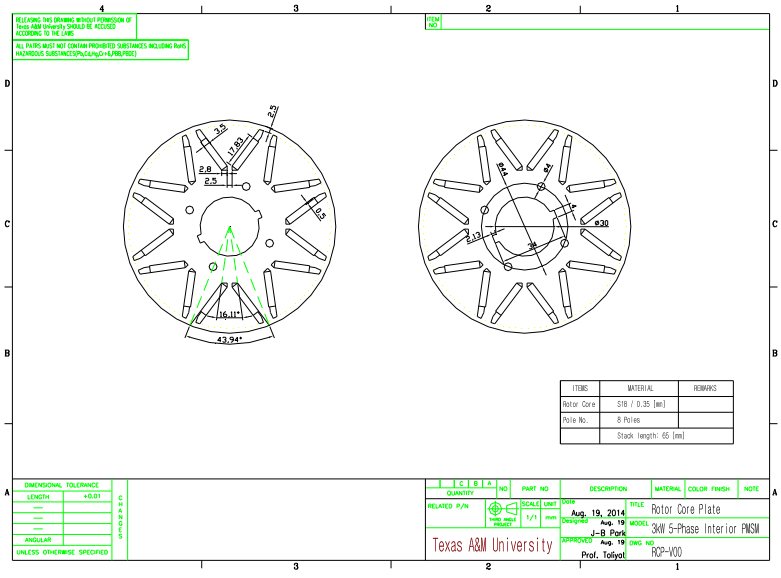

Fig. 68. Rotor core design drawing

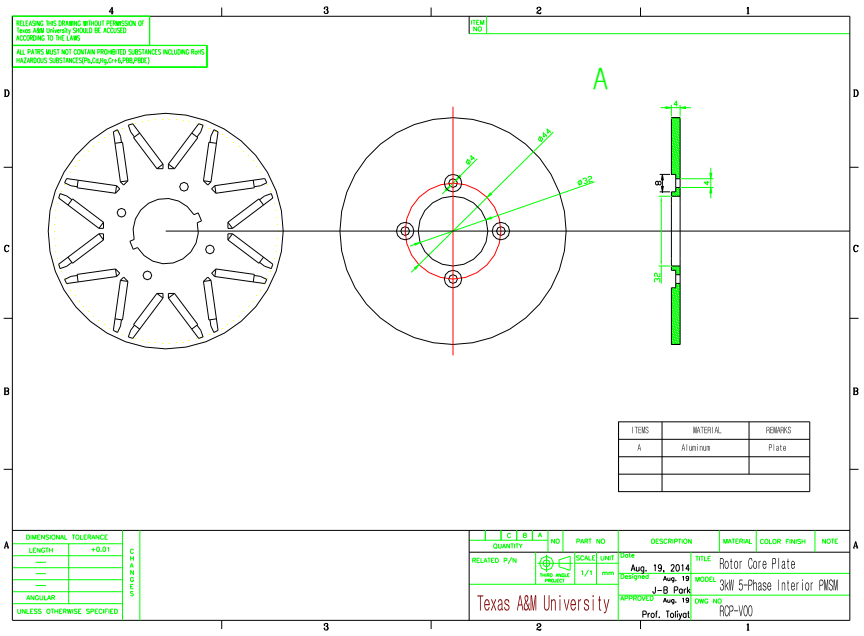

Fig. 69. Rotor core plate design drawing

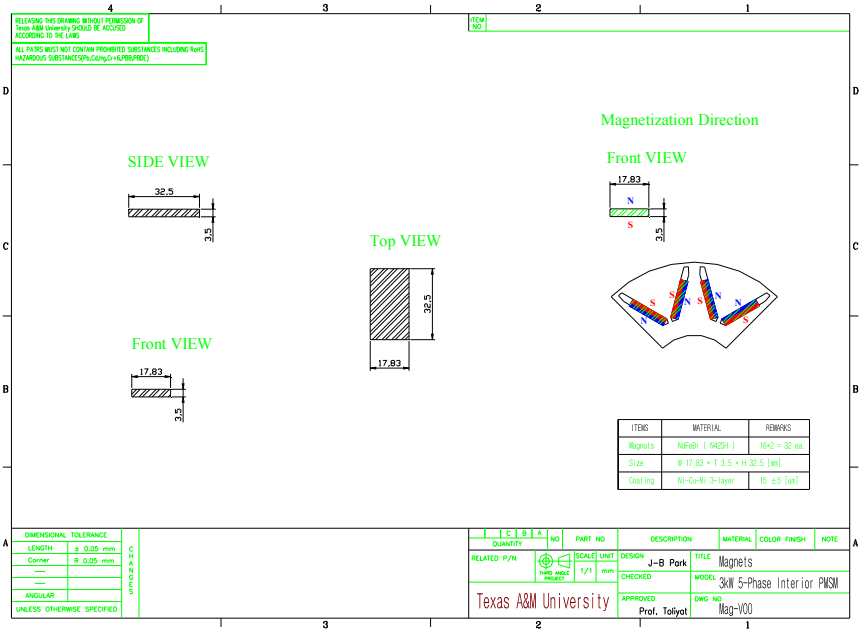

Fig. 70 . Magnet design drawing

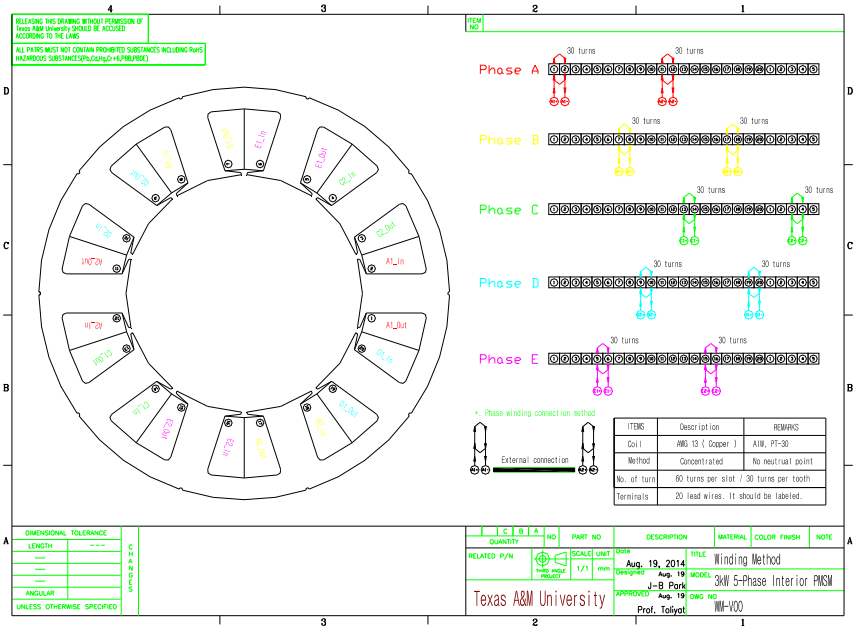

Fig. 71. Winding design drawing

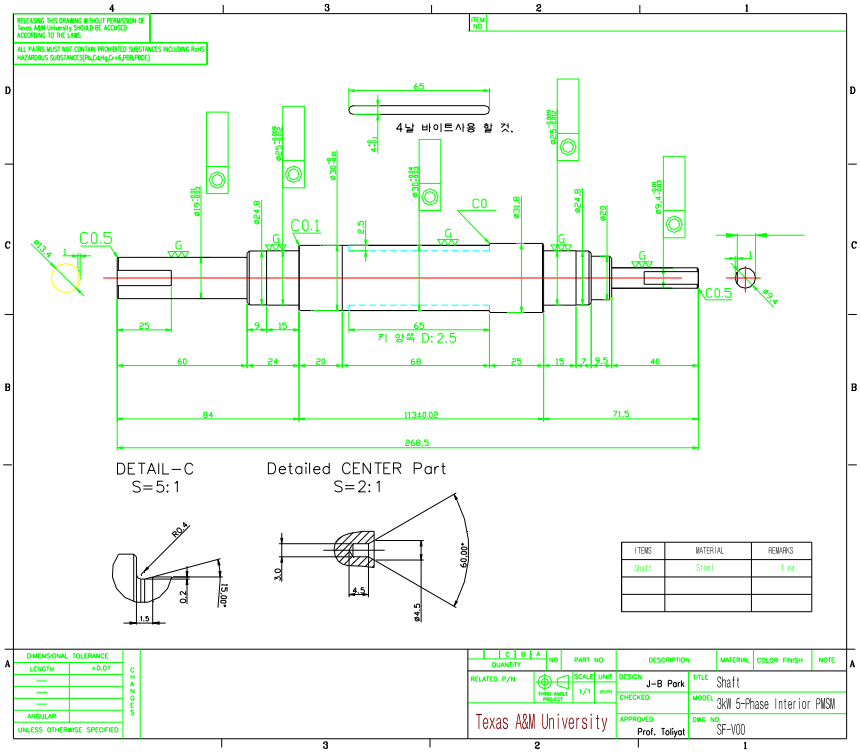

Fig. 72. Shaft design drawing

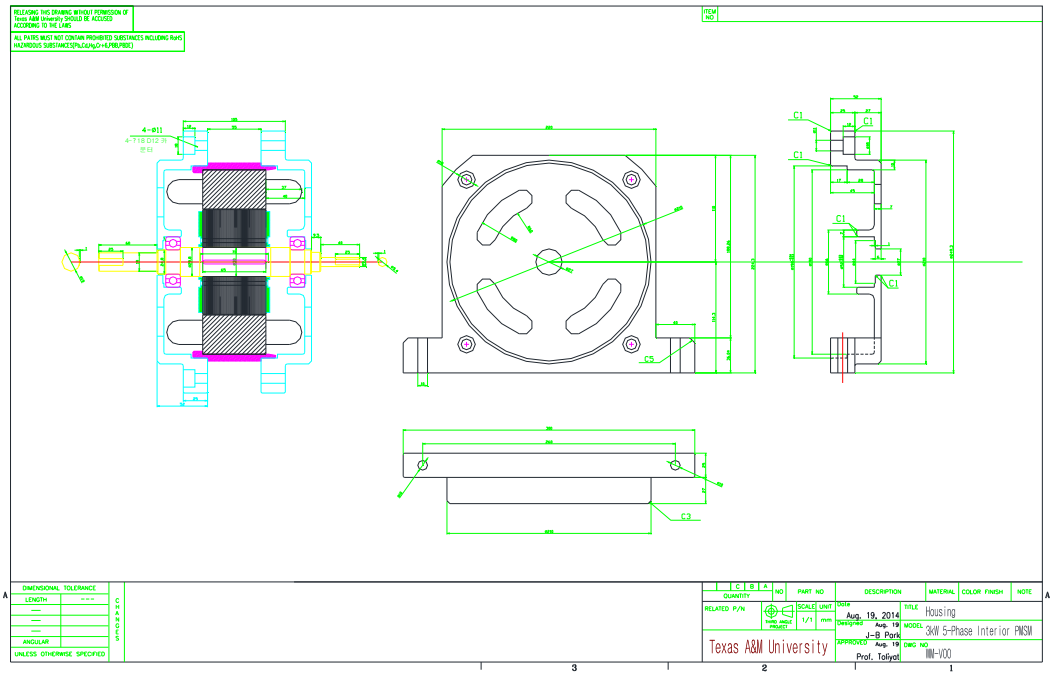

Fig. 73. Housing design drawing

After the optimization, each dimension was evaluated by FEA and resized based on the flux saturation in the magnetic path from Fig. 67 to Fig. 73. Fig. 67 shows the stator core design which has 18mm tooth width and 2.5mm slot opening. Rotor core was optimized with Response Surface Method in Fig. 68, and the core plate is designed to cover the magnets in the rotor core in Fig. 69. Fig. 70 shows the magnet dimension with the magnetization information, and the winding method without neutral point is shown in Fig. 71. Shaft and housing design drawings are illustrated in Fig. 72 and Fig. 73.

3.7. Modifying the existing 5-phase interior PMSM

The existing 5-phase interior PMSM was modified. After removing the neutral point shown in Fig. 74, each phase became independent with 10 leads instead of having 5 leads and one neural point inside of the motor. Fig. 75 shows each part of the motor, and the stator has two sets of the terminal which has 10 leads.

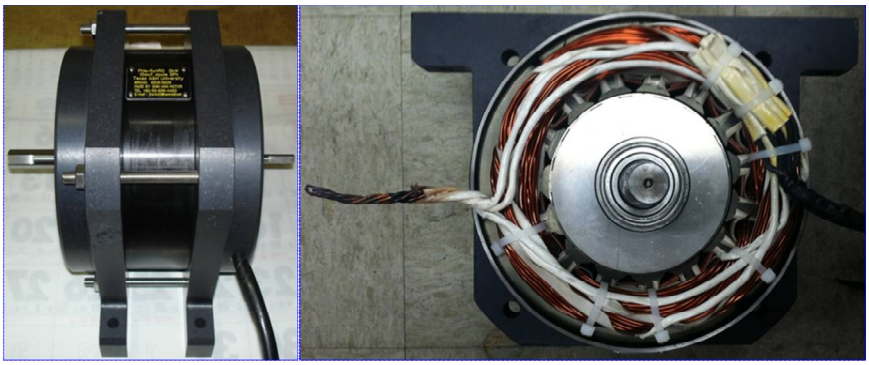

Fig. 74. 5-phase interior PMSM with neutral point.

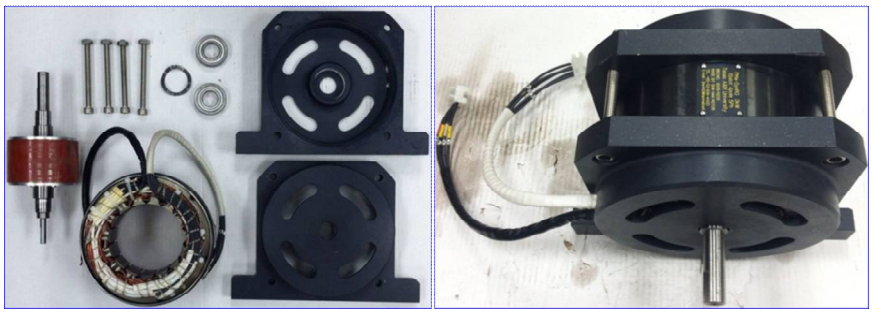

Fig. 75. Modified 5-phase 10-lead interior PMSM.

Winding method is shown in Fig. 76. The motor has distributed winding method with 3 coil spans, and the magnets are inserted in the second layer of the rotor pole in Fig. 76. The winding factor of the motor is 0.937, but the distributed winding method based on the stator slot and rotor pole combination makes the air-gap force distribution unbalanced as depicted in Fig. 77. As a result, the motor has a lot of harmonics in the back-EMF. Vibration and noise will be an issue too.

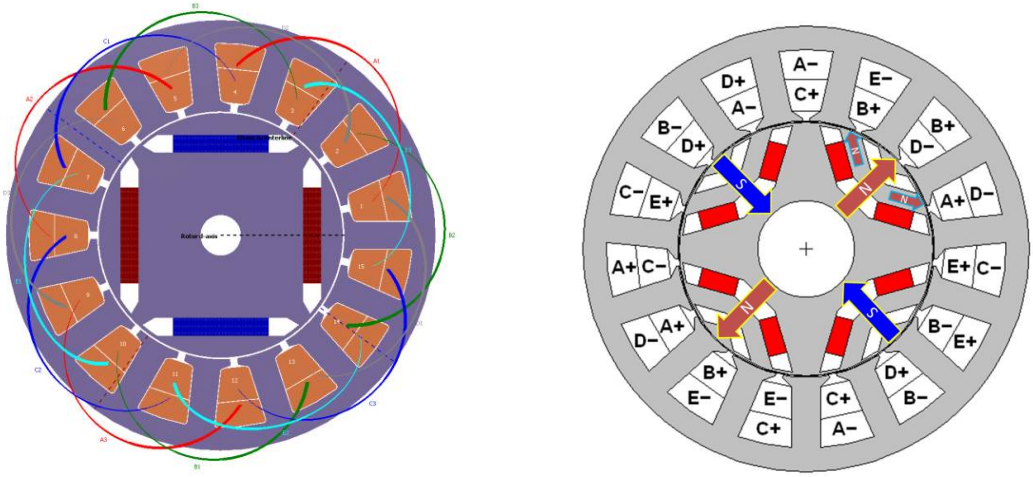

(a) **(b)**

Fig. 76. Existing 5-phase interior PMSM. (a) Distributed winding. (b) Rotor core and magnets.

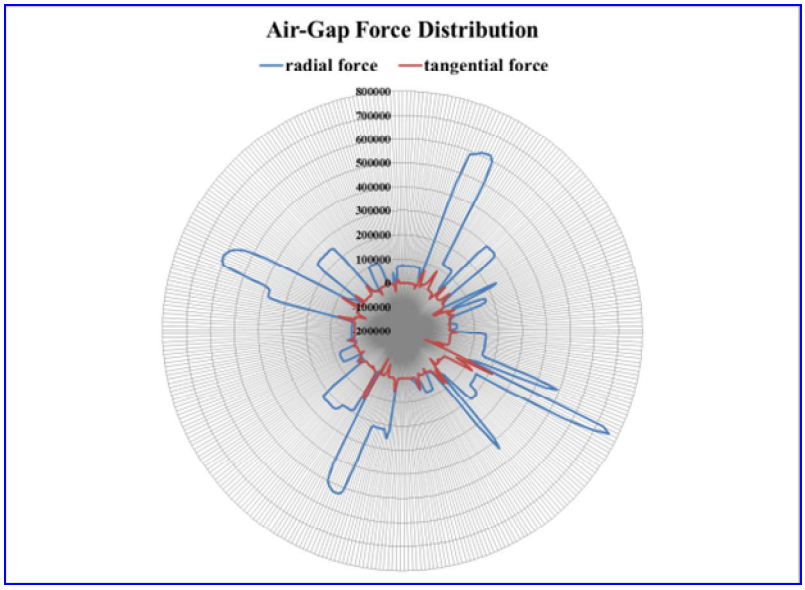

Fig. 77. Air-gap force distribution for 5-phase 10-lead interior PMSM.

To understand the modified interior PMSM, the back-EMF and cogging torque were measured by the test set-up in Fig. 78. The motor is connected to the torque meter and the torque meter has a connection with the 6kW induction motor though the coupling. When testing the PMSM, the secondary motor should not have harmonic component because it affects the main motor's performance. Usually, skewed or slotless induction motors are mainly used. The induction motor has slot harmonic, so it is expected to see them in the waveforms of the interior PMSM.

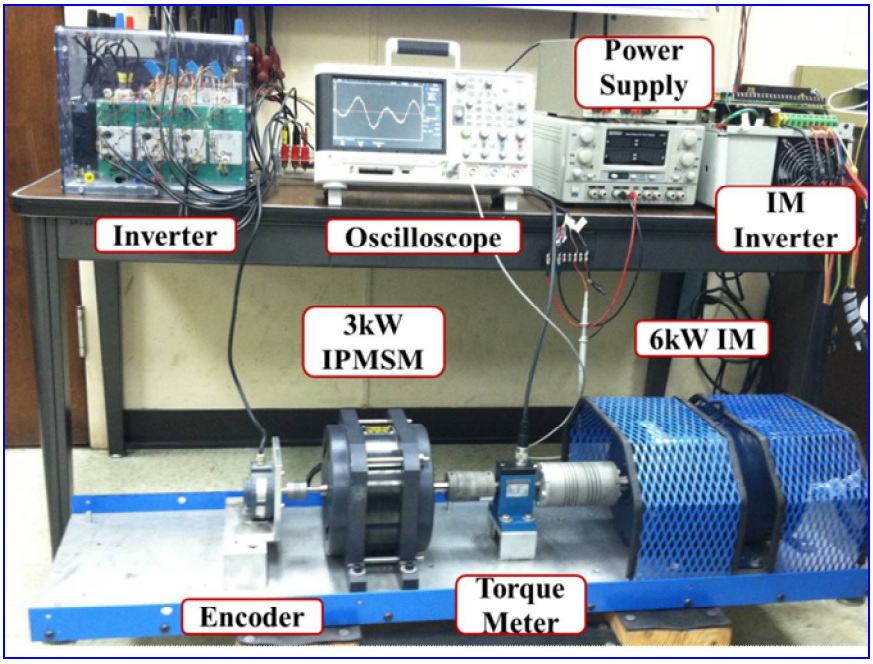

Fig. 78. Back-EMF and cogging torque test set-up.

While controlling the induction motor by V/F, the back-EMF waveforms were measured from the motor terminals. The back-EMF waveforms show 72˚ phase shift and a lot of harmonic components at low speed. Even at high speed, the back-EMF has wired peak waveform because of the magnet position in the rotor core in Fig. 79. It can be expected that the control current will have much harmonic as soon as the motor generates back-EMF even though applying a certain reference value. The current will follow the reference, but the phase current will have harmonic components from the back-EMF.

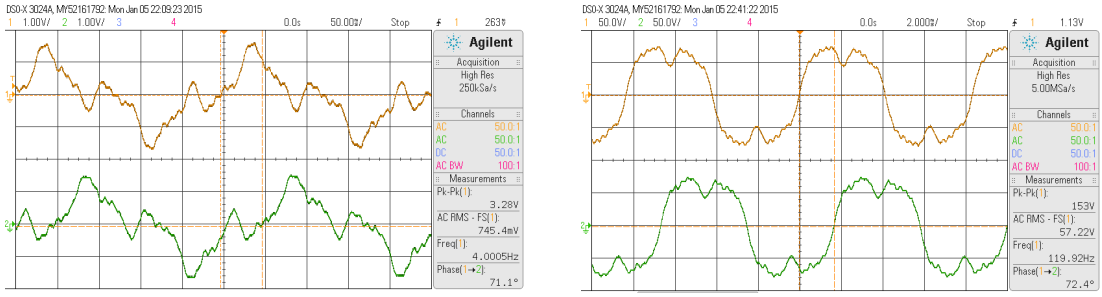

(a) **(b)**

Fig. 79. Back-EMF waveforms. (a) At low speed. (b) At high speed.

Fig. 80 shows the cogging torque waveform which has slot harmonic components from the induction motor as mentioned previously. The maximum cogging torque is 0.63 Nm.

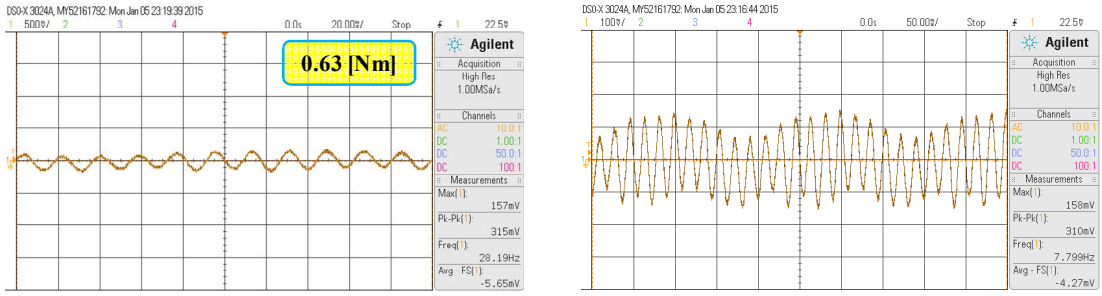

(a) **(b)**

Fig. 80. Cogging torque waveforms. (a) At low scale. (b) At high scale.

3.8. Summary

Aspects of interior PMSM design were investigated in this chapter. Design procedure was proposed and applied. Fractional design method was mentioned to find main design parameters in the process of the screening design. An optimization method

called response surface method was discussed and used in the design. Force distribution analysis was discussed to find a best stator slot and rotor pole combination. Each case were compared and evaluated by FEA. Stator design parameters were defined in detail. Rotor design parameters were optimized by response surface method and FEA. All design drawings are shown in the design results section. An existing 5-phase interior PMSM was modified to check the control methods, and its back-EMF and cogging torque were measured after making a test set-up. It is shown that the existing motor can be used to confirm the control method proposed.

4. 5-PHASE 10-LEAD INTERIOR PMSM INVERTER DESIGN

4.1. Introduction

To control the motor, the commercial Semikron boxes and TI Delfino DSP is used through the newly designed interface board. Fig. 81 shows the block diagram of the control system. After generating control signals from the DSP board with TI's F28335, the interface board regulates the voltage levels for the gate drives, and the gate drives control the 20 IGBTs in 5 H-bridge inverters. Finally the IGBTs power the motor.

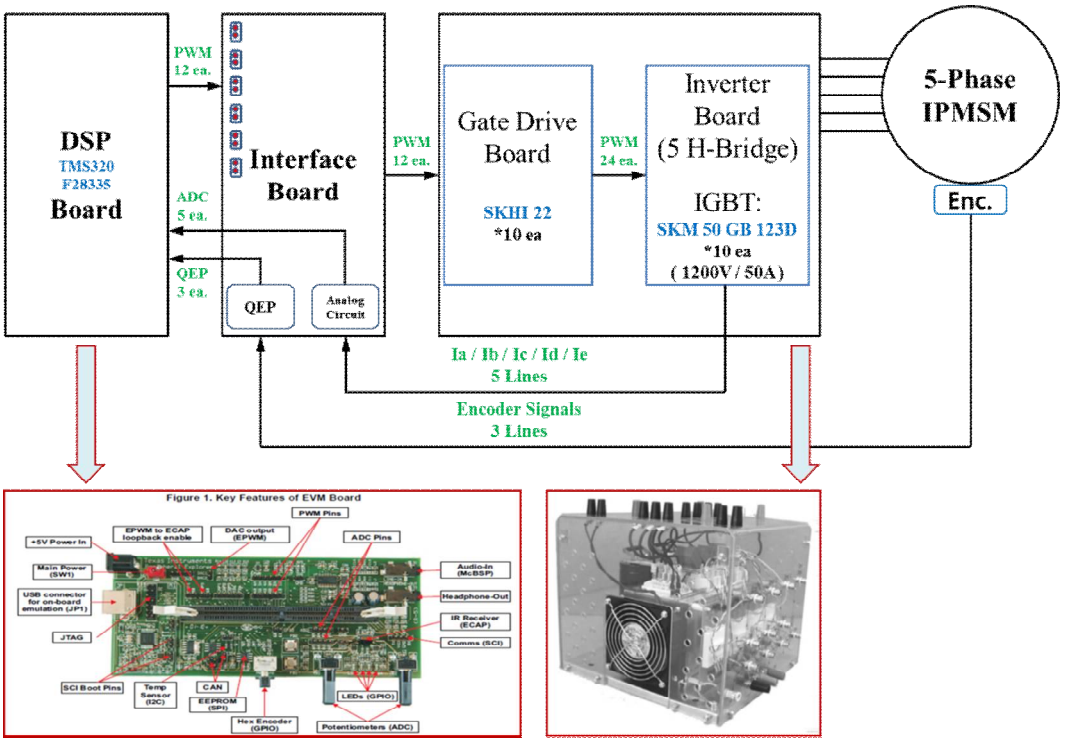

Fig. 81. 5-phase 10-lead interior PMSM invertor block diagram

The interface board has 7 parts: DSP boards connector, a current sensing circuit, a PWM signal circuit, a QEP circuit, a hardware protection circuit, a power supply circuit, and an inverter gate signal connector part. Fig. 82 shows the interface board circuit which has been designed and fabricated.

In the PWM signal circuit, a new gate control signal generation scheme capable of achieving both fixed and variable switching frequency modes was proposed and realized with two PWM signals, two GPIO signals, and four MUXs as shown in Fig. 83.

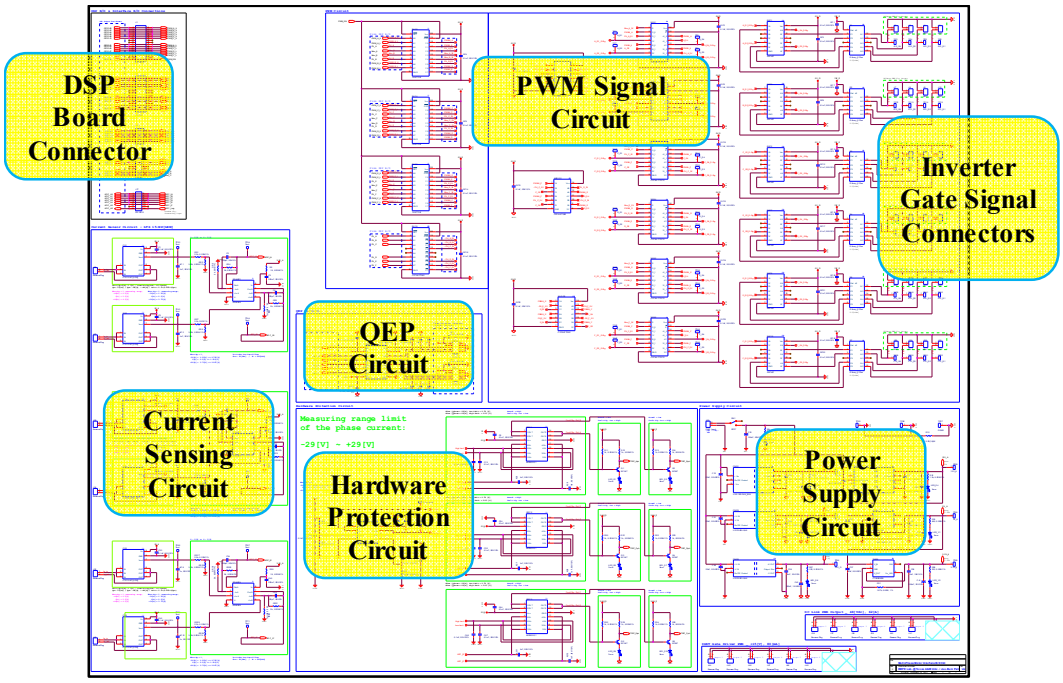

Fig. 82. Interface board circuit.

For the fixed switching frequency mode, two PWM signals will control the gates; whereas in the variable switching frequency mode one GPIO signal and one PWM signal

will control the gates. The active operating is determined by the mode selector which is controlled by one GPIO signal in a programmable manner.

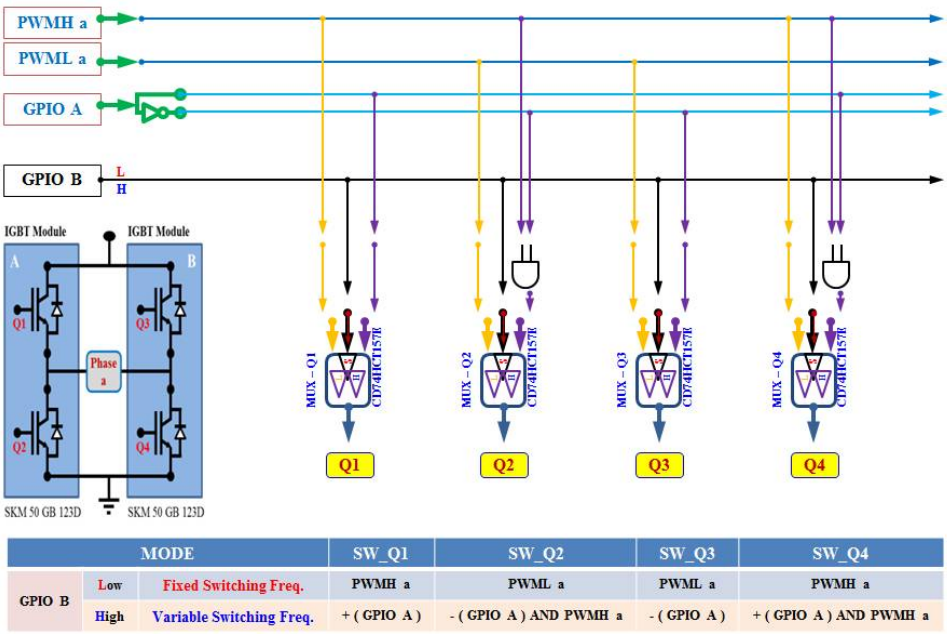

MODE			SW_Q1	SW_Q2	SW_Q3	SW_Q4
GPIO B	Low	Fixed Switching Freq.	PWMH a	PWML a	PWML a	PWMH a
	High	Variable Switching Freq.	+ (GPIO A)	- (GPIO A) AND PWMH a	- (GPIO A)	+ (GPIO A) AND PWMH a

Fig. 83. Concept of gate control signal generation.

On the left in Fig. 84, it is the top and bottom layer of the PCB layout design using Altium Designer v14.

On the right is the combined layer. 15 or 20 Mils are used for the signal line, 30 or 50 Mils are used for the power line, and 350-400 Mils are used for the current sensing line because the maximum current flowing is 30A.

To avoid the signal noise issue, ground line was divided into three sections: DGND indicates digital circuit ground, AGND indicates analog digital ground, and GND indicates the ground except the digital and analog circuit. These three grounds are

connected though a zero resistor which can protect the noise signal circulation one another.

Fig. 85 demonstrates the fabricated interface board without the components and with the components soldered on.

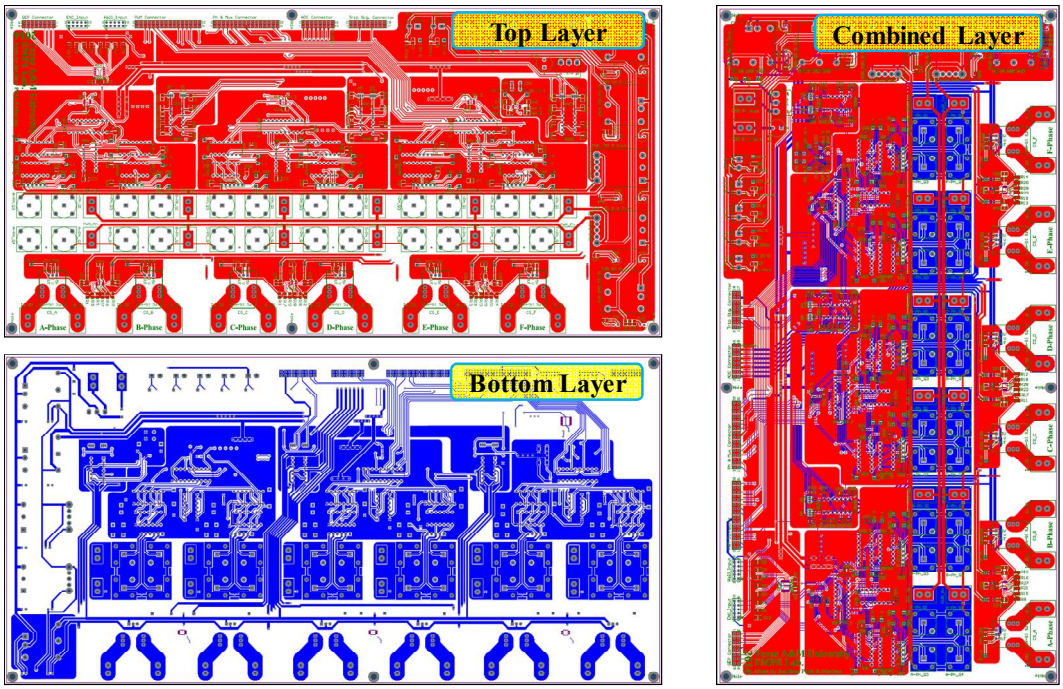

Fig. 84. Interface board PCB layout design.

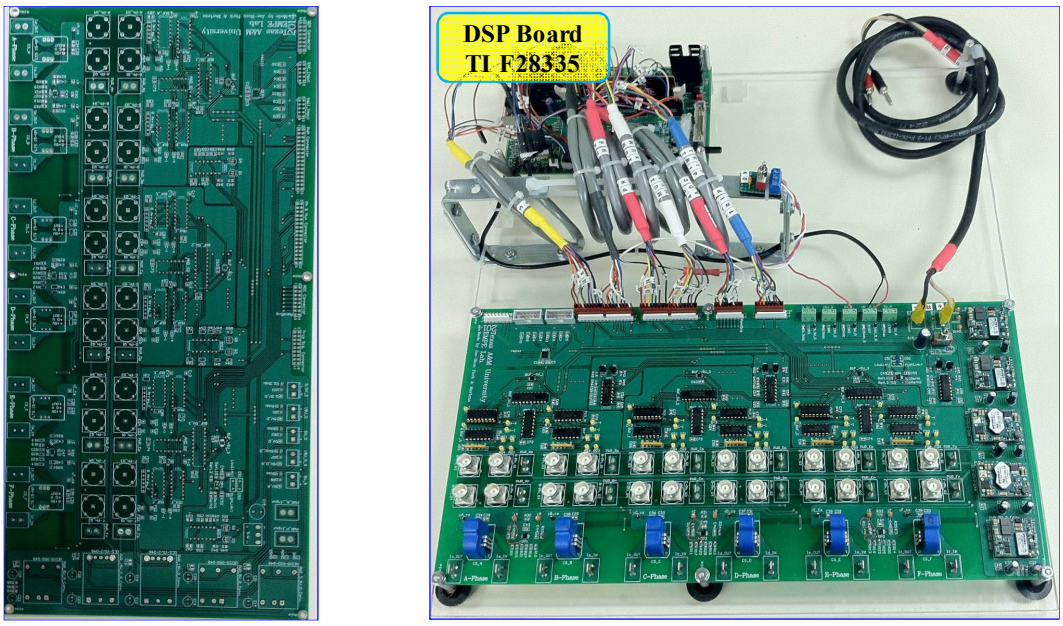

Fig. 85. Fabricated interface board with DSP board.

4.2. Interface board circuits

This section illustrates each circuit drawing from Fig. 86 to Fig. 91. The power supply circuit provides 3.3V, 5V, and 15V for the ICs and gate drives on the board with the 48Vdc input in Fig. 91. The interface board has connectors which access the GPIO or PWM signals from the DSP board, QEP signals from encoder, ADC signals from current or voltage sensor outputs as shown in Fig. 86.

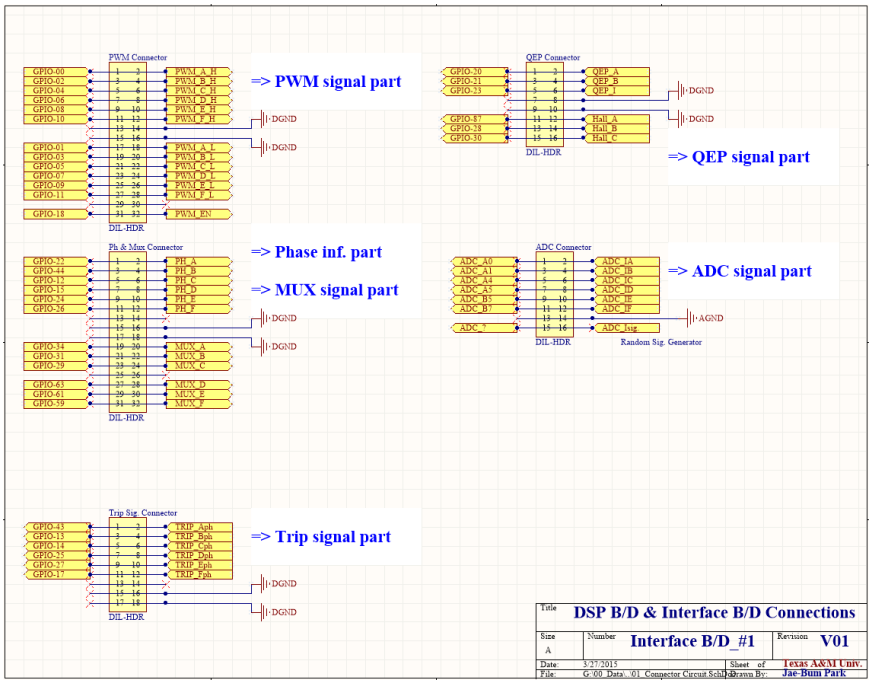

Fig. 86. DSP board connection.

In the current sensing circuit, Fig. 87, LEM's LTS 15-NP current transducers are chosen, and the measuring range is set to ± 30A. 1st order low pass filters are implemented with OPA 2350, and the switching frequency is 20 kHz with 362 kHz cutoff frequency. These values are for general purpose, so users can change the gain after replacing the resister and capacitor values on the board. QEP circuit in Fig. 88 has the voltage level converter that DSP can accept the signal from 5V output of the encoder.

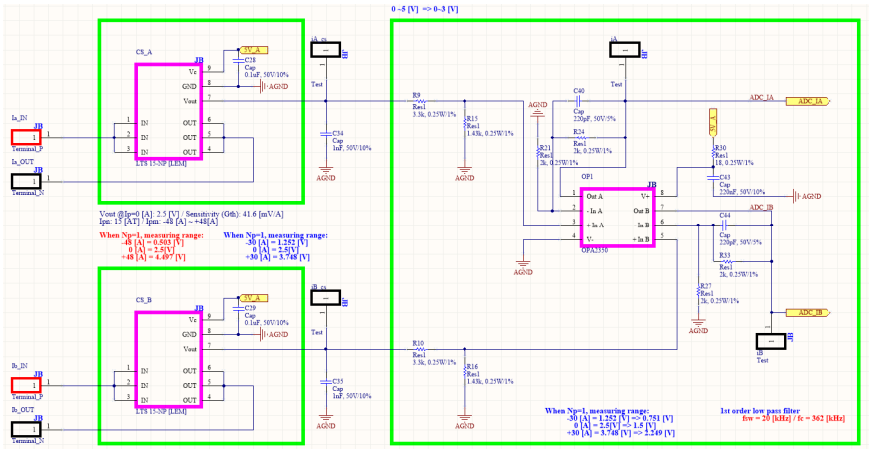

Fig. 87. Current sensing circuit.

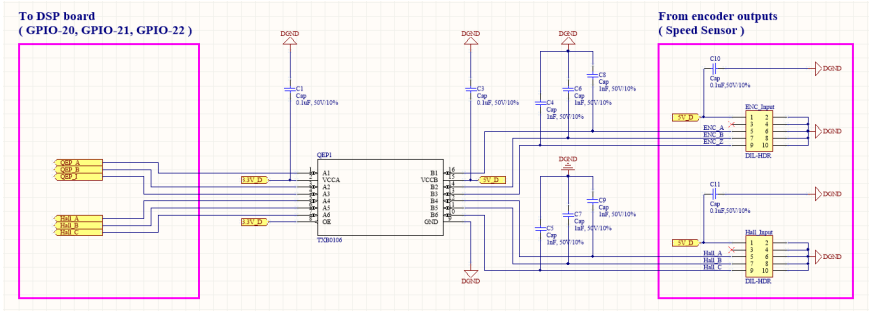

Fig. 88. QEP circuit.

To protect the interface board circuit from the motor phase current, the hardware protection trip signals are sensed from the output of the current sensor and disable the PWM signal as soon as any phase current is over 30A as depicted in Fig. 89. PWM signals and phase signals are generated from the DSP board and control the gate drives though MUXs, AND gates, and inverting buffers in Fig. 90.

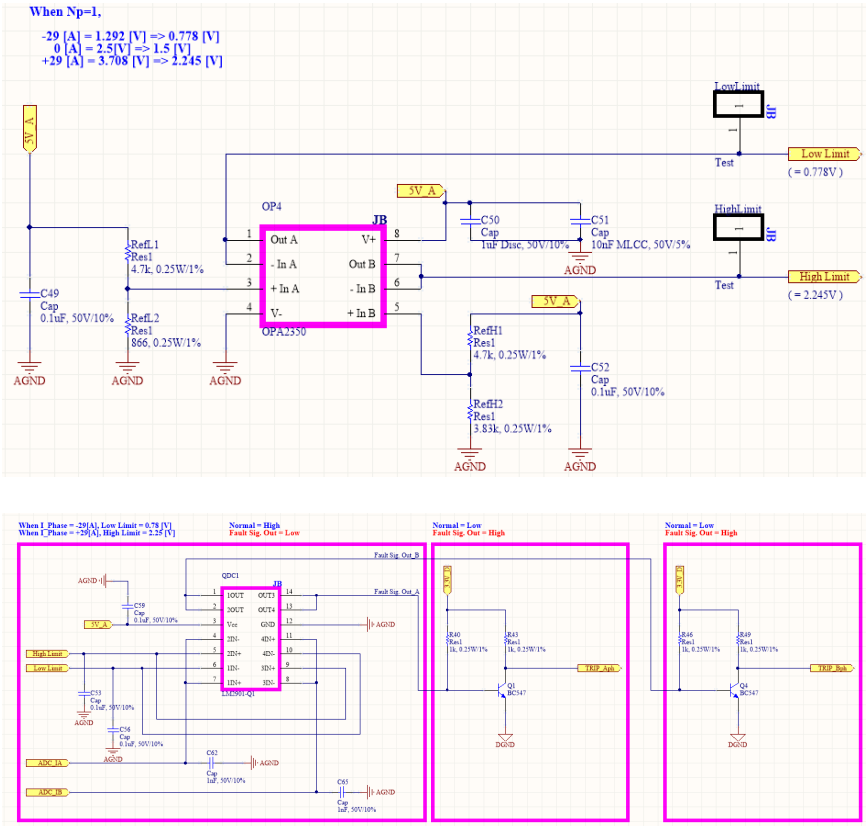

Fig. 89. Hardware protection circuit.

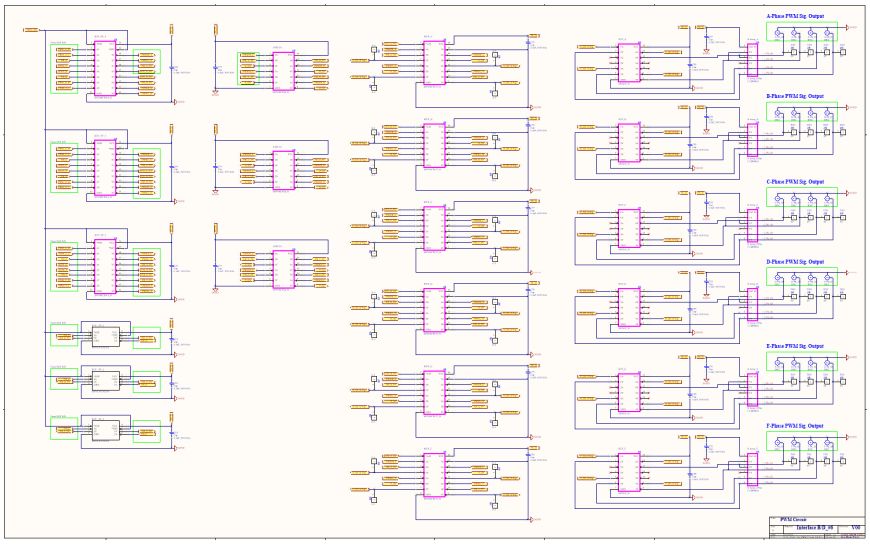

Fig. 90. PWM gate signal circuit.

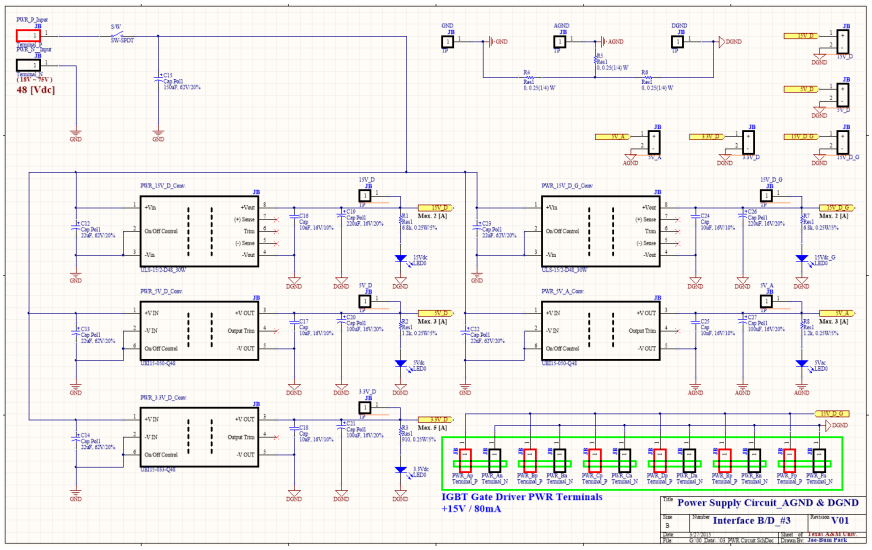

Fig. 91. Power supply circuit.

4.3. Summary

A newly designed invertor system was introduced, and an interface board was designed and fabricated to control the 5-phase 10-lead interior PMSM. Each circuit part is explained in detail and the fabricated interface board without the components and with the components soldered on is shown in this section.

5. 5-PHASE 10-LEAD INTERIOR PMSM CONTROL

5.1. Introduction

This chapter reports on the fabrication of a reconfigurable control set-up, and the results of the experiments performed on the set-up. An effective switching method was proposed and confirmed through various control methods. Moreover, closed loop speed control was implemented using 10-step VSI control, SPWM, and hysteresis control methods [64].

5.2. Reconfigurable motor control set-up

Basic performance of the 5-phase 10-lead interior PMSM was measured with the test set-up as shown in Fig. 92. The 5-phase PMSM is connected to the torque meter and induction motor though the couplings. While controlling the 3-phase induction motor, the basic performance of the 5-phase PMSM can be measured form an oscilloscope.

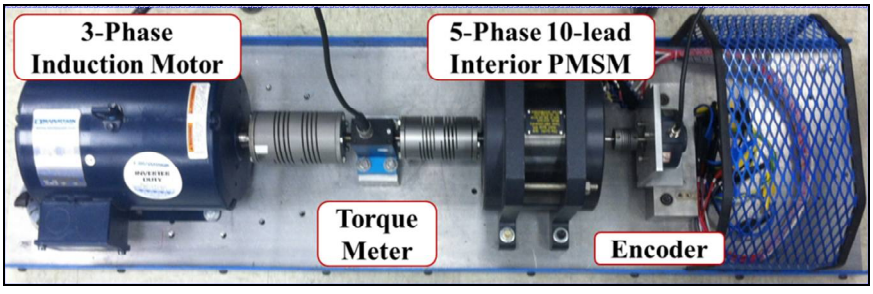

Fig. 92. Back-EMF and cogging torque test set-up connection.

To control the 5-phase PMSM, encoder and 3-phase loading motor were added instead of the induction motor, so the motor can be controlled after detecting the position of the rotor while adding the load in Fig. 93.

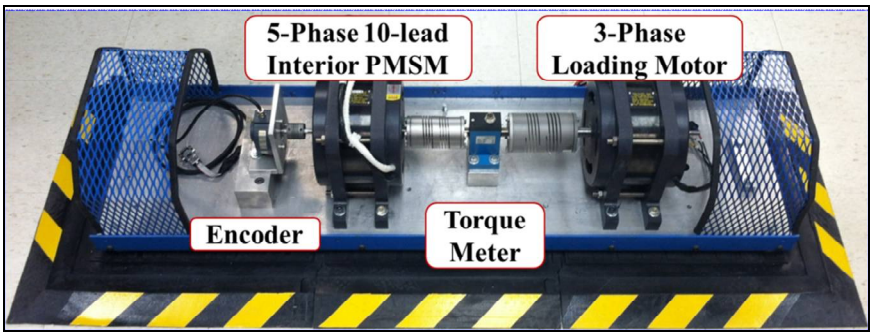

Fig. 93. 5-phase 10-lead interior PMSM control set-up connection.

Fig. 94 illustrates the entire control set-up for bipolar voltage switching method. The modified 5-phase 10-lead interior PMSM is connected to the encoder and torque meter. The 3-phase IPMSM with the resisters is loading the 5-phase 10-lead interior PMSM. The DSP board generates the gate signals and controls the IGBTs in the 5 H-bridge inverters through the interface board designed. As a result, the IGBTs power the 5-phase motor.

Proposed unipolar voltage switching method was implemented with the gate signal inverting board which was hand-constructed in Fig. 95. The switches in each inverter leg should be controlled independently of the other leg, so switch 2 and switch 4 are inverted and PWM1A only controls the leg “A”. Likewise, PWM1B controls the leg

"B". The inverter IGBTs are controlled by the floating point DSP, Delfino (F38225), though the interface board and the gate signal inverting board.

Fig. 96 shows the entire control set-up for unipolar voltage switching method. The gate signal inverting board is added to the set-up after the interface board.

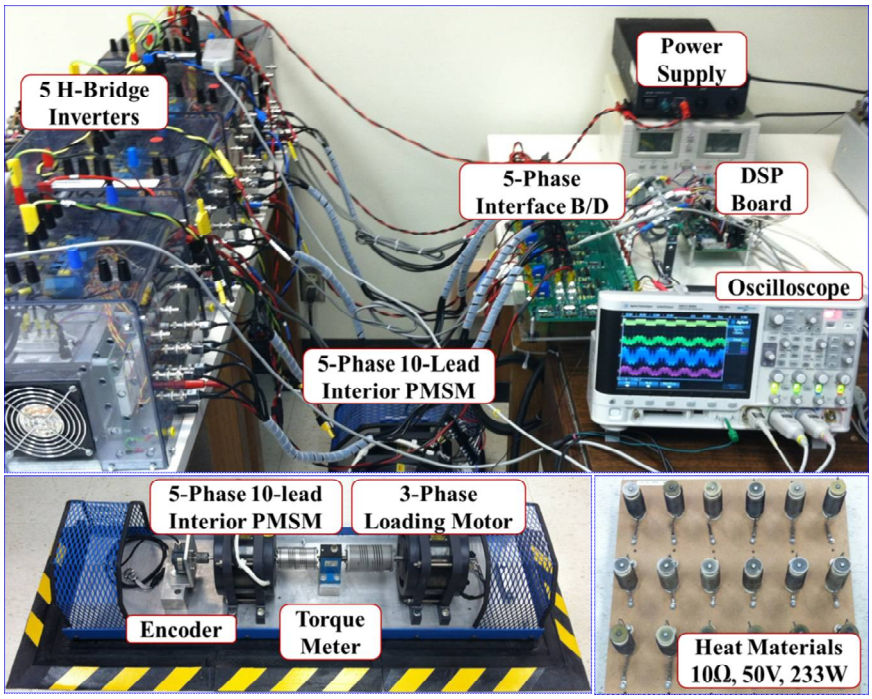

Fig. 94. Control set-up with bipolar voltage switching method.

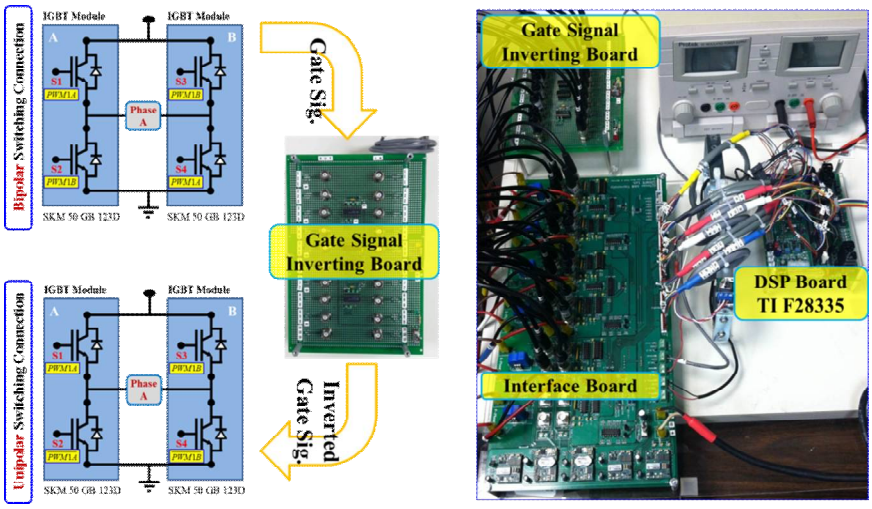

Fig. 95. Gate signal connection for unipolar voltage switching method.

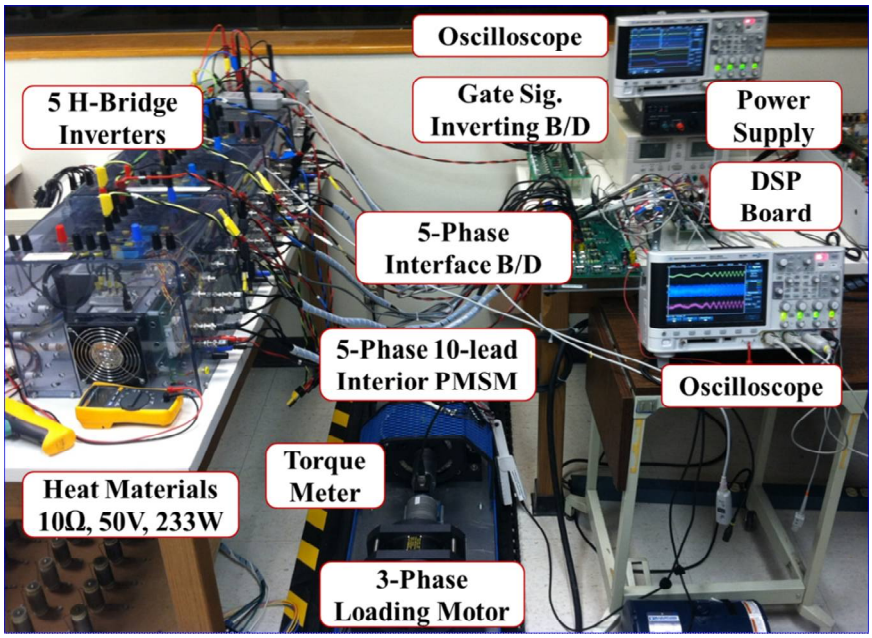

Fig. 96. Control set-up with unipolar voltage switching method.

5.3. PWM switching methods: bipolar and unipolar switching methods

5.3.1. PWM with bipolar voltage switching method

In this voltage switching method, switch 1 and switch 4 and switch 2 and switch 3 are paired and simultaneously turned on and off. One of the pairs is always on.

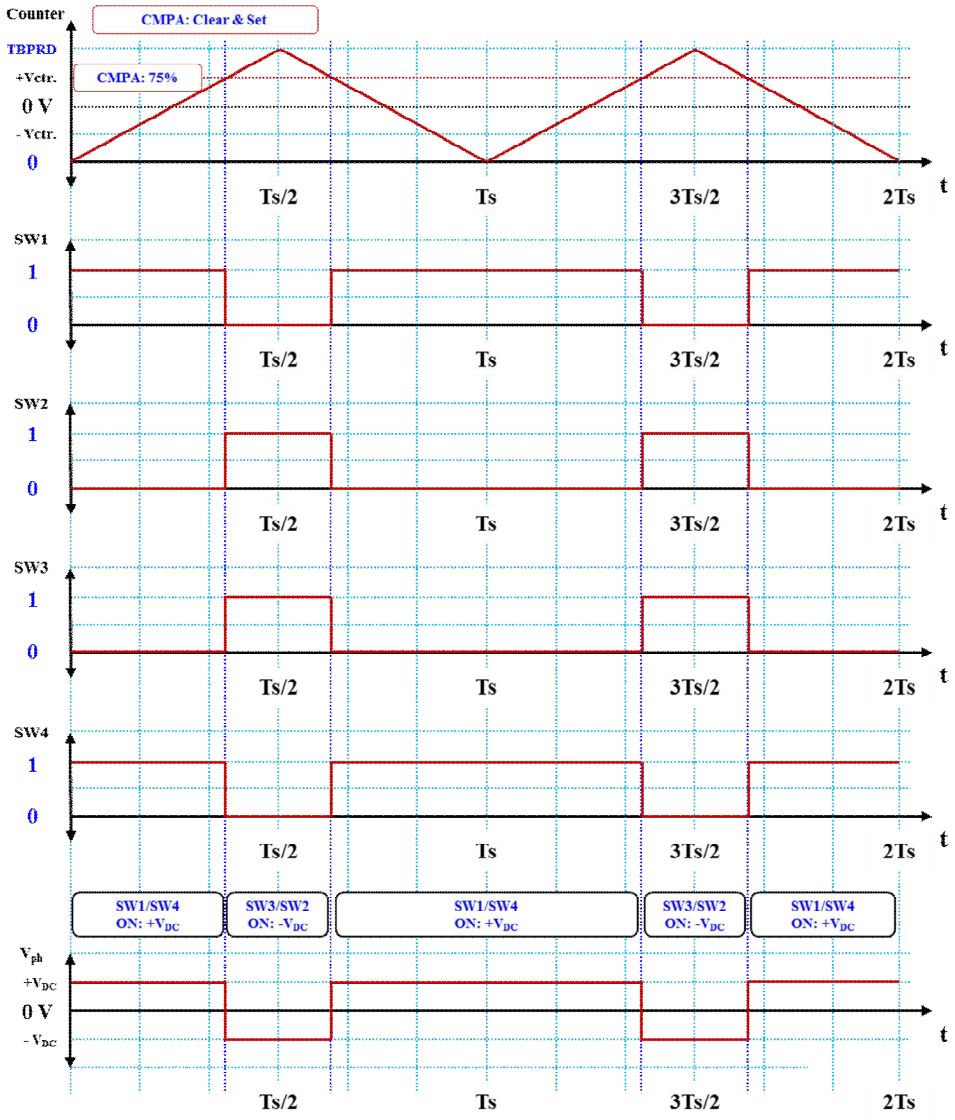

Fig. 97. Bipolar voltage switching method when CMPA ≥ 50%.

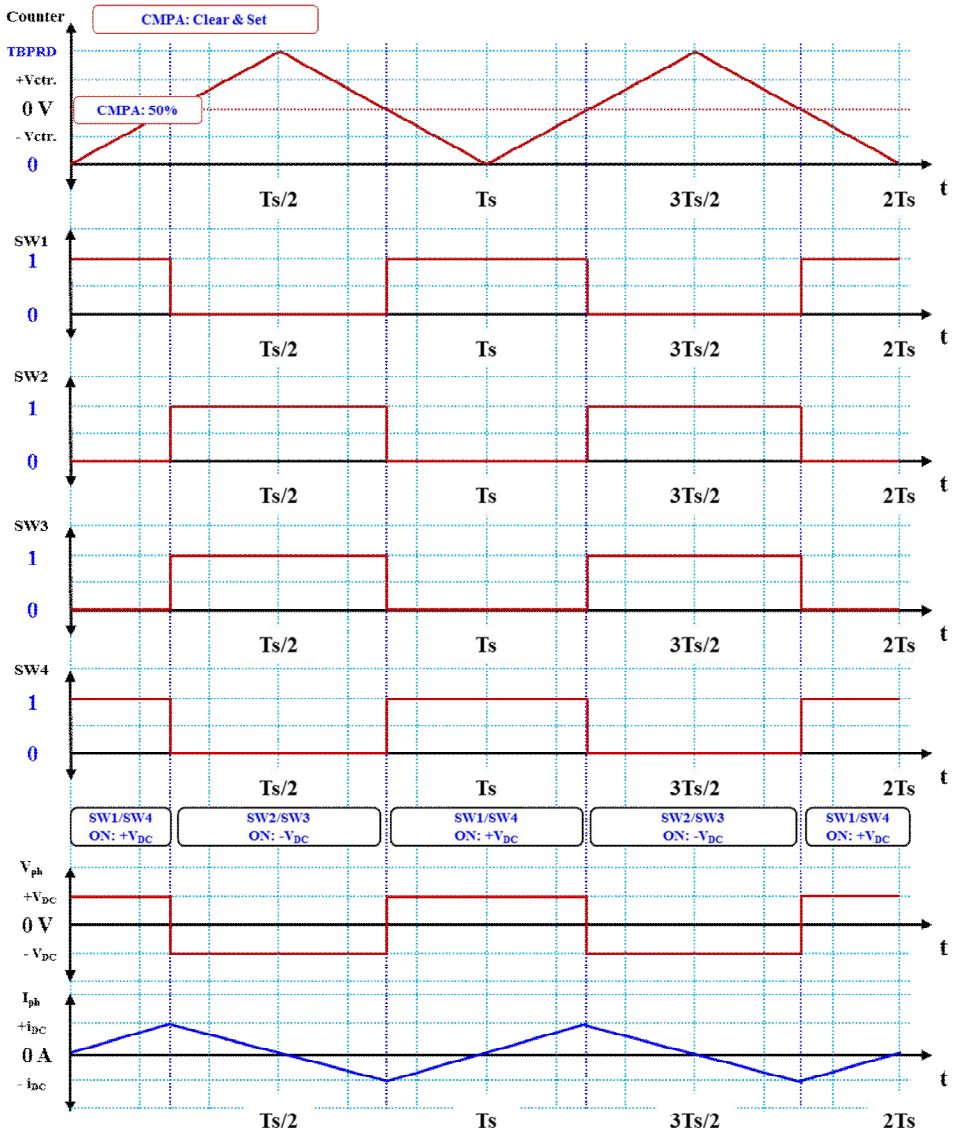

Fig. 98. Bipolar voltage switching method when CMPA = 50%.

The phase voltage is either positive V_{dc} or negative V_{dc}. Even in a zero voltage state, there is the positive and negative V_{dc} phase voltage, and the current is flowing as shown in Fig. 98. The average current is zero, but rms current is not zero. It makes to

control the motor difficult. Fig. 99 shows the experimental result which confirms the bipolar switching scheme explained.

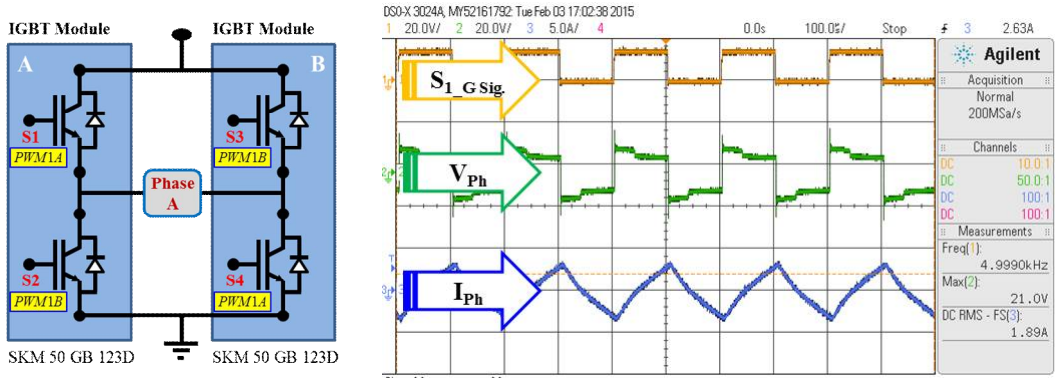

(a) **(b)**

Fig. 99. Bipolar voltage switching method when CMPA = 50%. (a) Gate signal connection. (b) Experimental phase voltage and current.

5.3.2. PWM with unipolar voltage switching method

PWM with unipolar voltage switching is also referred to as the double-PWM switching. The switches in each inverter leg are controlled independently but complementally. When the CMPA value is over than 50%, there is the positive V_{dc} phase voltage switching. Conversely, there is the negative V_{dc} phase voltage switching when the CMPA value is less than 50%. Because of the switching operations, the effective frequency of the output voltage waveform is doubled, and the current ripple is reduced. It results in a better output voltage waveform and a better frequency response [65]. Fig. 100 shows the switching voltages and the motor phase voltage when CMPA value is greater than 50%. Likewise, Fig. 101 depicts the ones when CMPA value is less than 50%.

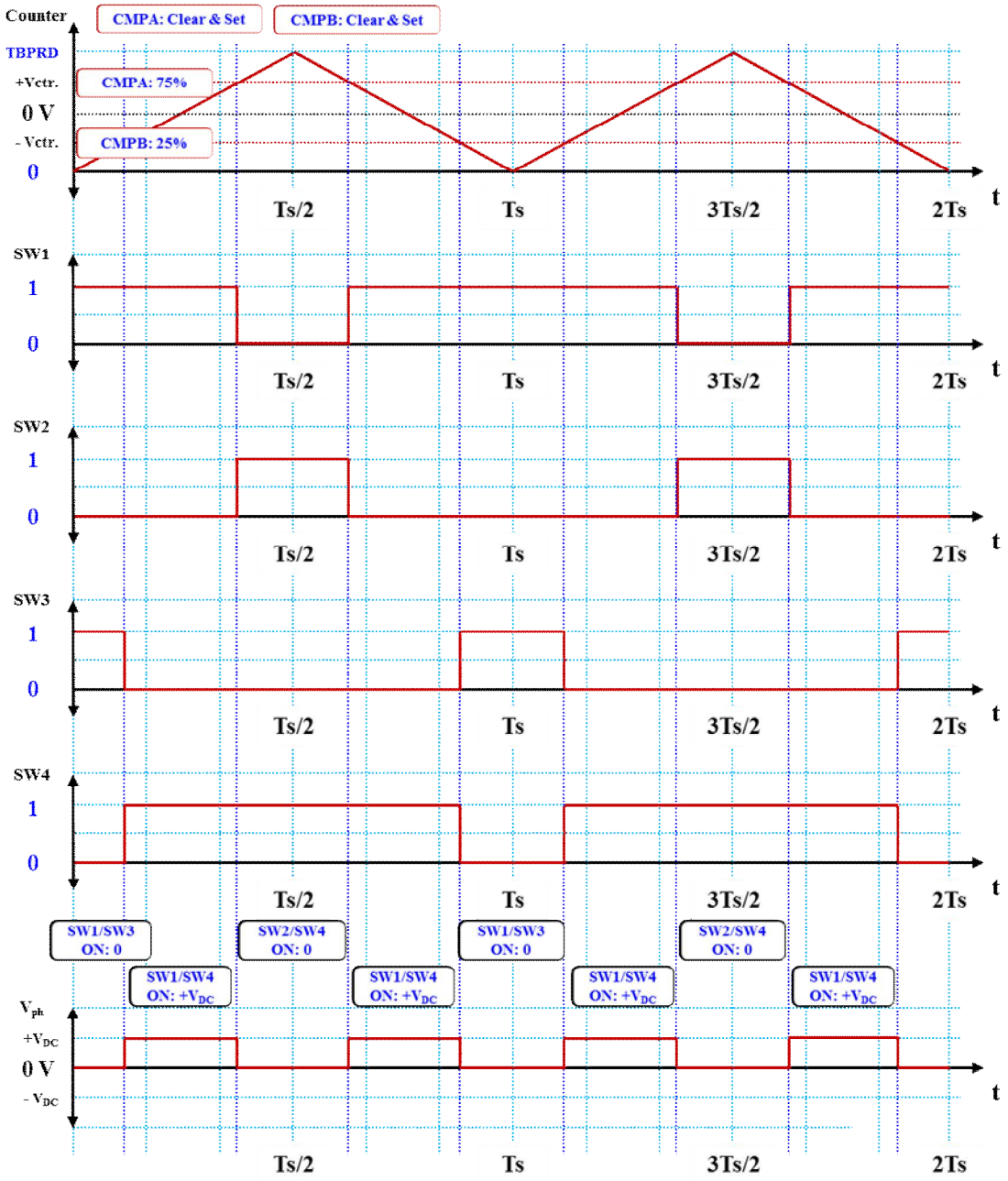

Fig. 100. Unipolar voltage switching method when CMPA ≥ 50%.

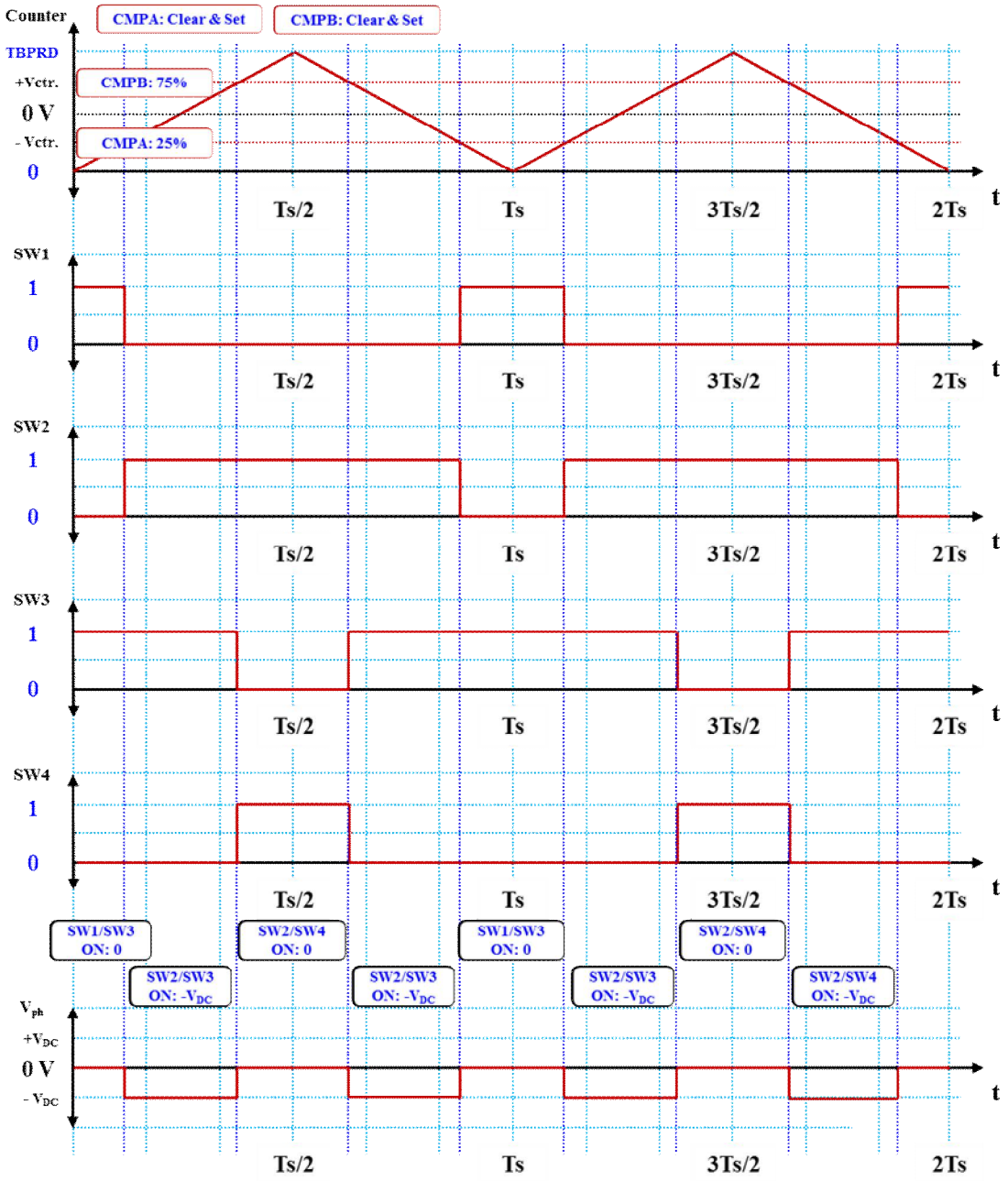

Fig. 101. Unipolar voltage switching method when CMPA ≤ 50%.

In a zero voltage state, there is no phase voltage and no current as shown in Fig. 102. Again, Fig. 103 shows the experimental results, and it confirms the switching scheme shown in Fig. 100, 101, and 102.

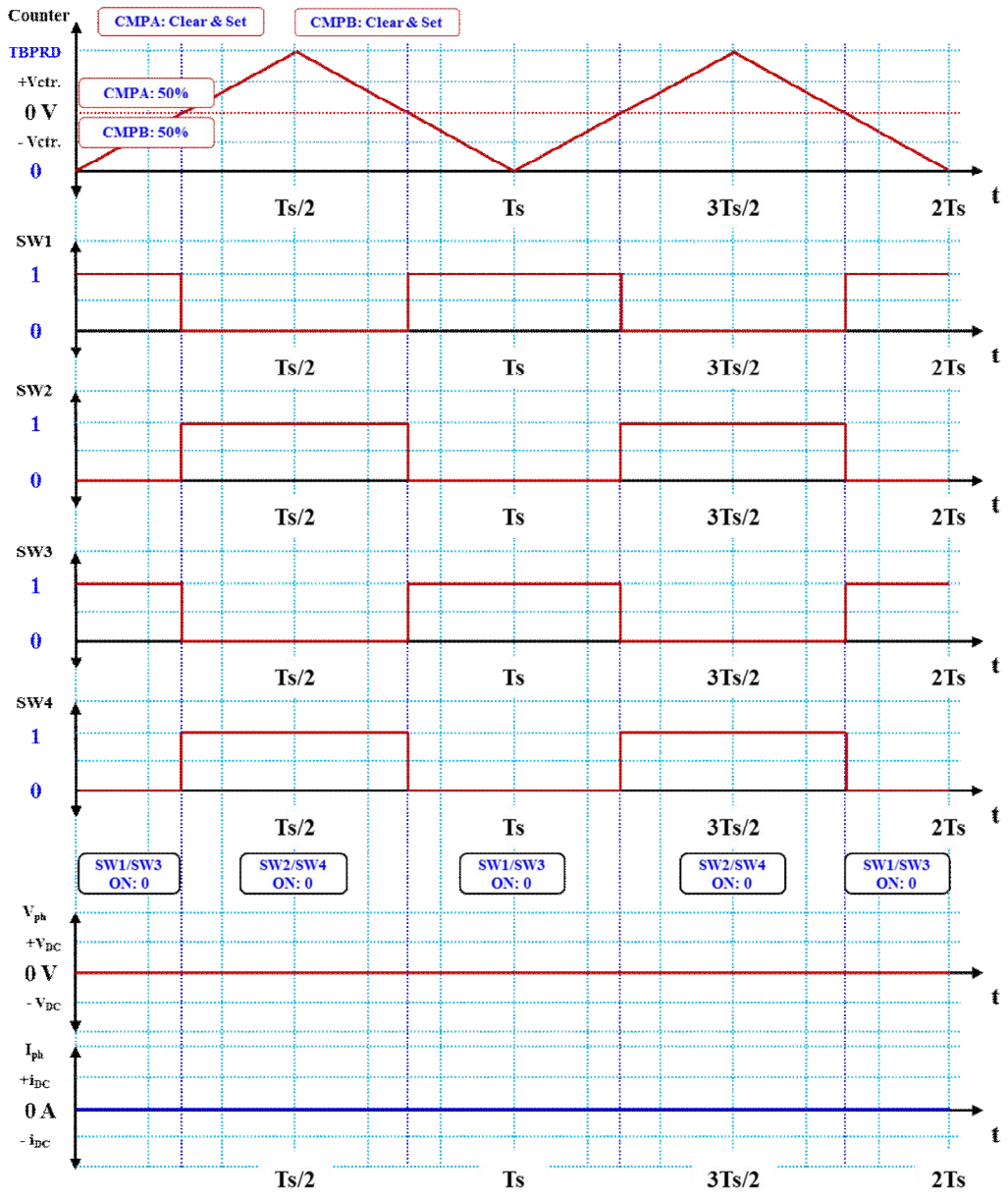

Fig. 102. Unipolar voltage switching method when CMPA =CMPB = 50%.

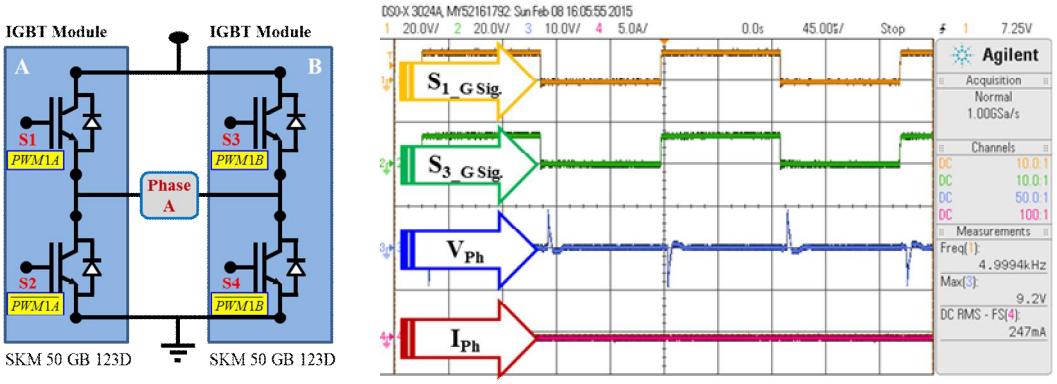

(a) **(b)**

Fig. 103. Unipolar voltage switching method when CMPA =CMPB = 50%. (a) Gate signal connection. (b) Experimental phase voltage and current.

5.4. 10-step VSI control

5-phase 10-lead inverter has 5 independent H-bridges as illustrated in Fig. 104. Each phase is separated from the others. Switching actions can have either bipolar or unipolar conditions. Based on the rotor position, an appropriate voltage vector needs to be applied to the motor in Fig. 105.

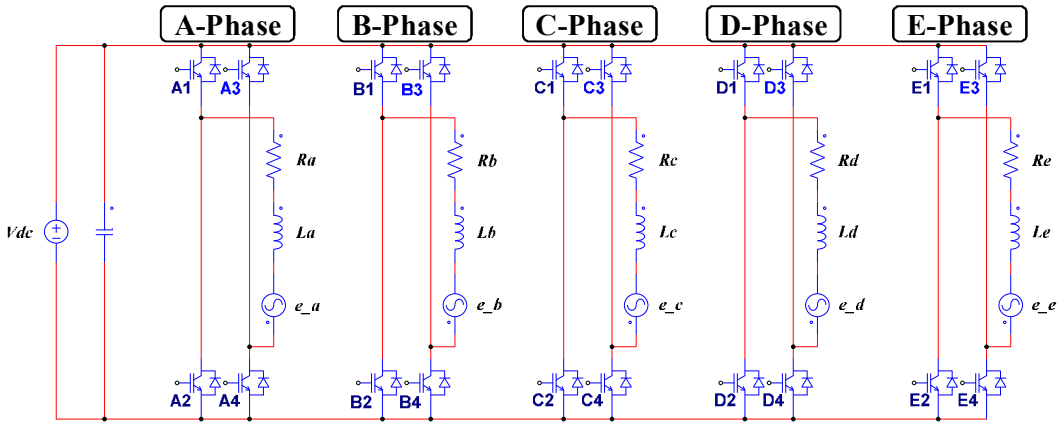

Fig. 104. Equivalent circuit diagram for 5-phase 10-lead interior PMSM.

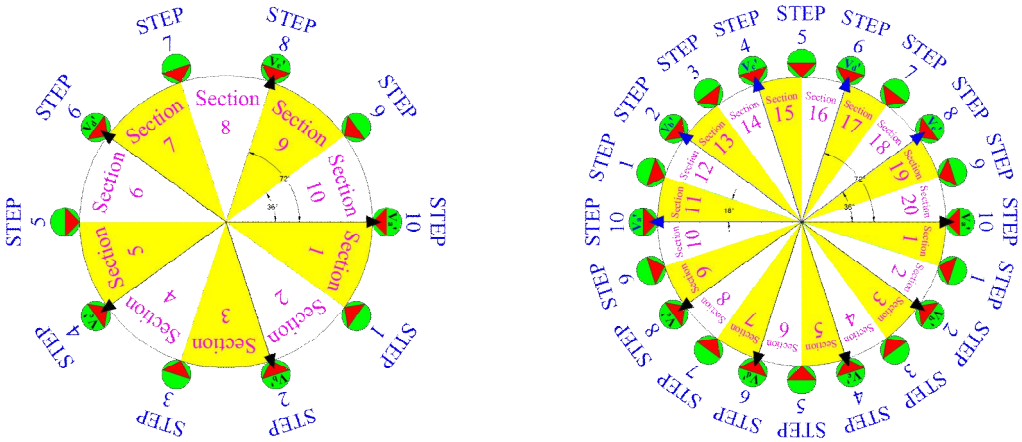

(a) **(b)**

Fig. 105. Voltage vector diagram for 5-phase 10-lead interior PMSM. (a) Electrical angle. (b) Mechanical angle.

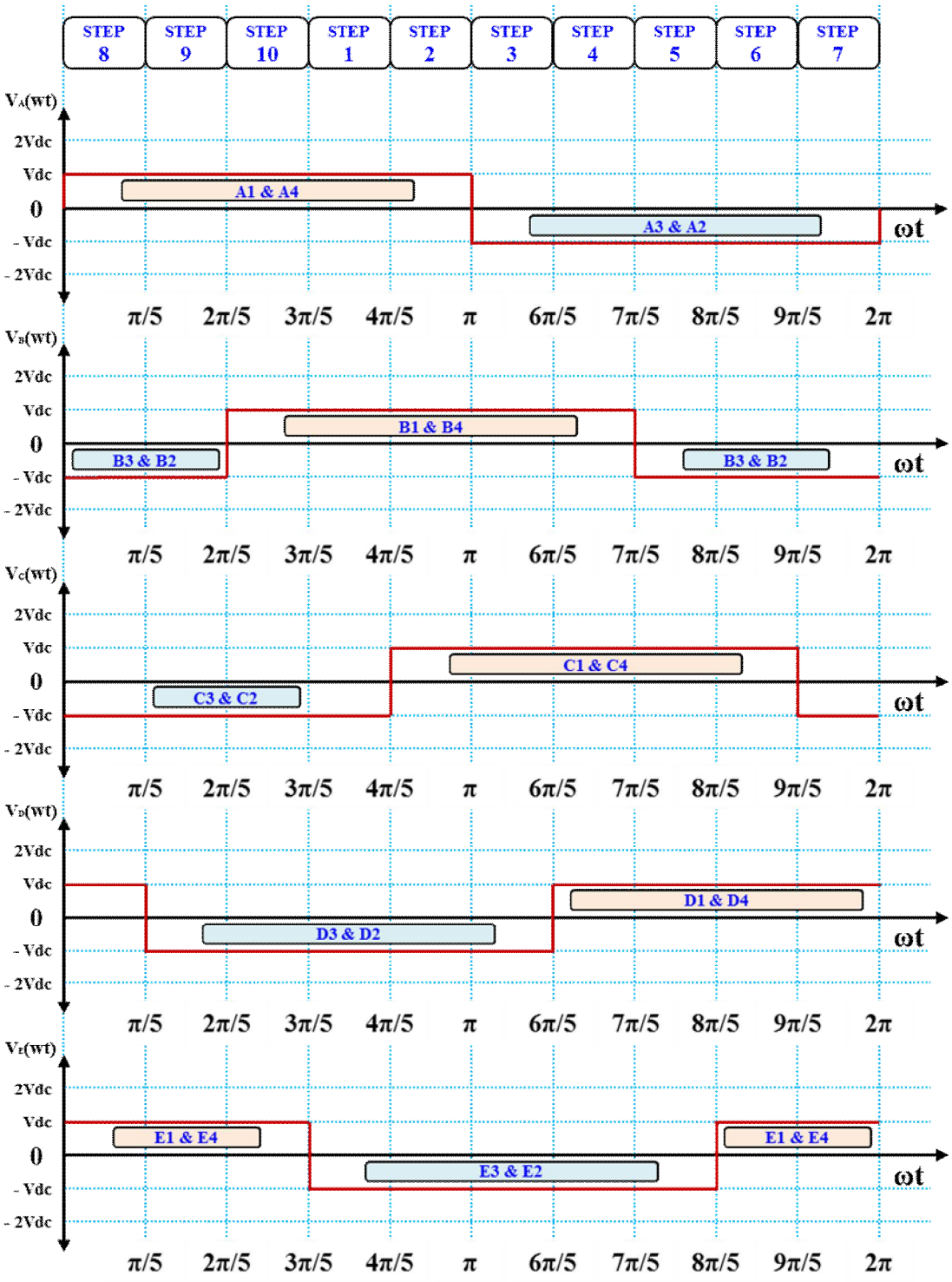

Fig. 106. Phase voltage waveforms for 5-phase 10-lead interior PMSM.

Fig. 106 shows phase voltage waveforms which result in 180˚ conduction for each IGBT in the inverter. The number of steps depends on how the encoder value changes. The switching conditions for each voltage vector are listed in Fig. 107.

From Fig. 108 to Fig. 118, the circuit currents flows are visualized between each switching transient.

STEP 8	STEP 9	STEP 10	STEP 1	STEP 2	STEP 3	STEP 4	STEP 5	STEP 6	STEP 7
+Va, -Vb, -Vc, +Vd, +Ve	+Va, -Vb, -Vc, +Vd, +Ve	+Va, -Vb, -Vc, +Vd, +Ve	+Va, -Vb, -Vc, +Vd, +Ve	+Va, -Vb, -Vc, +Vd, +Ve	+Va, -Vb, -Vc, +Vd, +Ve	+Va, -Vb, -Vc, +Vd, +Ve	+Va, -Vb, -Vc, +Vd, +Ve	+Va, -Vb, -Vc, +Vd, +Ve	+Va, -Vb, -Vc, +Vd, +Ve
A1/A4 B3/B2 C3/C2 D1/D4 E1/E4	A1/A4 B3/B2 C3/C2 D1/D4 E1/E4	A1/A4 B3/B2 C3/C2 D1/D4 E1/E4	A1/A4 B3/B2 C3/C2 D1/D4 E1/E4	A1/A4 B3/B2 C3/C2 D1/D4 E1/E4	A1/A4 B3/B2 C3/C2 D1/D4 E1/E4	A1/A4 B3/B2 C3/C2 D1/D4 E1/E4	A1/A4 B3/B2 C3/C2 D1/D4 E1/E4	A1/A4 B3/B2 C3/C2 D1/D4 E1/E4	A1/A4 B3/B2 C3/C2 D1/D4 E1/E4
1H/2L 3L 4H/5H	1H/2L 3L 4H/5H	1H/2L 3L 4H/5H	1H/2L 3L 4H/5H	1H/2L 3L 4H/5H	1H/2L 3L 4H/5H	1H/2L 3L 4H/5H	1H/2L 3L 4H/5H	1H/2L 3L 4H/5H	1H/2L 3L 4H/5H

Fig. 107. Switching conditions for each voltage vector.

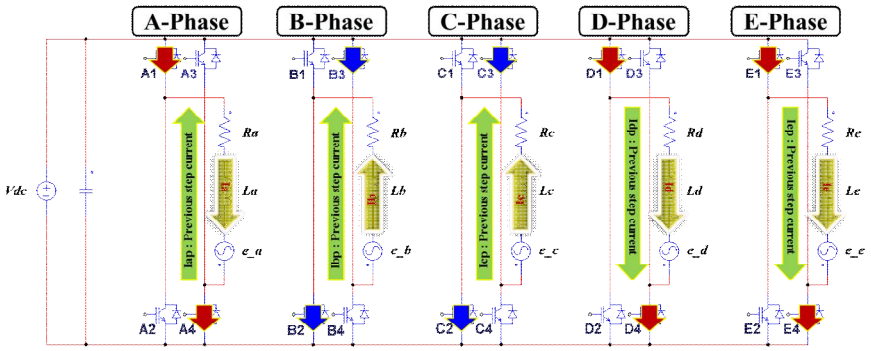

Fig. 108. Current flows at STEP 8.

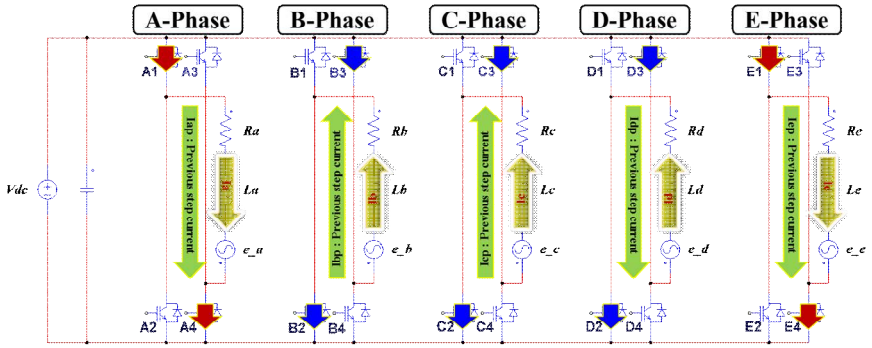

Fig. 109. Current flows at STEP 9.

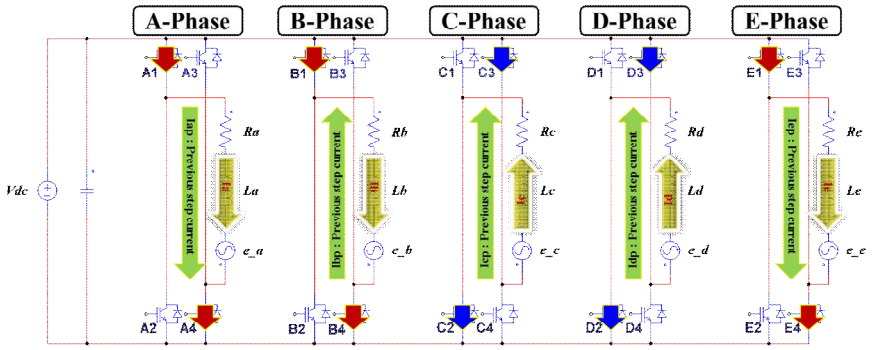

Fig. 110. Current flows at STEP 10.

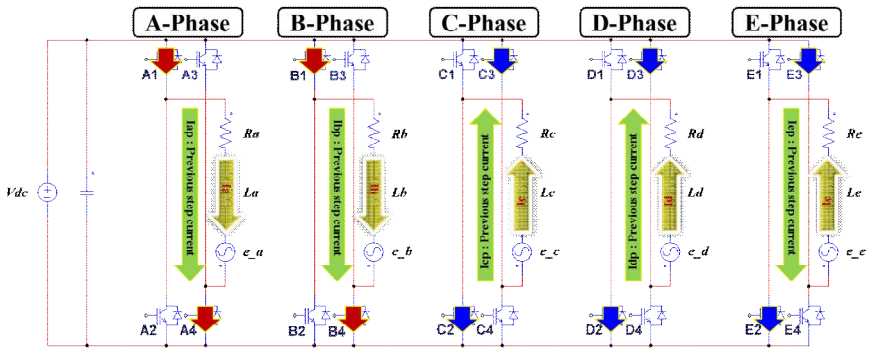

Fig. 111. Current flows at STEP 1.

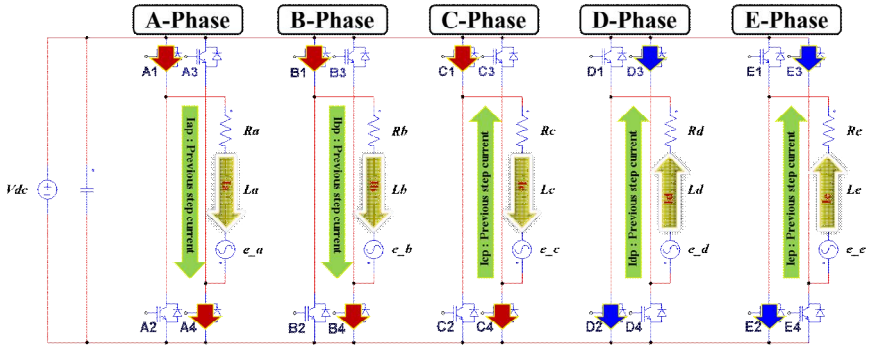

Fig. 112. Current flows at STEP 2.

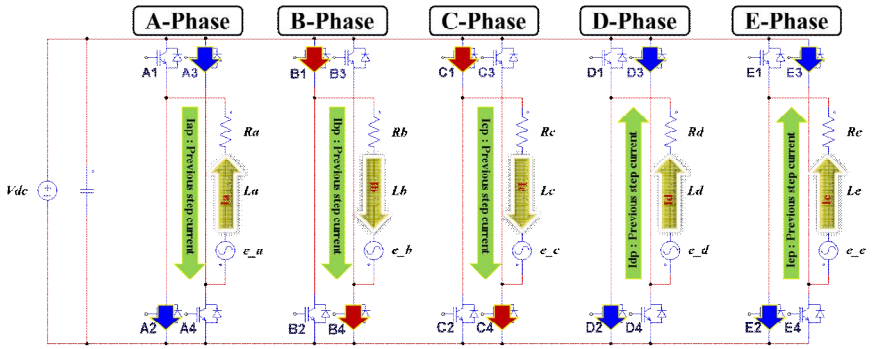

Fig. 113. Current flows at STEP 3.

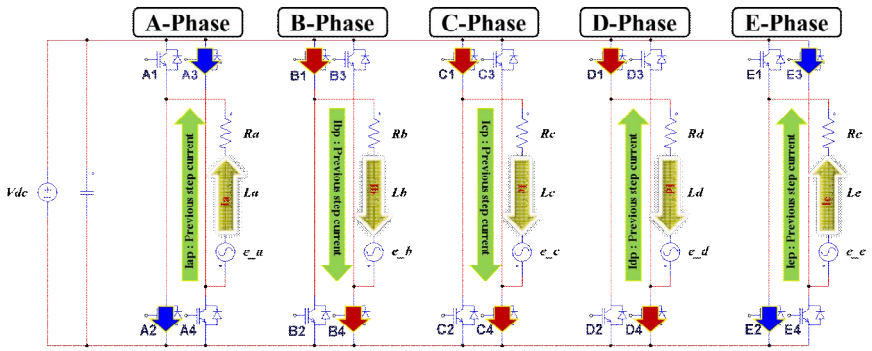

Fig. 114. Current flows at STEP 4.

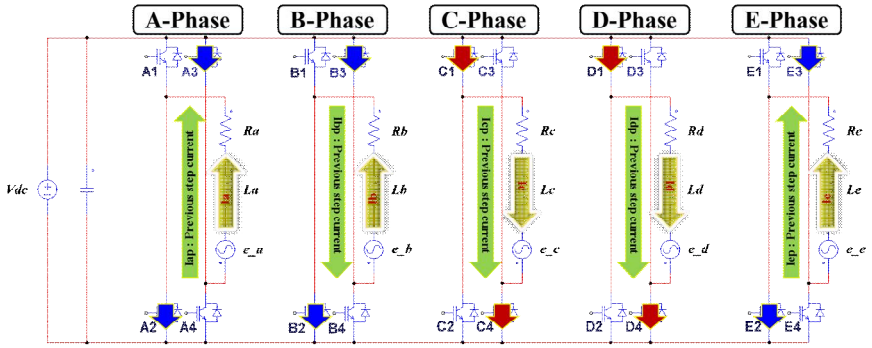

Fig. 115. Current flows at STEP 5.

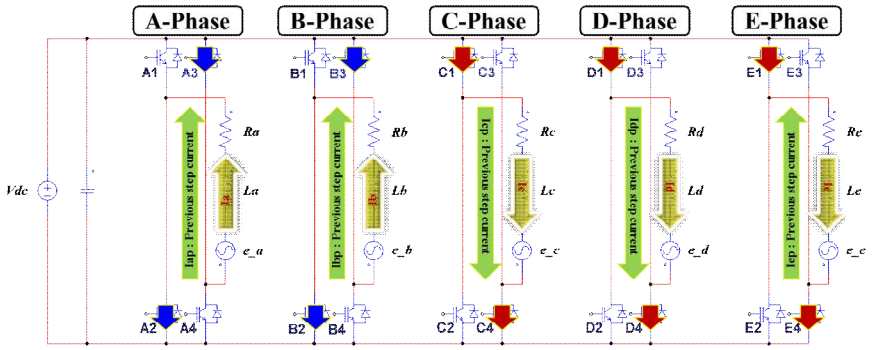

Fig. 116. Current flows at STEP 6.

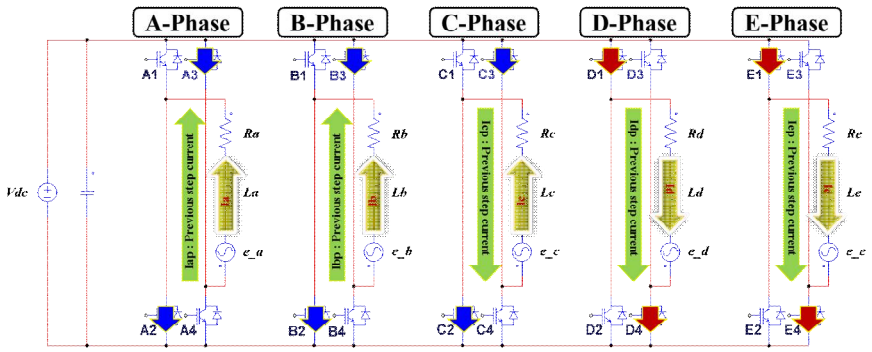

Fig. 117. Current flows at STEP 7.

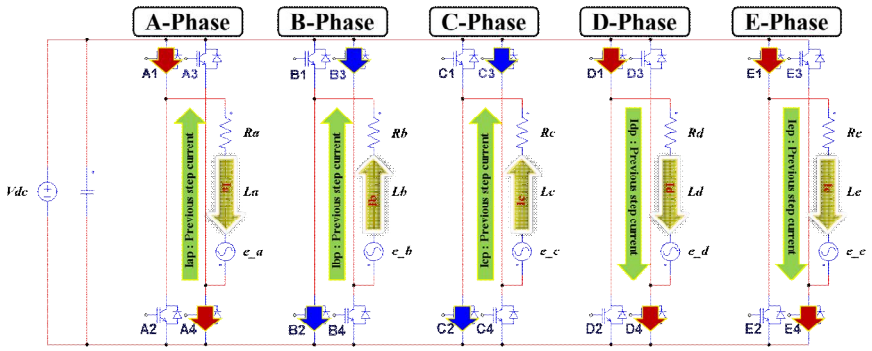

Fig. 118. Current flows at STEP 8.

Gate signals for 10-step VSI control is compared under the same operating condition in Fig. 119 and Fig. 120. For the bipolar switching method, the phase voltages show the bipolar switching between the positive V_{dc} and negative V_{dc}. For the unipolar switching method, the phase voltages show the unipolar switching either between zero and the positive V_{dc} or between zero and the negative V_{dc} in Fig. 120. There is a significant current ripple difference between two switching methods.

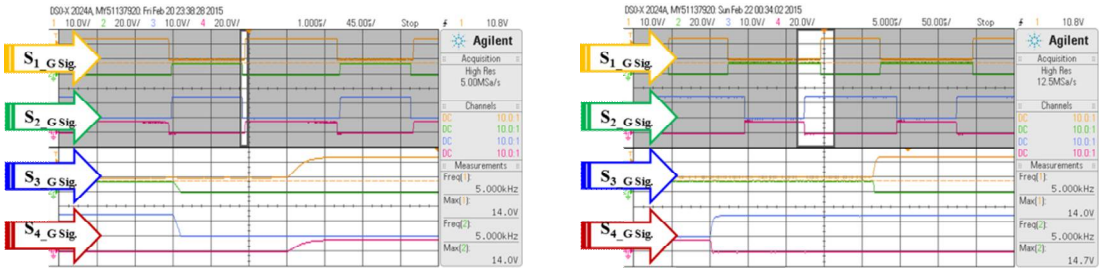

(a) **(b)**

Fig. 119. Comparison of Gate signals. (a) Bipolar switching method. (b) Unipolar switching method.

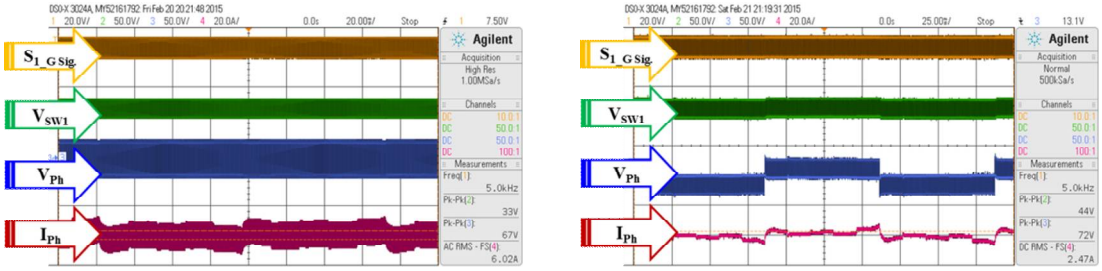

(a) **(b)**

Fig. 120. Comparison of phase voltages and currents. (a) Bipolar switching method. (b) Unipolar switching method.

5.5. SPWM control

5.5.1. In a-b-c-d-e reference frame (Stationary Ref. Frame)

The gating signals are generated by comparing a sinusoidal reference signal with a triangular carrier wave of frequency. The frequency of reference signal determines the inverter output frequency and its peak amplitude controls the modulation index and output voltage.

In the diagram shown in Fig. 121, the current references are generated from the speed loop with the advanced current angle (θ_{Iph}), and then they are compared with each phase current from the current sensors. Each PI controller generates the voltage commands, and they control the motor.

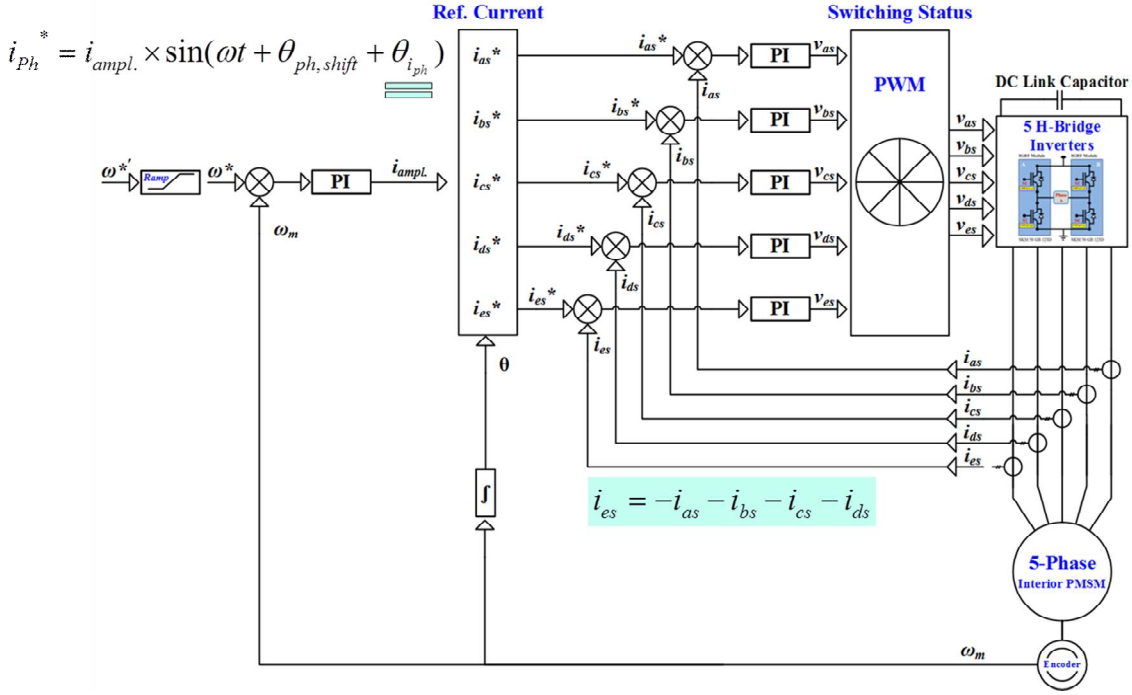

Fig. 121. Diagram of SPWM control method in stationary reference frame.

Fig. 122 shows the response of the phase current following the reference. At low speed, there is almost no back-EMF, so that the phase current corresponds to the sinusoidal reference current perfectly. However, the phase current exhibits harmonics from the back-EMF at the high speed, but it still follows the reference.

Gate signals are compared in Fig. 123, and the inverter legs are working independently in unipolar switching method.

In stationary reference frame, the reference current is sinusoidal, and the phase current is following the reference current shown in Fig. 124.

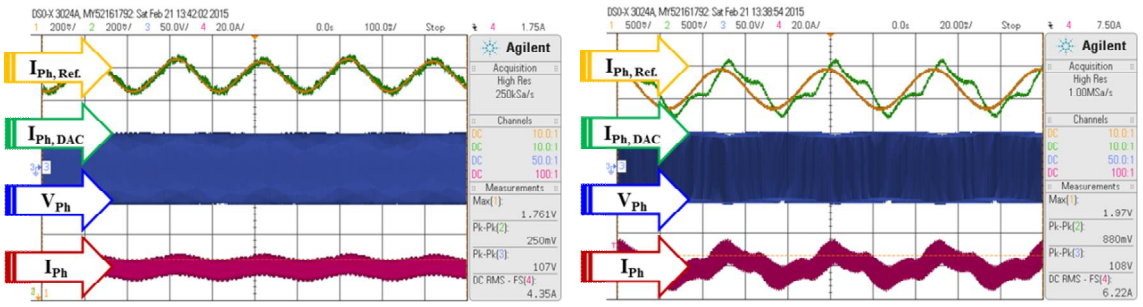

(a) **(b)**

Fig. 122. Current reference response. (a) At low speed. (b) At high speed.

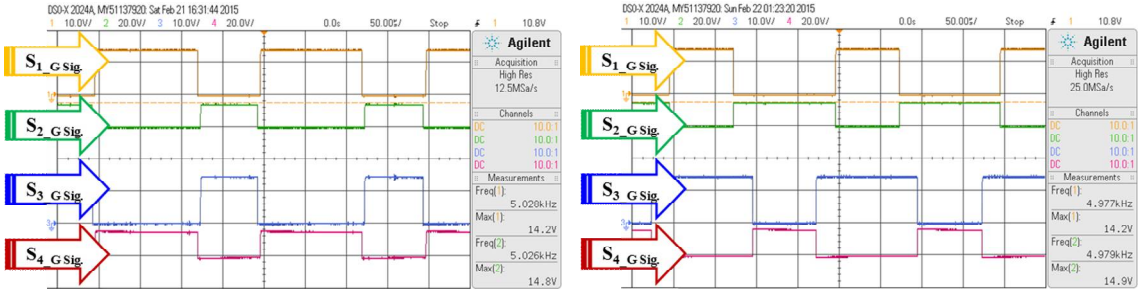

(a) **(b)**

Fig. 123. Comparison of Gate signals. (a) Bipolar switching method. (b) Unipolar switching method.

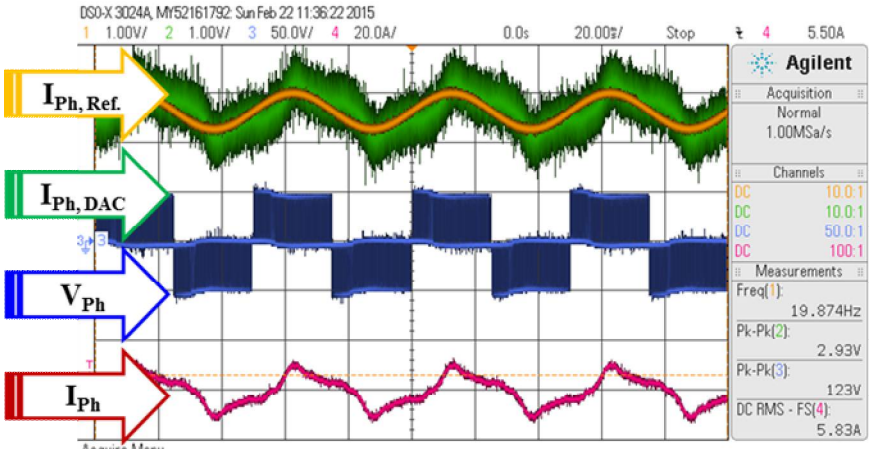

Fig. 124. Reference current response in stationary reference frame.

The phase voltage shows the bipolar and unipolar switching actions, and there is significant current ripple difference in Fig. 125. Torque is measured under 560W loading condition at 1200rpm in Fig. 126. Fig. 127 indicates that the real speed follows the reference speed with a ramp function implemented after closing the speed loop.

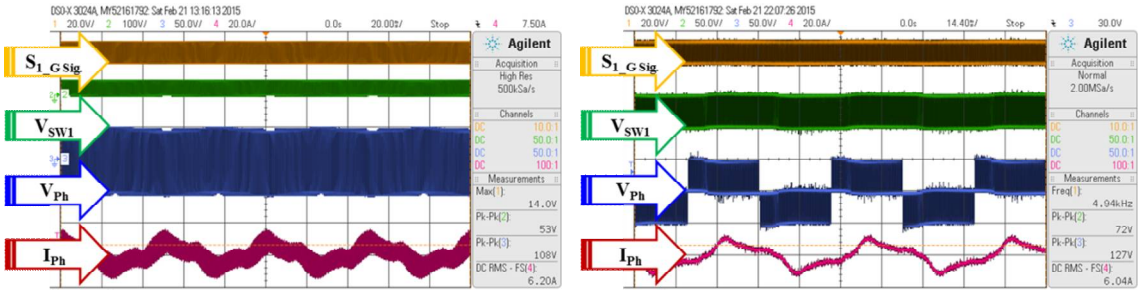

(a) **(b)**

Fig. 125. Comparison of phase voltages and currents. (a) Bipolar switching method. (b) Unipolar switching method.

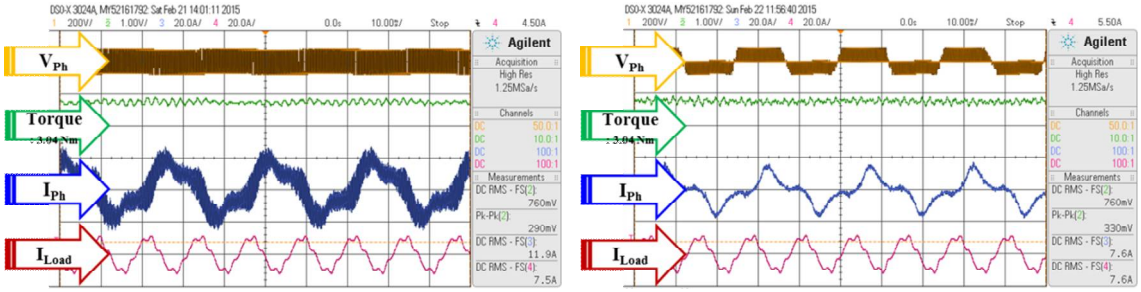

(a) **(b)**

Fig. 126. Comparison of torque at 1200rpm with 560W load. (a) Bipolar switching method. (b) Unipolar switching method.

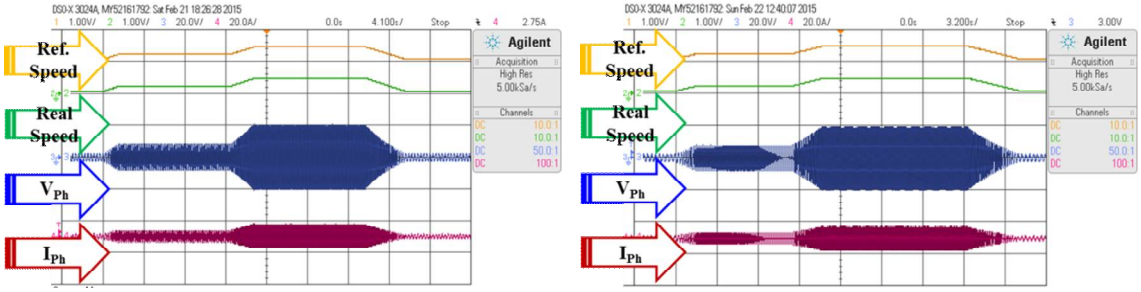

(a) **(b)**

Fig. 127. Comparison of speed loop response. (a) Bipolar switching method. (b) Unipolar switching method.

5.5.2. *In d-q reference frame (Rotating Ref. Frame)*

In the diagram for rotating reference frame shown in Fig. 128, the reference i_q current is generated from the speed loop, and the i_d and i_q currents from the transformation are compared with the reference currents. These PI controllers generate V_d and V_q voltage commands, and each phase command is obtained after the inverse transformation. These commands control the motor.

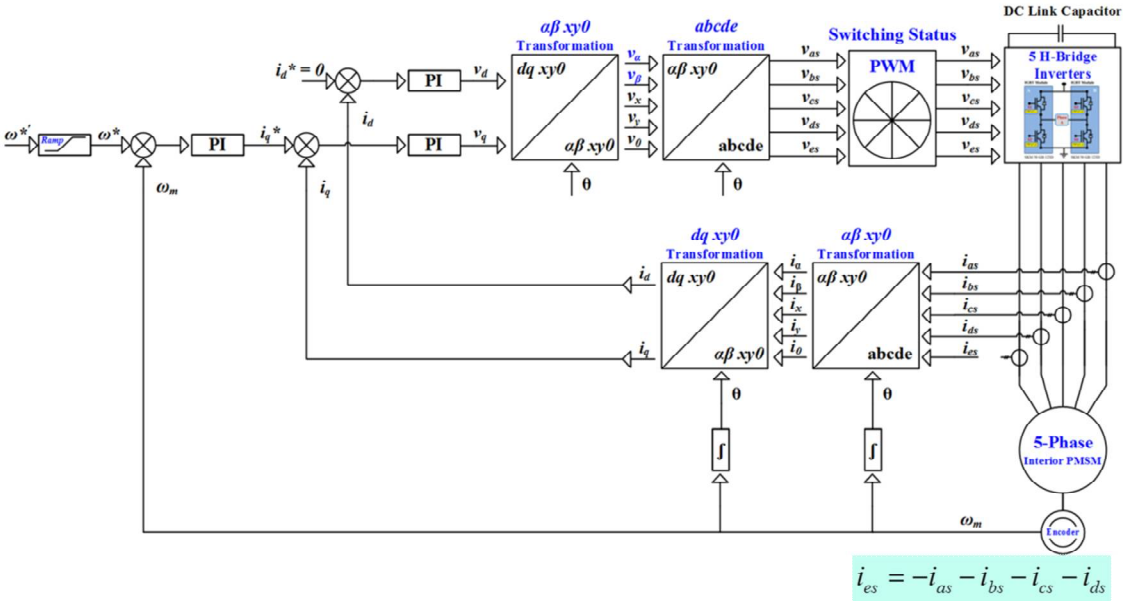

Fig. 128. Diagram of SPWM control method in rotating reference frame.

Gate signals are compared in Fig. 129, and the inverter legs are working independently in unipolar switching method.

In rotating reference frame, the reference current is a DC, and the i_q current is following the reference current shown in Fig. 130.

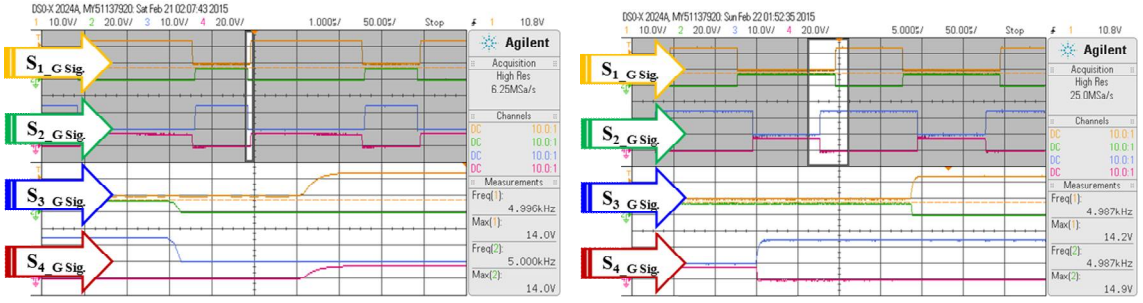

(a) **(b)**

Fig. 129. Comparison of Gate signals. (a) Bipolar switching method. (b) Unipolar switching method.

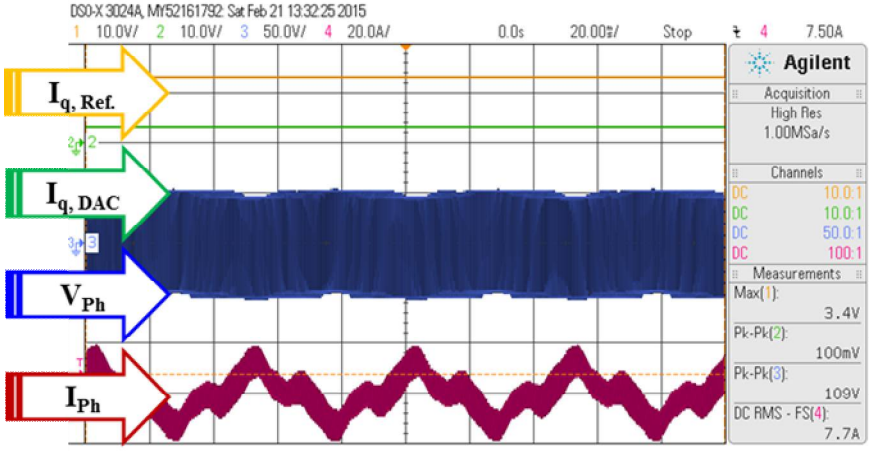

Fig. 130. Reference current response in stationary reference frame.

The phase voltage shows the bipolar and unipolar switching actions, and there is significant current ripple difference in Fig. 131. Torque is measured under 560W loading condition at 1200rpm in Fig. 132. Fig. 133 indicates that the real speed follows the reference speed with a ramp function implemented after closing the speed loop.

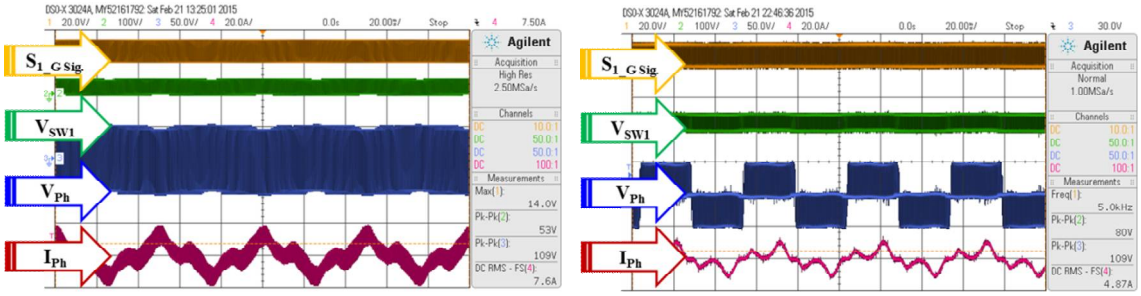

(a) **(b)**

Fig. 131. Comparison of phase voltages and currents. (a) Bipolar switching method. (b) Unipolar switching method.

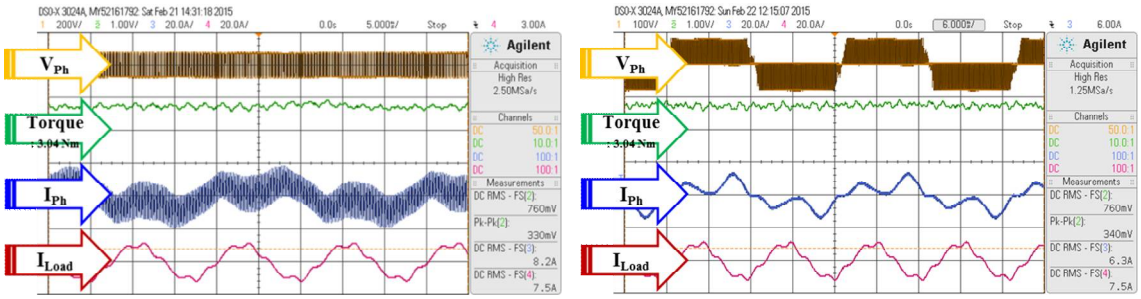

(a) **(b)**

Fig. 132. Comparison of torque at 1200rpm with 560W load. (a) Bipolar switching method. (b) Unipolar switching method.

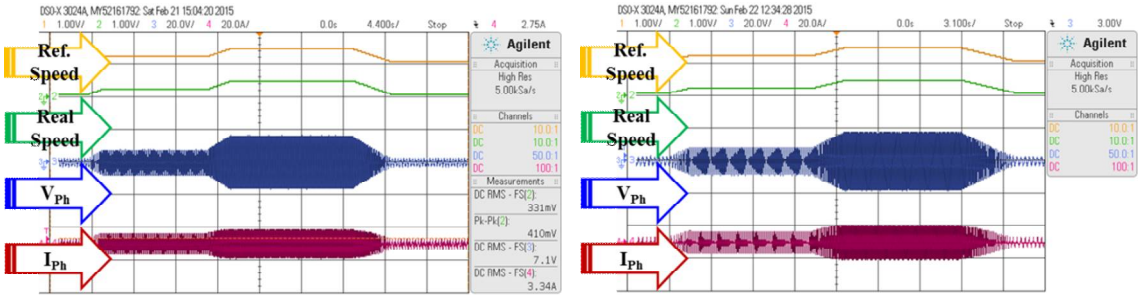

(a) **(b)**

Fig. 133. Comparison of speed loop response. (a) Bipolar switching method. (b) Unipolar switching method.

5.6. Hysteresis control

Among the various PWM techniques, the hysteresis band current control is used very often because of its simplicity of implementation. Also, besides fast response current loop, the method does not need any knowledge of load parameters. However, the current control with a fixed hysteresis band has the disadvantage that the PWM frequency varies within a band because peak to peak current ripple is required to be controlled at all points of the fundamental frequency wave. For some applications such military traction or ship propulsion systems, the hysteresis control is mainly used. Therefore it is necessary to evaluate the control method.

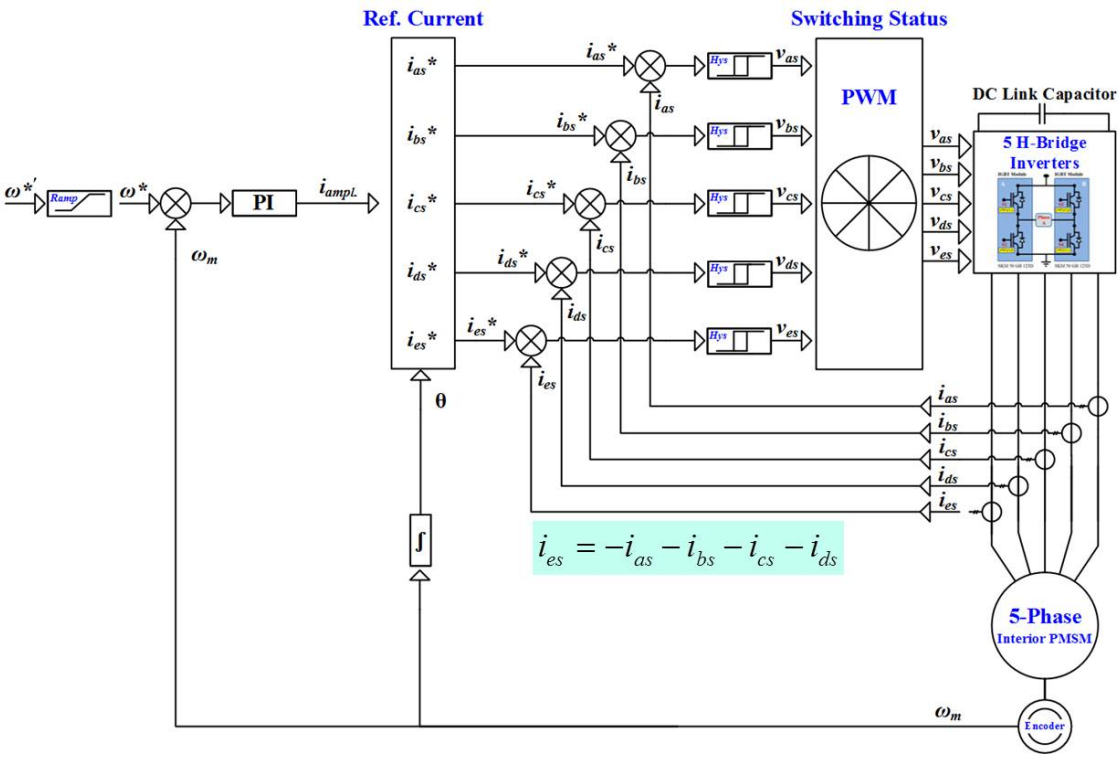

Fig. 134. Diagram of Hysteresis control method.

In Fig. 134, the control diagram is very much like the SPWM in stationary reference frame, but the hysteresis switching method was used with a 5% hysteresis band at 5kHz sampling frequency instead of using the PI controllers.

For the both switching method, the gate signals are compared, and the signals shows the phase voltages are applying correctly in Fig. 135. The speed loops are closed and the phase is following the reference closely. The phase currents flow depending on the applied phase voltages as depicted in Fig. 136.

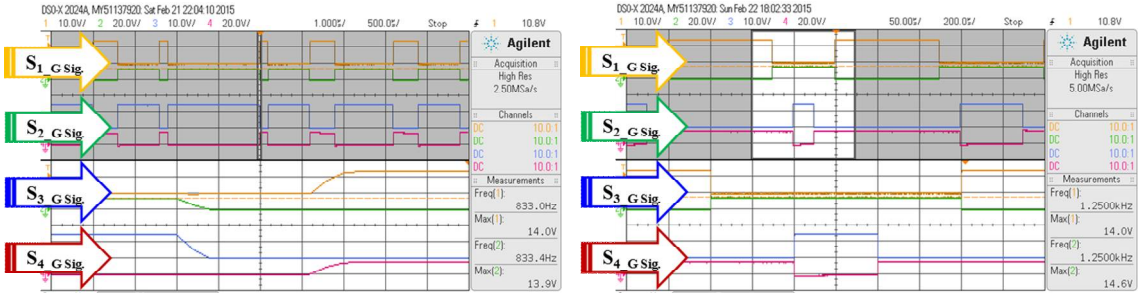

(a) **(b)**

Fig. 135. Comparison of Gate signals. (a) Bipolar switching method. (b) Unipolar switching method.

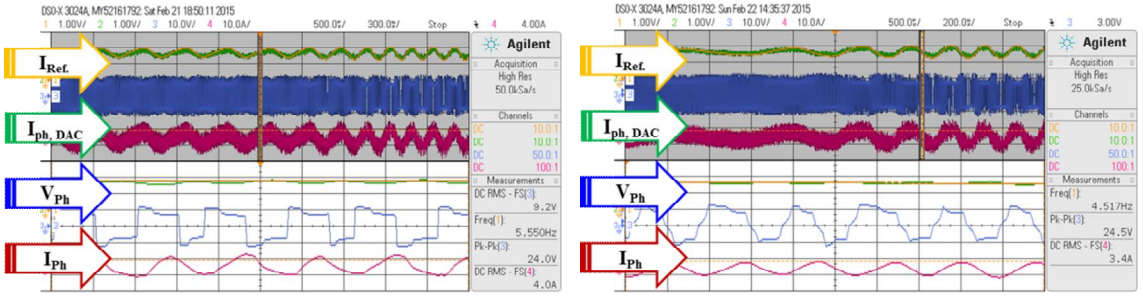

(a) **(b)**

Fig. 136. Comparison of Gate signals. (a) Bipolar switching method. (b) Unipolar switching method.

5.7. Summary

A reconfigurable motor control set-up was built with an encoder, a torque meter, a 3-phase interior PMSM, register load, a 3-phase induction motor. An effective switching method was proposed and implemented in the motor control drive. 10-step VSI control, SPWM in stationary and rotating reference frames, hysteresis control methods were evaluated with the 5-phase 10-lead interior PMSM.

6. CONCLUSIONS AND FUTURE WORK

In this dissertation, a 5-phase 10-lead Interior PMSM was designed with the proposed design method, and an optimization theory called "Response Surface Methodology" was introduced. Moreover, an inverter board block diagram and a concept of the control signal generation were introduced, and then a multi-phase inverter interface board was designed and evaluated with the TI floating point DSP, Delfino (F28335). To evaluate the 5-phase 10-lead interior PMSM systems, a reconfigurable motor control set-up for both a multi-phase and a 3-phase motors was built with the 5-phase IPMSM, 3-phase IPMSM motor, encoder, torque meter, resister heat materials, and induction motor. The test set-up could be for either a multi-phase control system or a 3-phase control system. An effective switching method was proposed and implemented in the motor control drive. Step VSI control was applied with bipolar and unipolar switching methods and the speed loop was closed with PI controllers. Reference frame transformation for 5-phase motor was discussed and used in the SPWM current regulation. Sine PWM control method was implemented in both stationary and rotating reference frames. Both bipolar and unipolar switching methods were used for the SPWM current control method and compared. Hysteresis control method was also implemented with PWM and GPIO switching methods.

Overall, the proposed multi-phase fault tolerant PMSM drive systems could be the future of the electric vehicle traction and ship propulsion systems.

5-phase 10-lead interior is a unique structure for EV traction or ship propulsion applications, and a unique structure machine comes many research opportunities. A few potential paths of research are suggested here:

- High power multi-phase PMSM needs to designed and its control methods needs to be researched
- More current control methods need to be researched to minimize the torque ripple, vibration, and noise: SVPWM, Random SPWM, etc.
- The inverter part needs to be optimized.
- Various control methods needs to be researched under each fault condition
- Sensorless control also needs to be researched for this multi-phase interior PMSM.

REFERENCES

[1] R. Shi, H.A. Toliyat, and A. El-Antably, "A DSP-Based Direct Torque Control of Five-Phase Synchronous Reluctance Motor Drive," Applied Power Electronics Conference and Exposition(APEC), 2001. Sixteenth Annual IEEE vol. 2, pp. 1077-1082, 2001.

[2] N.P. Ananthamoorthy; and K. Baskaran, "Simulation of PMSM based on Current Hysteresis PWM and Fed PI Controller," Computer Communication and Informatics (ICCCI), 2012 International Conference on Digital Object Identifier: 10.1109/ICCCI.2012.6158897, pp. 1-5, 2012.

[3] H.Y. Choi, S.J. Park, Y.K. Kong, and J.G. Bin, "Design of Multi-phase Permanent Magnet Motor for Ship Propulsion," in Proc. of ICEMS, Tokyo, Japan, pp. 1-4, Nov. 2009.

[4] G.Z. Wu, and H.Y. Zhu, "Combined Hysteresis Current-Controlled PWM Inverter and Robust Control for a Permanent-Magnet Synchronous Motor," Electric Information and Control Engineering (ICEICE), 2011 International Conference on Digital Object Identifier: 10.1109/ICEICE.2011.5778376, pp. 5753-5757, 2011.

[5] M. Ehsani, Y. Gao, S.E. Gay and A. Emadi, "Modern Electric, Hybrid Electric, and Fuel Cell Vehicles: Fundamentals, Theory, and Design," CRC Press, Taylor & Francis Group, Boca Raton, Florida, USA, 2010.

[6] H. W. Cho, S. –M., Jang, and S. –K., Choi, "A Design Approach to Reduce Rotor Losses in High-Speed Permanent Magnet Machine for Turbo-Compressor," IEEE Transactions on Magnetics, vol. 42, pp. 3521-3523, Oct. 2006.

[7] D. K. Woo, S. Y. Lee, J. H. Seo, and H. K. Jung, "Optimal Rotor Structure Design of Interior-Permanent Magnet Synchronous Machine Based on Improved Niching Genetic Algorithm," ICEM 2008, 18th International Conference on, pp. 1-4, 2008.

[8] J. Z. Zhang, M. Cheng, and Z. Chen, "Optimal Design of Stator Interior Permanent Magnet Machine with Minimized Cogging Torque for Wind Power Application," Energy Conversion and Management, vol. 49, pp. 2100-2105, Aug. 2008.

[9] J. Z. Zhang, M. Cheng, and W. Hua, "Optimal Design of Stator Interior Permanent Magnet Machine Based on Finite Element Analysis," Journal of Applied Physics, vol. 105, issue 7, Apr. 2009.

[10] R. Dutta and M. F. Rahman, "Design and Analysis of an Interior Permanent Magnet (IPM) Machine with Very Wide Constant Power Operation Range," IEEE Transactions on Energy Conversion, vol. 23, pp. 25-33, Mar. 2008.

[11] C. Koutroulis, AG Kladas, and AG Mamalis, "Advanced Permanent Magnet Machine Design and Construction for Wind Power Generation and Traction Applications," International Journal of Applied Electromagnetics and Mechanics, vol. 13, pp. 285-290, 2001.

[12] L. Y. Xu, Lurong Ye, Li Zhen, and Ahmed El-Antably, "A New Design Concept of Permanent-Magnet Machine for Flux Weakening Operation," IEEE Transactions on Industry Applications, vol. 31, pp. 373-378, Mar. - Apr. 1995.

[13] J. H. H. Kuhlmann, "Design of Electrical Apparatus 2nd Edition," J. Wiley and Sons, Incorporated, 1940.

[14] C.-M. Ong, "Dynamic Simulation of Electric Machinery: Using MATLAB/SIMULINK," Prentice Hall PTR, 1998.

[15] T. M. Jahns, and Nicola Bianchi, "Design, Analysis, and Control of Interior PM Synchronous Machines: Tutorial Course Notes," by the IEEE-IAS Electrical Machines Committee, Oct. 2004.

[16] D. W. Novotny and T. A. Lipo, "Vector Control and Dynamics of AC Drives," Oxford University Press, 1996.

[17] D. Ishak, Z. Q. Zhu, and D. Howe, "High Torque Density Permanent Magnet Brushless Machines with Similar Slot and Pole Numbers," Journal of Magnetism and Magnetic Materials, vol. 272, pp. E1767-E1769, May 2004.

[18] D. Ishak, Z. Q. Zhu, and D. Howe, "Permanent-Magnet Brushless Machines with Unequal Tooth Widths and Similar Slot and Pole Numbers," IEEE Transactions on Industry Applications, vol. 41, pp. 584-590, Mar.-Apr. 2005.

[19] J. Rens, K. Atallah, S. D. Calverley, and D. Howe, "A Novel Magnetic Harmonic Gear," IEEE Trans. Ind. Appl., vol. 46, pp. 206-212, 2010.

[20] B. Stumberger, G. Strumberger, M. Hadziselimovic, A. Hamler, M. Trlep, and V. Gorican, "High-Performance Permanent Magnet Brushless Motors with Balanced

Concentrated Windings and Similar Slot and Pole Numbers," Journal of Magnetism and Magnetic Materials, vol. 304, pp. E829-E831, Sep. 2006.

[21] M. Liwschitz-Garik and C. C. Whipple, "Electric Machinery," D. Van Nostrand Company, Inc., 1947.

[22] A. M. El-Refaie, et al., "Analysis of surface permanent magnet machines with fractional-slot concentrated windings," IEEE Transactions on Energy Conversion, vol. 21, pp. 34-43, Mar. 2006.

[23] C. C. Chan, J. Z. Jiang, G. H. Chen, X. Y. Wang, and K. T. Chau, "A Novel Polyphase Multipole Square-Wave Permanent-Magnet Motor Drive for Electric Vehicles," IEEE Transactions on Industry Applications, vol. 30, pp. 1258-1266, Sep.-Oct. 1994.

[24] B. C. Mecrow, A. G. Jack, J. A. Haylock, J. Coles, "Fault-Tolerant Permanent Magnet Machine Drives," IEE Proceedings-Electric Power Applications, vol. 143, pp. 437-442, Nov. 1996.

[25] 한양대학교에너지변환연구실, "매입자석 동기모터의 설계 및 제어," Seoul: 교보문고, 2010.

[26] T. A. Lipo, "Introduction to AC Mchine Design," Madison: University of Wisconsin-Madison, 1996.

[27] Nicola Bianchi, and Thomas M. Jahns, "Design, Analysis, and Control of Interior PM Synchronous Machines," CLEUP, 2004.

[28] C. G. Veinott, "Theory and design of small induction motors," New York: McGraw-Hill, 1959.

[29] I. Boldea and S. A. Nasar, "The induction machines design handbook, 2nd edition," Boca Raton: Taylor & Francis, 2010.

[30] D. C. Hanselman, "Brushless permanent-magnet motor design," New York: McGraw-Hill, 1994.

[31] D. C. Hanselman, "Brushless permanent magnet motor design, 2nd edition," Cranston, R.I.: The Writers' Collective, 2003.

[32] J. F. Gieras and M. Wing, "Permanent magnet motor technology: design and applications, 2nd edition," New York: Marcel Dekker, 2002.

[33] R. Dutta and M. F. Rahman, "Design and analysis of an interior permanent magnet (IPM) machine with very wide constant power operation range," IEEE Transactions on Energy Conversion, vol. 23, pp. 25-33, Mar 2008.

[34] C. Koutroulis, et al., "Advanced permanent magnet machine design and construction for wind power generation and traction applications," International Journal of Applied Electromagnetics and Mechanics, vol. 13, pp. 285-290, 2001.

[35] S. I. Kim, et al., "Design process of interior PM synchronous motor for 42-V electric air-conditioner system in hybrid electric vehicle," IEEE Transactions on Magnetics, vol. 44, pp. 1590-1593, Jun 2008.

[36] C. C. Hwang, et al., "Influence of pole and slot combinations on cogging torque in fractional slot PM motors," Journal of Magnetism and Magnetic Materials, vol. 304, pp. E430-E432, Sep. 2006.

[37] T.J.E. Miller, "Brushless Permanent-Magnet and Reluctance Motor Drives," Oxford Science Publications, 1989

[38] Peyman Niazi, "Permanent Magnet assisted Synchronous Reluctance Motor Design and Performance Improvement," Dissertation of Texas A&M University, Dec. 2005.

[39] J.R. Hendershot Jr, and T.J.E. Miller, "Design of Brushless Permanent-Magnet Motors," Oxfrod University Press Inc., 1994.

[40] Kab-Jae Lee, Ki-Chan Kim, Sol Kim, Joon Seon Ahn, SeongYeop Lim, and Ju Lee, "Optimal Magnet Shape to Improve Torque Characteristics of Interior Permanent Magnet Synchronous Motor," Journal of Applied Physics, Vol. 97, No. 10, Parts 2 & 3, 10Q505, 15 May, 2005.

[41] Edwin K. P. Chong and Stanislaw H. Zak, "An Introduction to Optimization," John Wiley & Sons, Inc., 2001.

[42] Jolly L., Jabbar M.A., Lju Qinghua, " Design Optimization of Permanent Magnet Motors Using Response Surface Methodology and Genetic Algorithms," IEEE Transactions on Magnetics, Vol. 41, No. 10, pp.3928-3930, Oct. 2005.

[43] T. Heikkila, "Permanent Magnet Synchronous Motor for Industrial Inverter Applications - Analysis and Design," Dissertation of Lappeenranta University of Technology, 2002.

[44] G. H. Kang, J. P. Hong, G. T. Kim, and J.W. Park, "Improved Parameter Modeling of Interior Permanent Magnet Synchronous Motor based on Finite

Element Analysis," IEEE Transactions on Magnetics, Vol. 36, No. 4, pp. 1867-1870, Jul. 2000.

[45] Magunssen, F., Thelin, P. and Sadarangani, C., "Design of Compact Permanent Magnet Machines for a Novel HEV Propulsion System," Proceedings of Electric Vehicle Symposium(EVS-20), Long Beach, USA, Nov. 2003.

[46] T.M. Jahns, "Flux-Weakening Region Operation of an Interior Permanent-magnet Synchronous Motor Drive," IEEE Transactions on Industry Applications, Vol. IA-23, No. 4, pp.681-689, 1986.

[47] S.R. MacMinn and T.M. Jahns, "Control Techniques for Improved High-Speed Performance of Interior PM Synchronous Motor Drives," IEEE Transactions on Industry Applications, Vol. IA-27, No. 4, pp.997-1004, 1991.

[48] S. Morimoto, M, Sanada and Y. Taketa, "Wide-Speed Operation of Interior Permanent Magnet Synchronous Motors with High Performance Current Regulatior," IEEE Transactions on Industry Applications, Vol. IA-30, No. 4, pp.920-926, 1994.

[49] S. Morimoto, and Y. Taketa, "Current Phase Control Methods for Permanent Magnet Synchronous Motor," IEEE Transactions on Power Electronics, Vol. 5, No. 2, pp.133-139, 1990.

[50] Y. Honda, T. Nakamura, T. Higaki and Y. Takeda, "Motor Design Considerations and Test Results of an Interior Permanent Magnet Synchronous Motor for Electric Vehicles," IEEE Industry Applications Society Annual Meeting, New Orleans, 1997.

[51] N. Mohan, T.M. Undeland and W.P. Robbins, "Power Eletronics Converters, Applications and Design," John Wiley and Sons, Inc., 1989.

[52] T. Matsuo and T. A. Lipo, "Rotor design optimization of synchronous reluctance machine, " IEEE Trans. Energy Convers., vol. 9, no. 2, pp. 359-365, Jun. 1994.

[53] K-C. Kim, J. Lee, H-J. Kim, and D-H. Koo, "Multiobjective Optimal Design for Interior Permanent Magnet Synchronous Motor," IEEE Trans. on Magnetics, vol. 45, no. 3, Mar. 2009.

[54] N. Matsui, Y. Takeda, S. Morimotor, and Y. Honda, "Umekomi Jishaku Douki Motor no Sekkei to Seigyo," Ohmsha Ltd, 2001.

[55] J. Baek, M. M. Rahimian, and H. A. Toliyat, "Optimal Design of PM Assisted Synchronous Reluctance Generators using Lumped Parameter Model and

differential Evolution Strategy," Energy Conversion Congress and Exposition, 2009. ECCE 2009. IEEE, pp. 2453-2459, 2009.

[56] J-B. Park, M. Johnson, H. A. Toliyat, "Integrated Torque Ripple Analysis Method for Multi-Phase Motors," Electric Machines & Drives Conference (IEMDC), 2013 IEEE International, pp. 281-286, May 2013.

[57] R. H. Myers, and D. C. Montgomery, "Response Surface Methodology in Process and Product Optimization Using Designed Experiments, 2nd edition," vol. 1, New York: Wiley, 2002.

[58] P. Zhang, S-O. Kwon, L. Fang, and J-P. Hong, "The Design and Analysis of a High Efficiency Permanent Magnet Reluctance Motor," in International Conference on Electrical Machines and Systems (ICEMS), pp. 1-7, 2006.

[59] K-C. Kim, J-S. Ahn, S-H. Won, and J. Lee, "The Parameter Study of Permanent Magnet Wind Generator for Low Cogging Torque and Power Ripple," The International Conference on Electrical Engineering (ICEE 2007), pp. 210 (CD-PDF), Hong Kong, China, July, 2007.

[60] P. Niazi, "Permanent Magnet assisted Synchronous Reluctance Motor Design and Performance Improvement," Ph.D. Dissertation, Texas A&M University, Dec. 2005.

[61] K-J. Lee, K-C. Kim, S. Kim, J-S. Ahn, S-Y. Lim, and J. Lee, "Optimal Magnet Shape to Improve Torque Characteristics of Interior Permanent Magnet Synchronous Motor," Journal of Applied Physics, Vol. 97, No. 10, Parts 2 & 3, 10Q505, 15 May, 2005.

[62] J. Antony, "Design of Experiments for Engineers and Scientists," Butterworth-Heinemann, 2003.

[63] R. Shi, H.A. Toliyat, and A. El-Antably, "A DSP-based direct torque control of five-phase synchronous reluctance motor drive," Applied Power Electronics Conference and Exposition(APEC) 2001, Sixteenth Annual IEEE Vol. 2, pp. 1077-1082, 2001.

[64] N.P. Ananthamoorthy; and K. Baskaran, "Simulation of PMSM based on current hysteresis PWM and Fed PI controller," Computer Communication and Informatics (ICCCI), pp. 1-5, 2012.

[65] G.Z. Wu, and H.Y. Zhu, "Combined hysteresis current-controlled PWM inverter and robust control for a permanent-magnet synchronous motor," Electric Information and Control Engineering (ICEICE), pp. 5753-5757, 2011.